A DETERMINATION OF THE BRANCHING RATIO

OF

K_L TO GAMMA GAMMA

BY

HAMISH W. M. NORTON

DECEMBER, 1984

THE UNIVERSITY OF CHICAGO

A DETERMINATION OF THE BRANCHING RATIO OF K_L TO GAMMA GAMMA

A DISSERTATION SUBMITTED TO
THE FACULTY OF THE DIVISION OF THE PHYSICAL SCIENCES
IN CANDIDACY FOR THE DEGREE OF
DOCTOR OF PHILOSOPHY

DEPARTMENT OF PHYSICS

BY

HAMISH W. M. NORTON

CHICAGO, ILLINOIS

AUGUST, 1984

TABLE OF CONTENTS

LIST OF ILLUSTRATIONS

LIST OF ILLUSTRATIONS--Continued

LIST OF ILLUSTRATIONS--Continued

Figures

CHAPTER I

INTRODUCTION

The decay $K_L \to \gamma\gamma$ is of some current interest theoretically. As a particularly simple decay, it is useful in studying how well the kaon is understood in terms of the quark model.

Several predictions of the branching ratio

$$\frac{K_L \to \gamma\gamma}{K_L \to \text{all}}$$

have been published in recent years.[1,2,3,4,5] Those based upon phenomenological methods, using as input the rates of π°, η and η' to $\gamma\gamma$, have been reasonably accurate.[3,5] Such predictions are based upon a calculation of the weak matrix elements connecting the K_L to each of the three pseudoscalar mesons, and then use the measured electromagnetic decay rates of those mesons into $\gamma\gamma$. Figure 1 shows this process schematically:

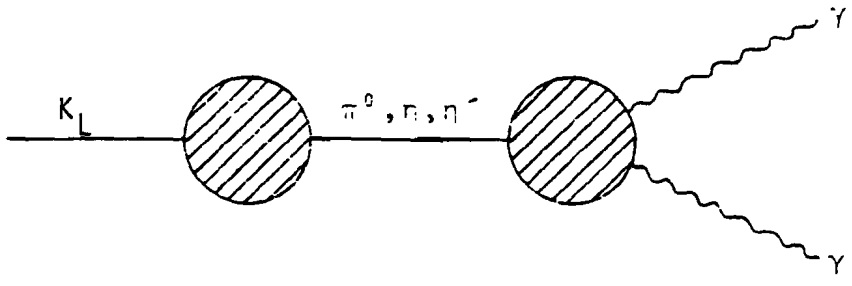

Figure 1. $K_L \to \gamma\gamma$ pole diagram

all the previous results are quite consistent[7,8,9,10,11,12] (except for a couple which were later retracted), they were all based either upon a small number of signal events or upon a small number of normalization events, and hence it was difficult or impossible for the experimenters to examine many possible sources of systematic error. We will discuss in detail the previous experiments in Chapter 10.

All those experiments were either unable to measure the vector momentum of the two photons in an event, or measured it to very low precision. Hence, their ability to see possible backgrounds in either signal or normalization events was limited.

All previous experiments have worked in a range of kaon momentum where it was either difficult to see the decay gamma rays at all, or where the electron pair production cross section varied strongly with energy. Since knowledge of the pair production probability in various parts of the detector was crucial to the normalization of all these experiments, its variation with energy is unfortunate in an experiment with relatively poor energy resolution.

This experiment will address such problems with a large, well-determined sample of $K_L \to \gamma\gamma$ events, normalized

CHAPTER II

PRINCIPLES OF THE MEASUREMENT

The branching ratio of K_L into $\gamma\gamma$ is measured by comparing the rate of $K_L \to \gamma\gamma$ decays to that of $K_L \to \pi^\circ\pi^\circ\pi^\circ$, which is known to have a branching ratio[6] of (0.215 ± 0.01). The error in this previously measured branching ratio will be seen to be the limiting error of this experiment.

The measurement of

$$\frac{\text{rate}\ (K_L \to \gamma\gamma)}{\text{rate}\ (K_L \to 3\pi^\circ)}$$

is quite straightforward. K_L decays into both $\gamma\gamma$ and $3\pi^\circ$ are detected simultaneously in the same neutral beam. Rate dependent effects due to the dead time of the spectrometer are the same for each type of decay, and therefore cancel in the ratio.

The two types of decay are reconstructed in a very similar way. In the $K_L \to 3\pi^\circ$ decay, the pions decay immediately[13] into pairs of gamma rays, so the apparatus must deal with either two or six gamma rays. Exactly one of the gamma rays is converted in a thin lead sheet, and the resultant electron pair is tracked by scintillation hodoscopes and drift chambers. The other gamma rays are not converted until they are detected in a lead glass

Vertex Reconstruction

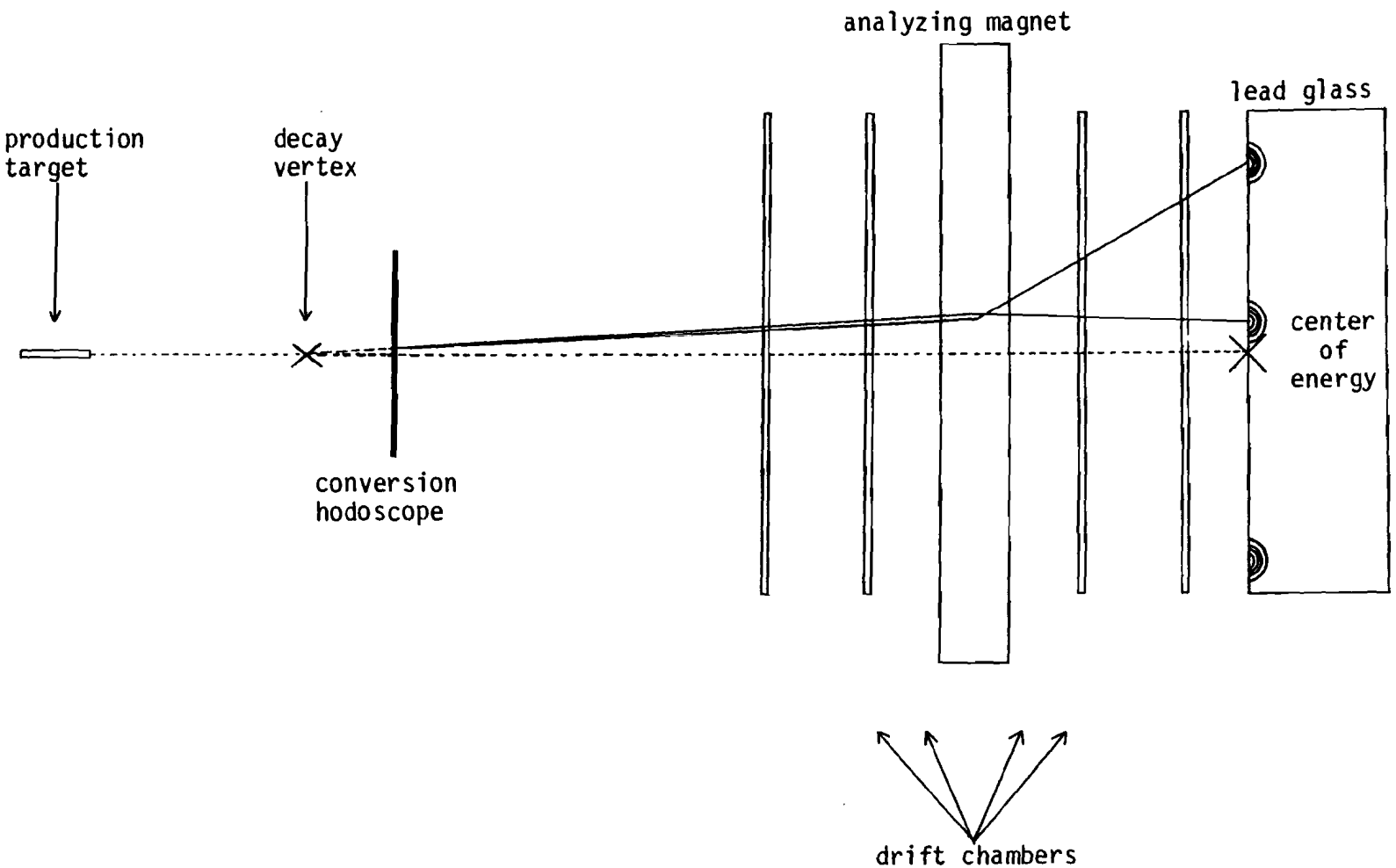

between the line traveled by the converted photon and that traveled by the kaon be small. In $K_L \to 3\pi^\circ$ events we also demand that there be some pairing of the six gammas such that the invariant mass of each pair is consistent with that of a π°.

The distribution of electron positions at any detector in the experiment is almost identical for the two modes considered, so that any small inefficiencies in charged particle tracking cancel in the ratio of decay rates. The acceptance of the spectrometer for the two decay modes is, however, not identical, and must be calculated with a Monte Carlo simulation of the apparatus.

The branching ratio of $K_L \to \gamma\gamma$ is thus given by

$$\frac{N_{\gamma\gamma}}{A_{\gamma\gamma}} \times \frac{A_{3\pi^\circ}}{N_{3\pi^\circ}} \times BR(3\pi^\circ)$$

where $N_{\gamma\gamma}$ denotes the observed number of $K_L \to \gamma\gamma$ decays, $N_{3\pi^\circ}$ denotes the observed number of $K_L \to 3\pi^\circ$ decays, $A_{\gamma\gamma}$ denotes the acceptance of the apparatus for $K_L \to \gamma\gamma$ decays, $A_{3\pi^\circ}$ denotes the acceptance of the apparatus for $K_L \to 3\pi^\circ$ decays, and $BR(3\pi^\circ)$ denotes the world average branching ratio of $K_L \to 3\pi^\circ$.

separated spots at our spectrometer. Beam profiles at our lead glass as measured by $K_L \to 3\pi^\circ$ events are shown in Figures 4 and 5.

Where possible, the beam was transported in vacuum to minimize scattering. All collimators downstream of 100 meters were under vacuum.

Figure 6 shows the decay region and spectrometer, starting roughly 390 meters downstream of the target. Near the beginning of the decay region is a regenerator-sweeping magnet assembly used to produce a K_S beam for the ε' experiment. The regenerator moved from one beam to the other between each pulse of the accelerator, so that one beam was a pure K_L beam and the other was a mixture of K_L and K_S. The position of the regenerator was recorded, and decays used in this experiment were required to originate in the unregenerated beam.

We had four anti-counter planes in the decay region, upstream of the spectrometer. Two, the RA (regenerator anti), located in the beam immediately downstream of the regenerator, and the A counter, in the beam just upstream of the conversion hodoscope, were used to veto decays into charged particles. The other two, the PA (pinching anti), surrounding the beam pipe upstream of the regenerator, and the DRA (decay region anti), surrounding the conversion hodoscope, were faced with three radiation

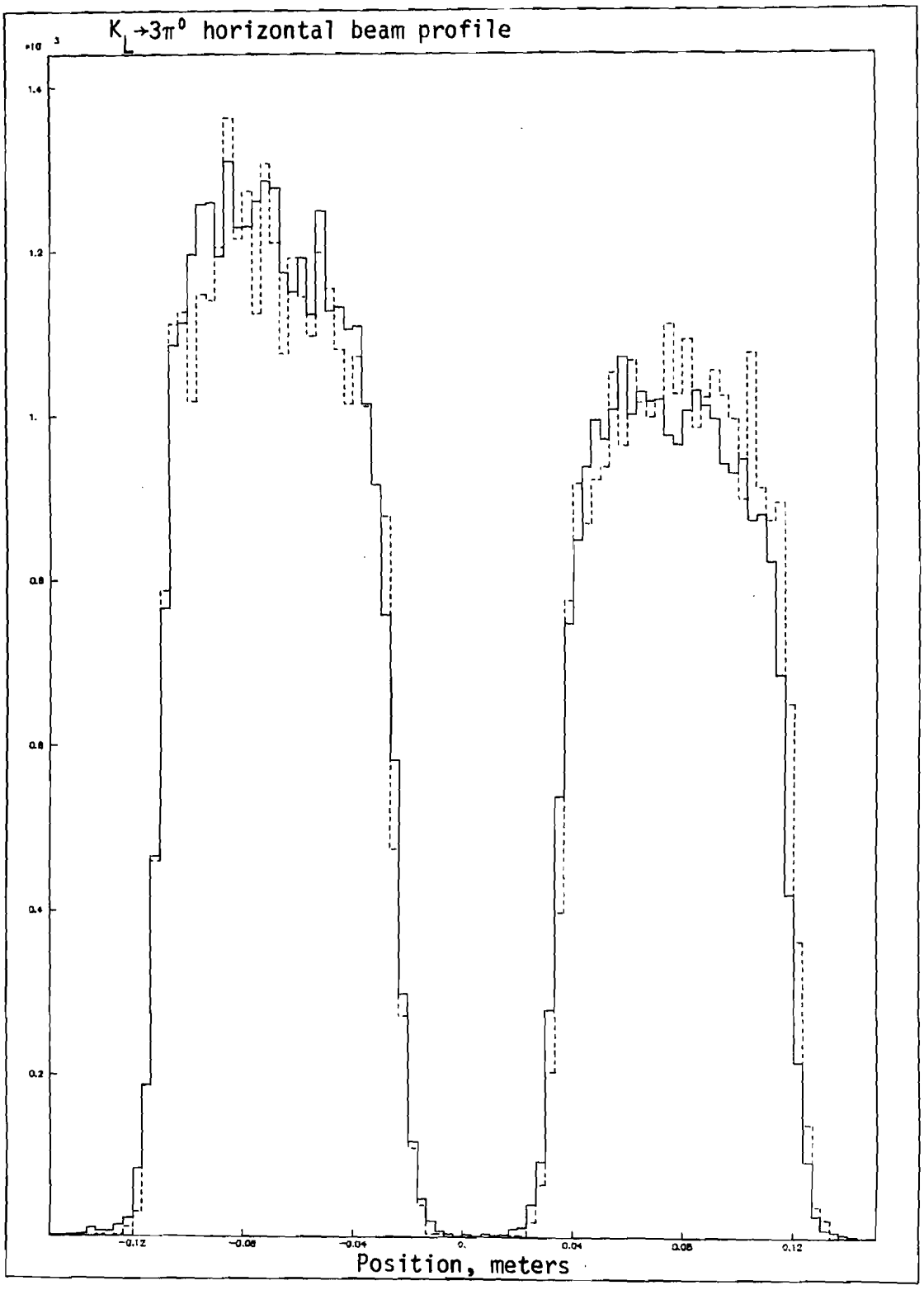
$K_L \rightarrow 3\pi^0$ horizontal beam profile
x10 3
1.4
1.2
1.
0.8
0.6
0.4
0.2
-0.12
-0.08
-0.04
0.
0.04
0.08
0.12
Position, meters

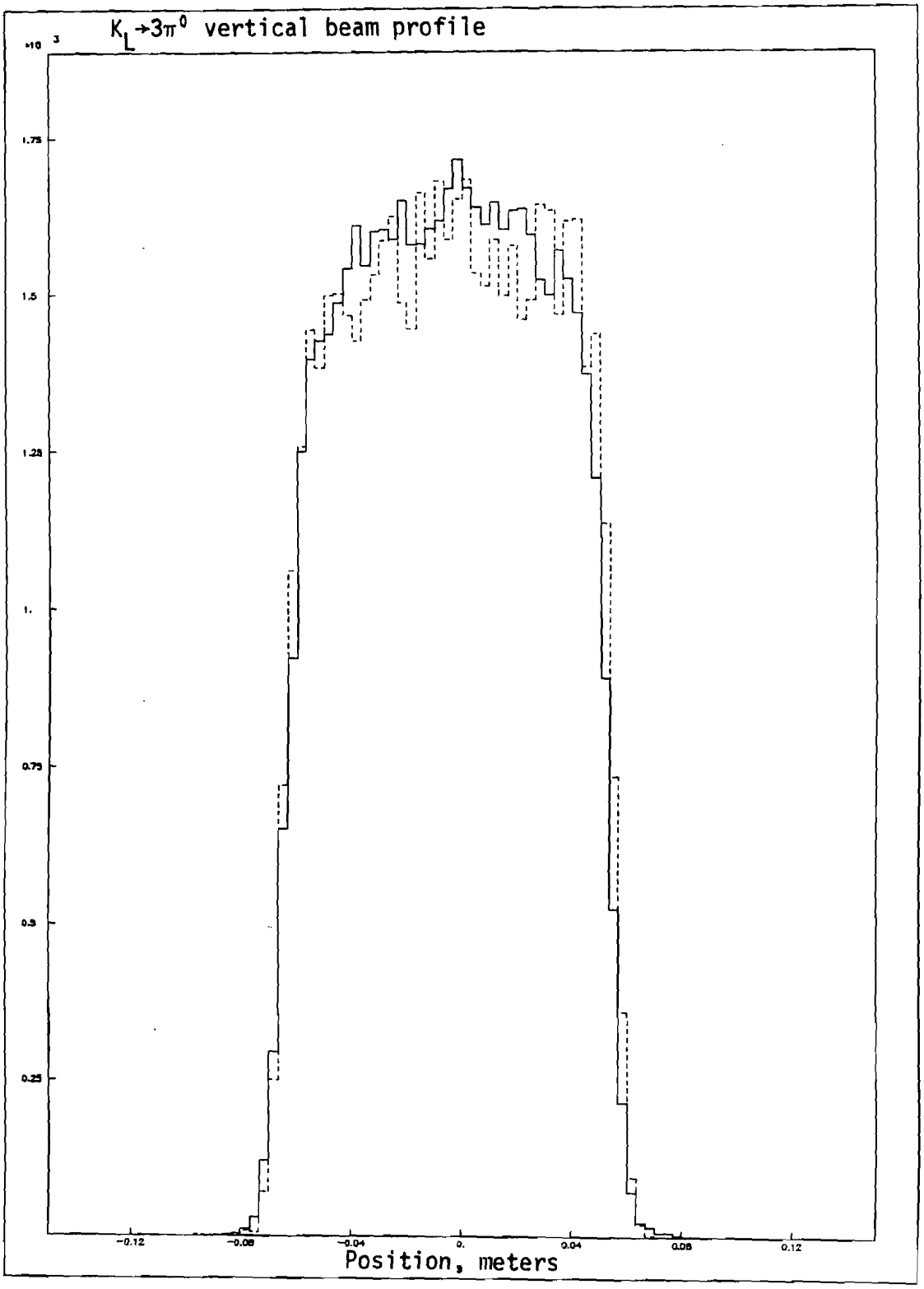
$K_L \to 3\pi^0$ vertical beam profile
×10 3
1.75
1.5
1.25
1.
0.75
0.5
0.25
−0.12
−0.08
−0.04
0.
0.04
0.08
0.12
Position, meters

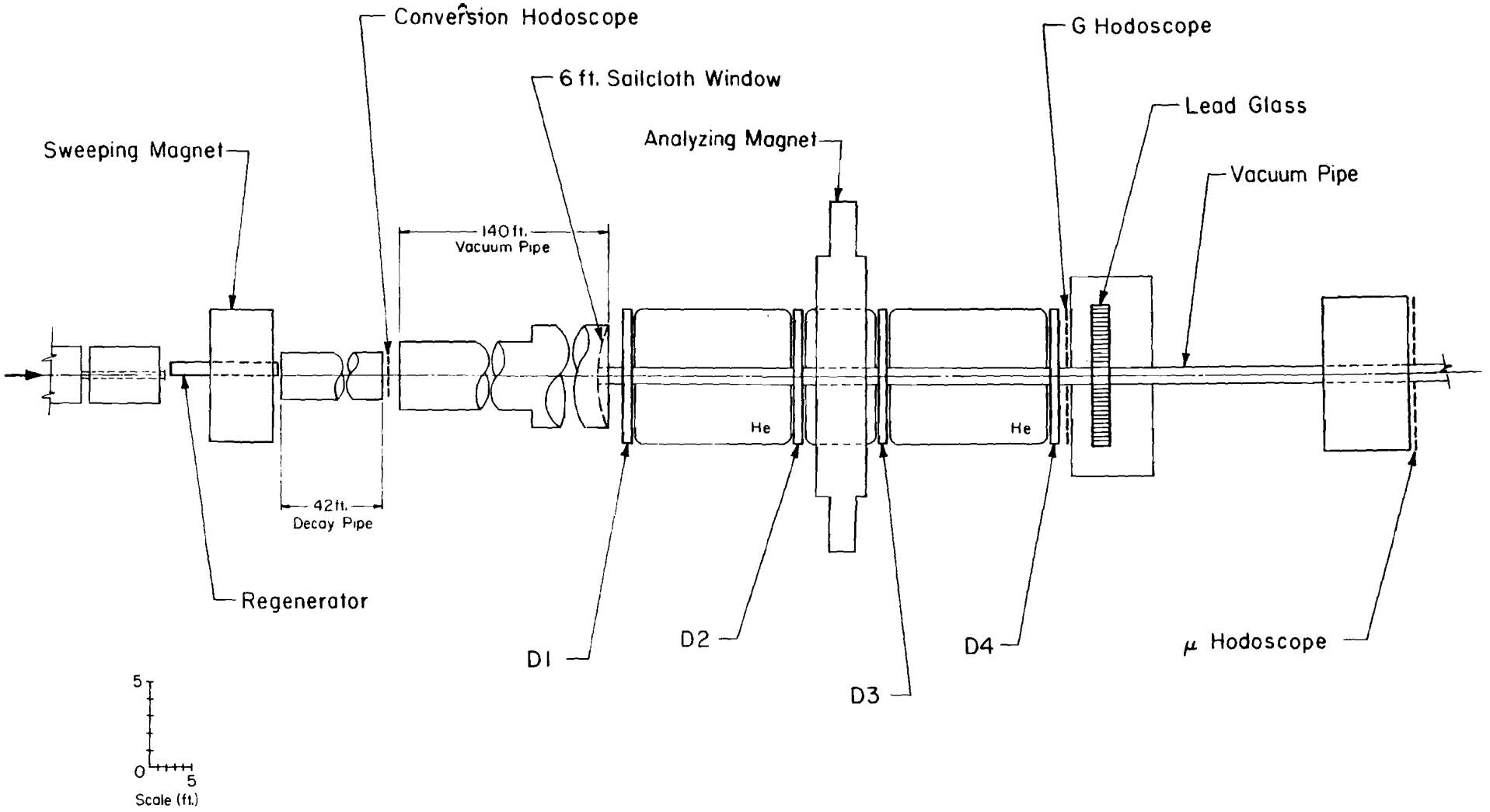
Conversion Hodoscope
6 ft. Sailcloth Window
G Hodoscope
Lead Glass
Analyzing Magnet
Sweeping Magnet
Vacuum Pipe
140 ft.
Vacuum Pipe
He
He
42 ft.
Decay Pipe
Regenerator
D1
D2
D3
D4
μ Hodoscope
5
0
5
Scale (ft.)

Conversion Hodoscope - Plan View

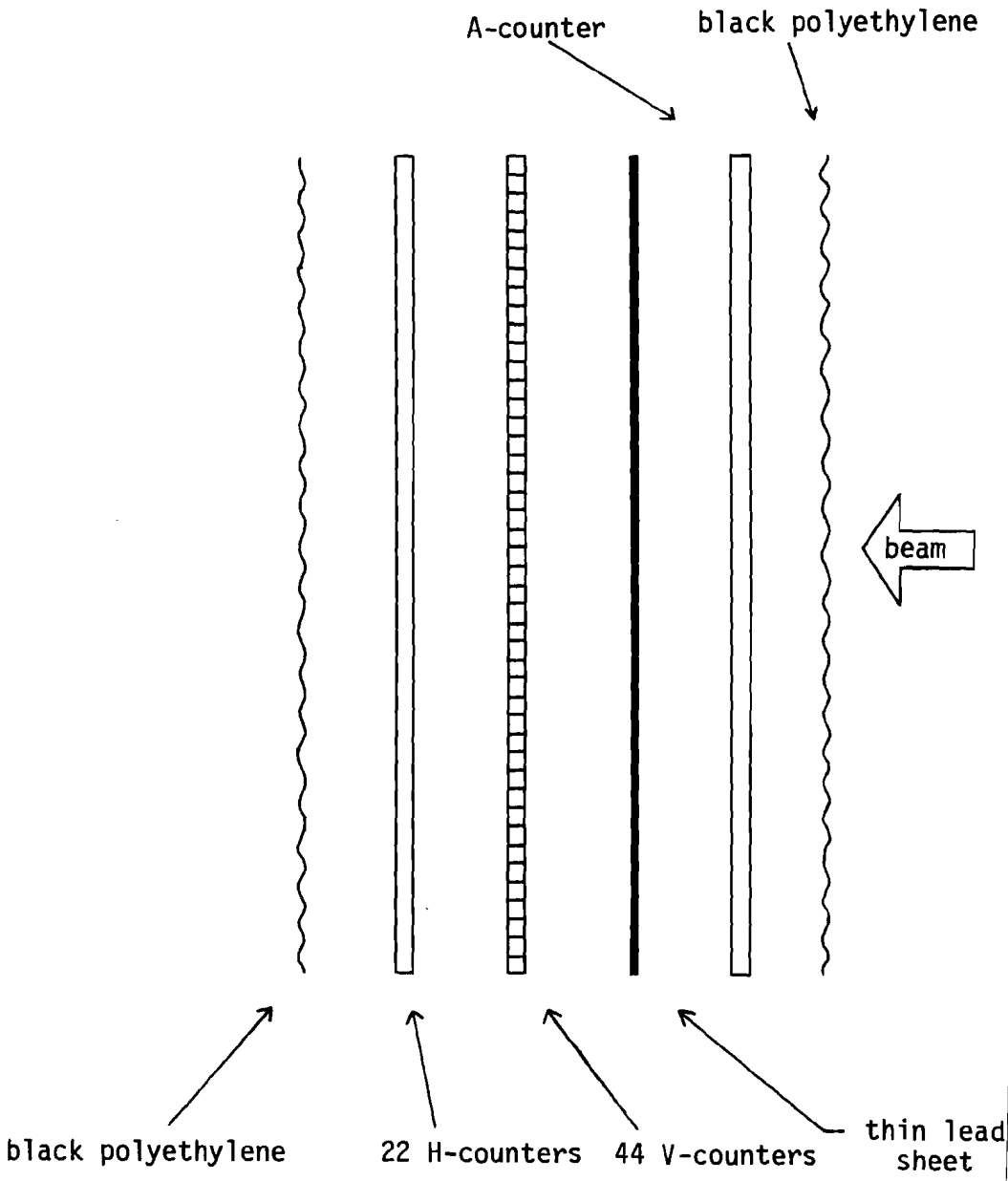

Electron trajectories were measured by four drift chambers, two on either side of the analyzing magnet. Each chamber had two horizontal and two vertical planes of sense wires. The distance between sense wires was 4.57 cm, and the distance between planes was 3 cm. The active region of the chambers was 1 meter high by 2 meters wide, except for a hole in the middle which allowed our beam pipe to pass through. A box surrounded this hole, and wires that intercepted the box were soldered to it.

The chambers used a mixture of half argon-half ethan, and were operated at 4800 V. They were measured to have an efficiency of ~98% and a resolution of 220 μ/plane.[15] The readout system had a multiple hit per wire capability, but the dead time of the electronics limited two track resolution to 5 mm.

The analyzing magnet had a useful aperture of 40 x 100 inches and a nomimal P_T kick of 107.6 MeV/c. The P_T kick was determined by triggering on $K_S \to \pi^+\pi^-$ and demanding that the K_S mass reconstruct to its known value.[15] Detailed field maps had been measured in a previous experiment.

Two planes of lead-faced anticounters vetoed events in which some gamma rays could not be reconstructed. One of these, the MA (magnet anti), was just upstream of the analyzing magnet, above and below its aperture. The other one, the CA (collar anti), surrounded the beam pipe

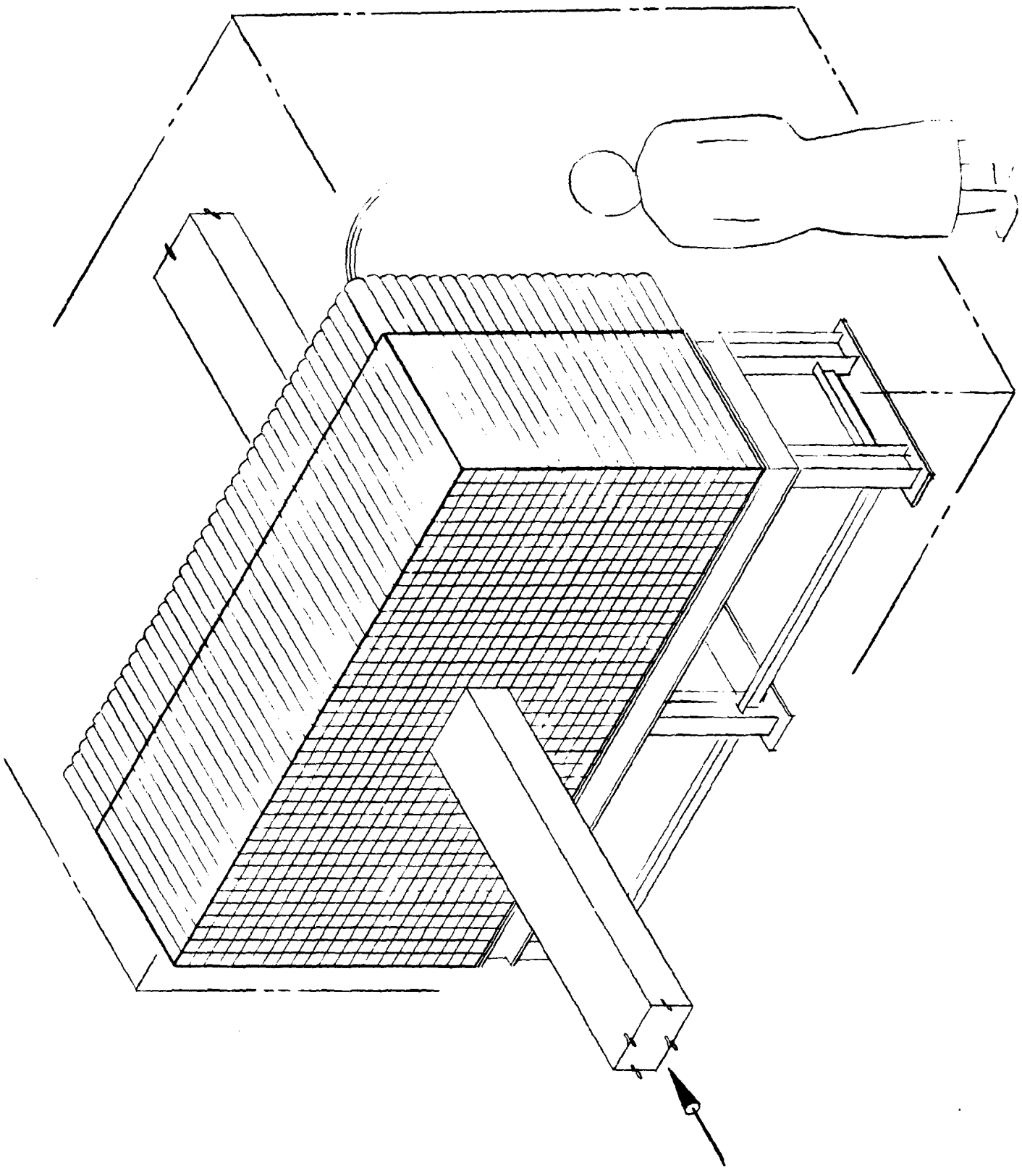

enclosure into a fast signal which went to a trigger processor, and a slow signal which went into a 450 ns delay cable before being digitized. The delay allowed time to make a trigger decision. The fast signal was picked off by a 10,000 Ω low capacitance amplifier input, in order not to degrade the signal going to the digitizers. We used LeCroy model 2285 ADC's which had 12 bits/channel, 24 channels/card. We had some difficulties calibrating them, which will be described in Chapter 5. The entire lead glass detector was housed in an insulated house held to a constant temperature ±1°C, in order to minimize electrical and mechanical drifts.

We anticipated that despite our best efforts, the calorimeter response would change in time. In order to monitor the response of individual channels, we used an air spark gap light source, which closely approximated the duration and spectrum of the Čerenkov light pulses normally observed in our lead glass. The light from this spark gap was focused on a bundle of optical fibers, which were fanned out so that each lead glass block had one small fiber bundle illuminating its upstream face.

The brightness of the flasher was monitored by two ITT vacuum photodiodes and also by two special reference photomultiplier-lead glass block assemblies, which were kept away from the beam, and hence did not suffer any

information, which shall be called TC, and that from the trigger processor, which shall be called TP. Several logical variables go into TC, as defined below:

2GU = two or more G-counters hit above the beam

2GD = two or more G-counters hit below the beam

3G = three or more G-counters hit

A = A counter hit

1H = one or more H-counters hit

1V = one or more V-counters hit

H10 = one or more H-counters show >10x minimum ionizing energy

2H = two or more H-counters hit

DRA = decay region anti hit

RA = one or both RA counters hit (one for each side of beam)

RF = synchronization signal from the accelerator; true when the particles from one RF bucket pass through our apparatus

MA = magnet anti hit

In terms of these variables, the trigger component TC is given by

```
TC = (2GU .or. 2GD) .and. (.not. 3G)
     .and. (.not. A) .and. 1H .and. 1V
     .and. (.not. H10) .and. (.not. 2H)
     .and. (.not. DRA) .and. (.not. RA)
     .and. (.not. MA) .and. RF
```

defined as

$$E_2 = \sum_{i=1}^{\#blocks} E_i r_i^2$$

where E_i is the energy is block i and r_i is the distance from the center of the lead glass array to that block. We were able to use this second moment to make a fast calculation of the invariant mass of the event. Remember that the square of the invariant mass is given by:

$$m^2 = \left(\sum_{i=1}^{\#gammas} E_i\right)^2 - \left(\sum_{i=1}^{\#gammas} \vec{p}_i\right)^2$$

and since photons have no rest mass, $E_i = |\vec{p}_i|$:

$$m^2 = \left(\sum_{i=1}^{\#gammas} E_i\right)^2 - \sum_{i=1}^{\#gammas} E_i^2 - 2 \sum_{i=2}^{\#gammas} \sum_{j=1}^{i-1} E_i E_j \cos\theta_{ij}$$

where θ_{ij} is the angle between the two gamma rays. If we approximate $\cos\theta$ by $1-\theta^2$,

$$m^2 \simeq \sum_{i>j} E_i E_j \Theta_{ij}^2.$$

If we assume each shower spreads only a small amount, we may sum over lead glass blocks instead of gamma rays:

$$m^2 \simeq \sum_{i=2}^{\#blocks} \sum_{j=1}^{i-1} E_i E_j r_{ij}^2 / z^2$$

where r_{ij} is the distance between the two blocks, and z is

TC .and. TP

If the trigger was satisfied, the scintillator, trigger processor, drift chamber, and lead glass information was recorded by our online PDP-11/45 computer running MULTI and written to magnetic tape. No attempt to analyze the data was made online, although histograms of detector outputs were made available online in order to ensure that everything was working properly.

apparatus. These runs were useful for drift chamber alignment and lead glass calibration.

Data taking for this experiment was interrupted for several weeks about halfway through, in order to take other data which was necessary for the ε' experiment. The two sets of data were treated identically.

module seemed to have a unique response curve, essentially unrelated to that of its neighbors. While the level of these response curves changed slowly with time, it appeared that the shape of the curves remained reasonably constant over short periods of time. Between our two data sets, which were separated by several weeks, the shapes did change somewhat. Figures 9 through 12 show the response of two different modules for a representative run in each of the two data sets.

It was decided to fit 12 gain constants to the behavior of each of 804 modules for each of roughly 300 runs (~1 run per data tape).

At this point it is appropriate to discuss in some detail the operation of the LeCroy 2285 ADC's. After subtraction of a pedestal of typically 200 counts, the ADC's would typically register ~60 counts per GeV of energy deposition in a module. Their saturation level was 4032 counts (not 4095) corresponding to about 65 GeV. In order to speed up the readout of large arrays such as ours, a built in digital processor suppressed the output of channels below a user-selected threshold.

Our ADC's were set to readout every channel above five counts (~80 MeV), and one channel on either side. The way our lead glass was wired, this corresponded to one extra block to the left, and one to the right read out for every

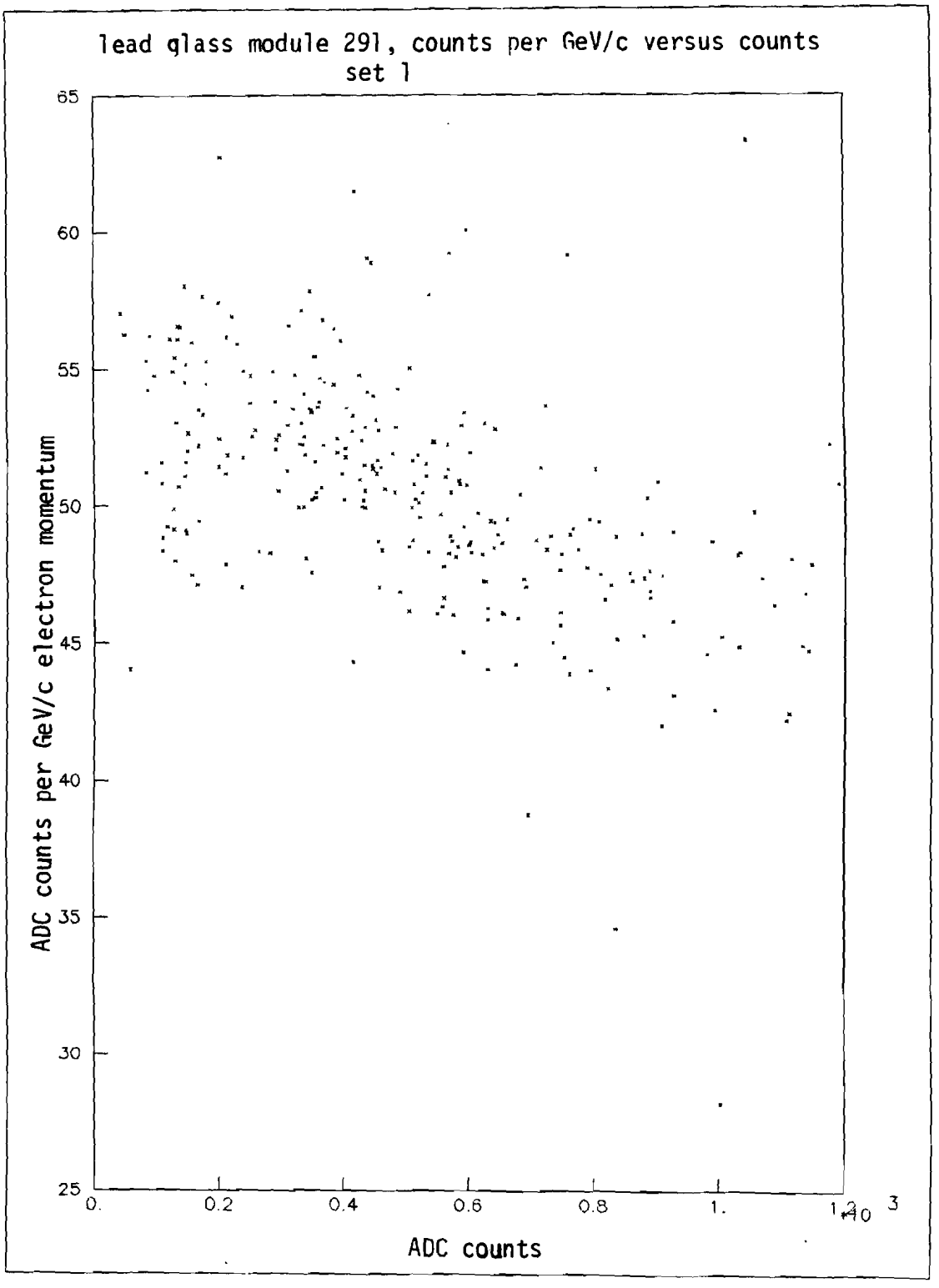
lead glass module 291, counts per GeV/c versus counts
set 1
ADC counts per GeV/c electron momentum
65
60
55
50
45
40
35
30
25
0.
0.2
0.4
0.6
0.8
1.
1.2
+40 3
ADC counts

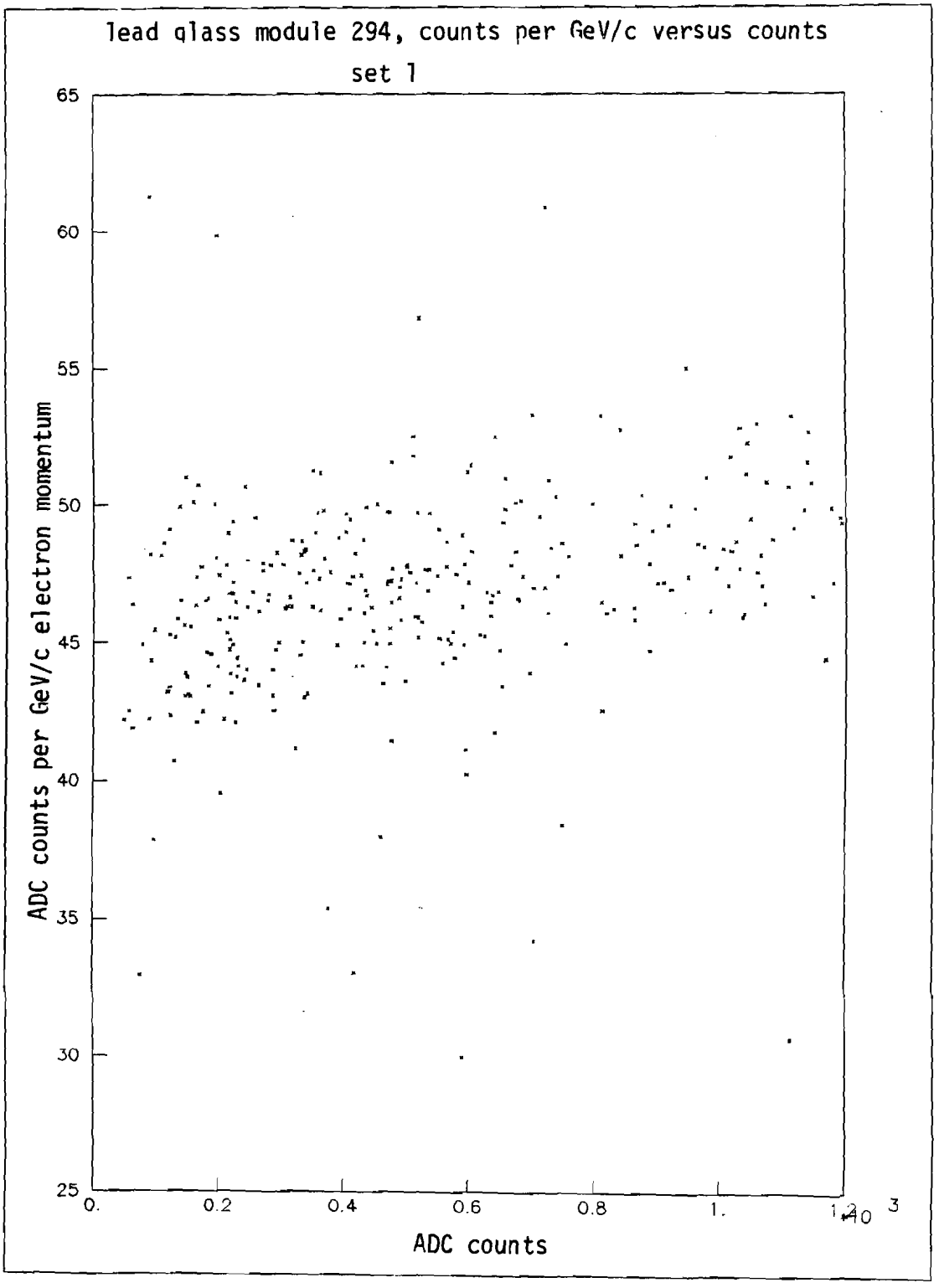
lead glass module 294, counts per GeV/c versus counts
set 1
ADC counts per GeV/c electron momentum
65
60
55
50
45
40
35
30
25
0.
0.2
0.4
0.6
0.8
1.
1.2
+40 3
ADC counts

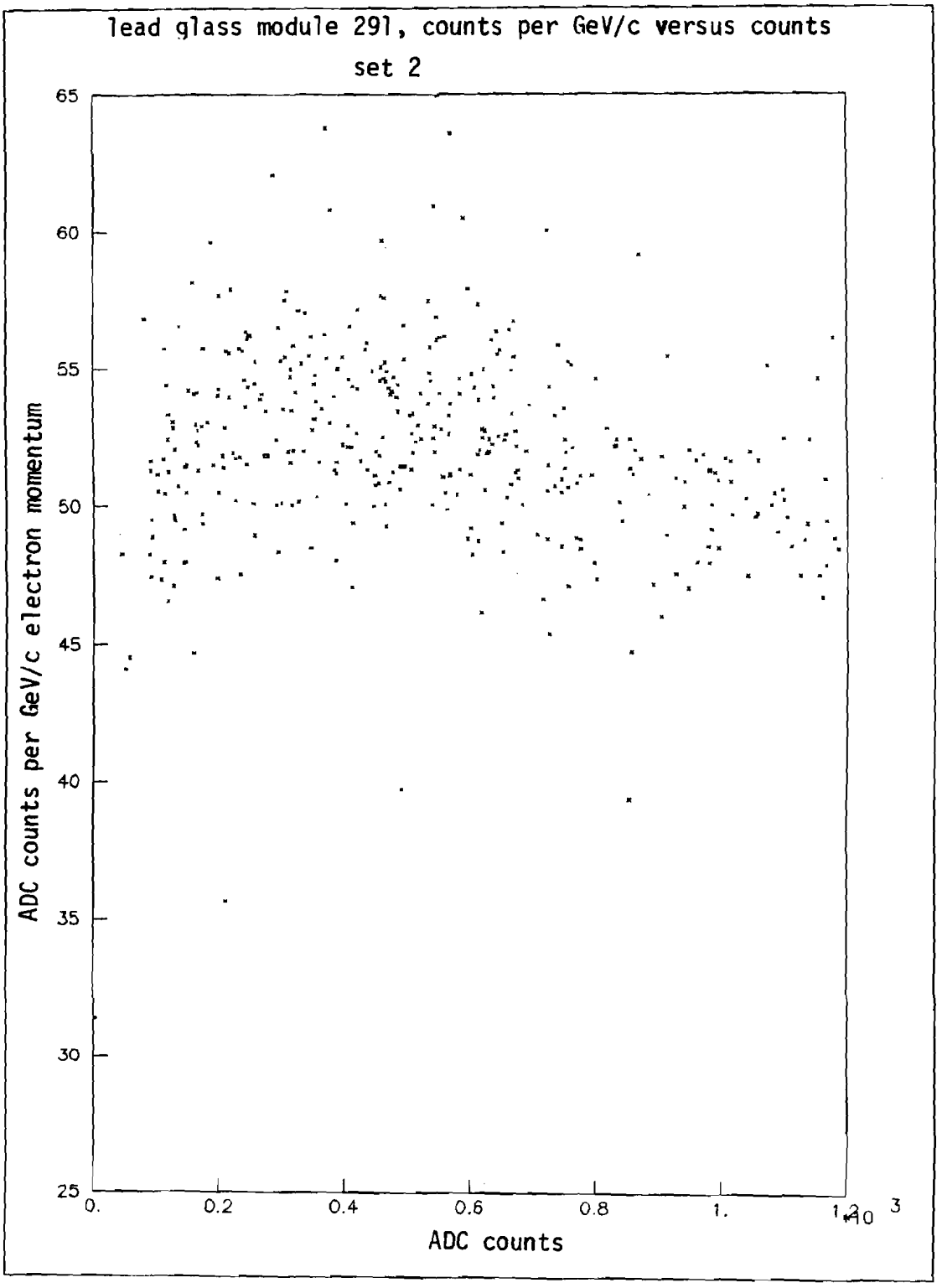
lead glass module 291, counts per GeV/c versus counts
set 2
ADC counts per GeV/c electron momentum
65
60
55
50
45
40
35
30
25
0.
0.2
0.4
0.6
0.8
1.
1.2
10 3
ADC counts

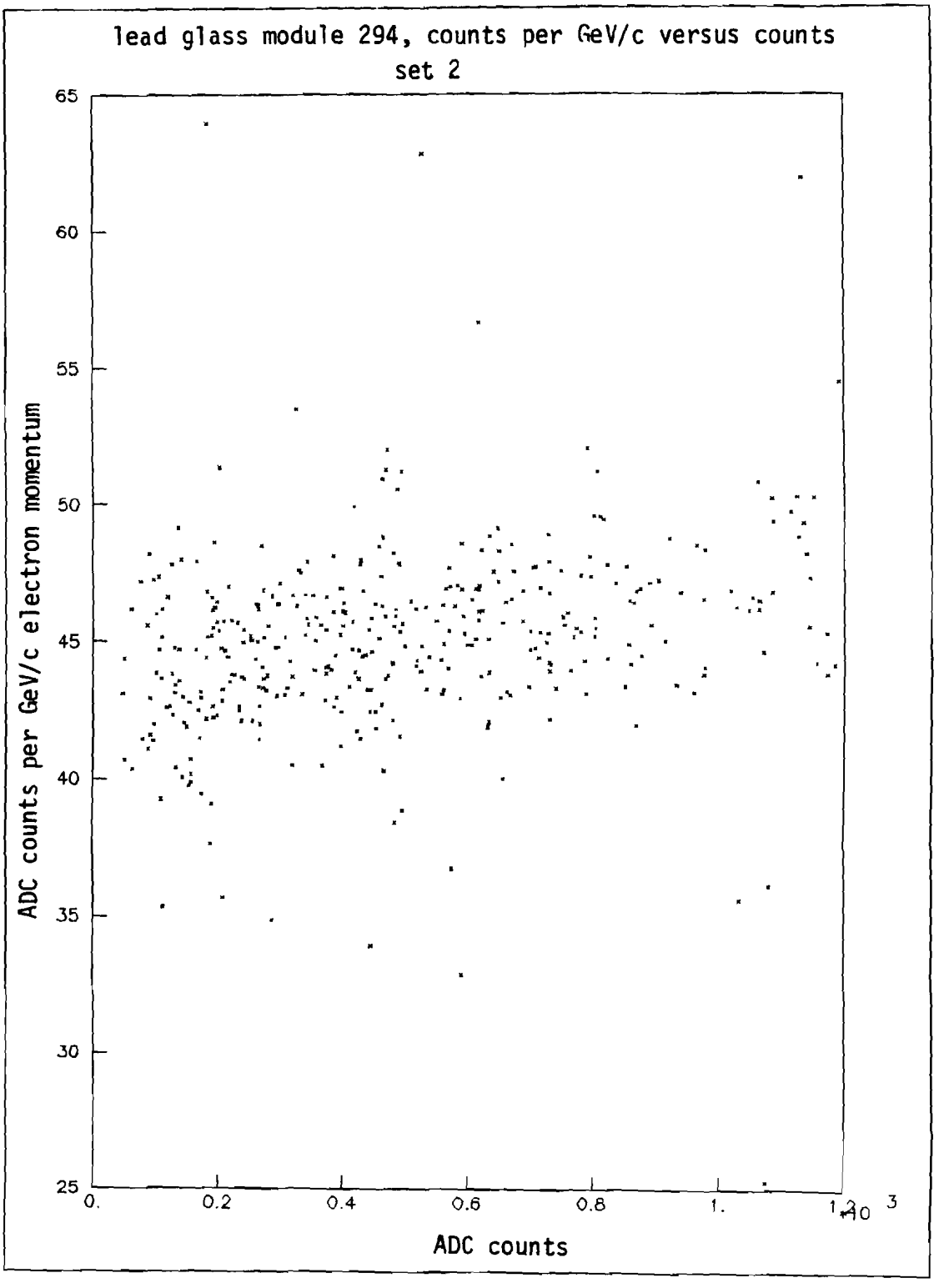
lead glass module 294, counts per GeV/c versus counts
set 2
ADC counts per GeV/c electron momentum
65
60
55
50
45
40
35
30
25
0.
0.2
0.4
0.6
0.8
1.
1.2
+03
ADC counts

response of a module at only one energy, which is much lower than the energy of any electromagnetic showers that will be of interest to us.

The second type of event used to calibrate the lead glass was our standard neutral decay trigger. Electrons from the converted photon required by this trigger had their momentum measured to high precision by our analyzing magnet and drift chambers, and one could compare this measurement to the energy reported by our lead glass. Figure 13 shows a typical neutral trigger event. As can be seen from the figure, these events have one serious problem. Since all of our electron pairs were produced by conversion of photons in a thin lead sheet, these electrons were likely to be accompanied by bremsstrahlung photons produced in the lead after the conversion point. If an electron was more energetic then 10-15 GeV, the analyzing magnet would not sufficiently separate the electron from its companion bremsstrahlung photon, and the two would be seen as one cluster of modules above threshold.

The method we used to circumvent this problem was to select a sample of electrons which were aimed at the center 25 percent of whichever block they hit. We lost 75 percent of our sample this way, but the events which remained deposited a reasonably constant $\sim$85 percent of their energy in the block which they hit directly. For electrons up to

typical neutral trigger
used for lead glass calibration

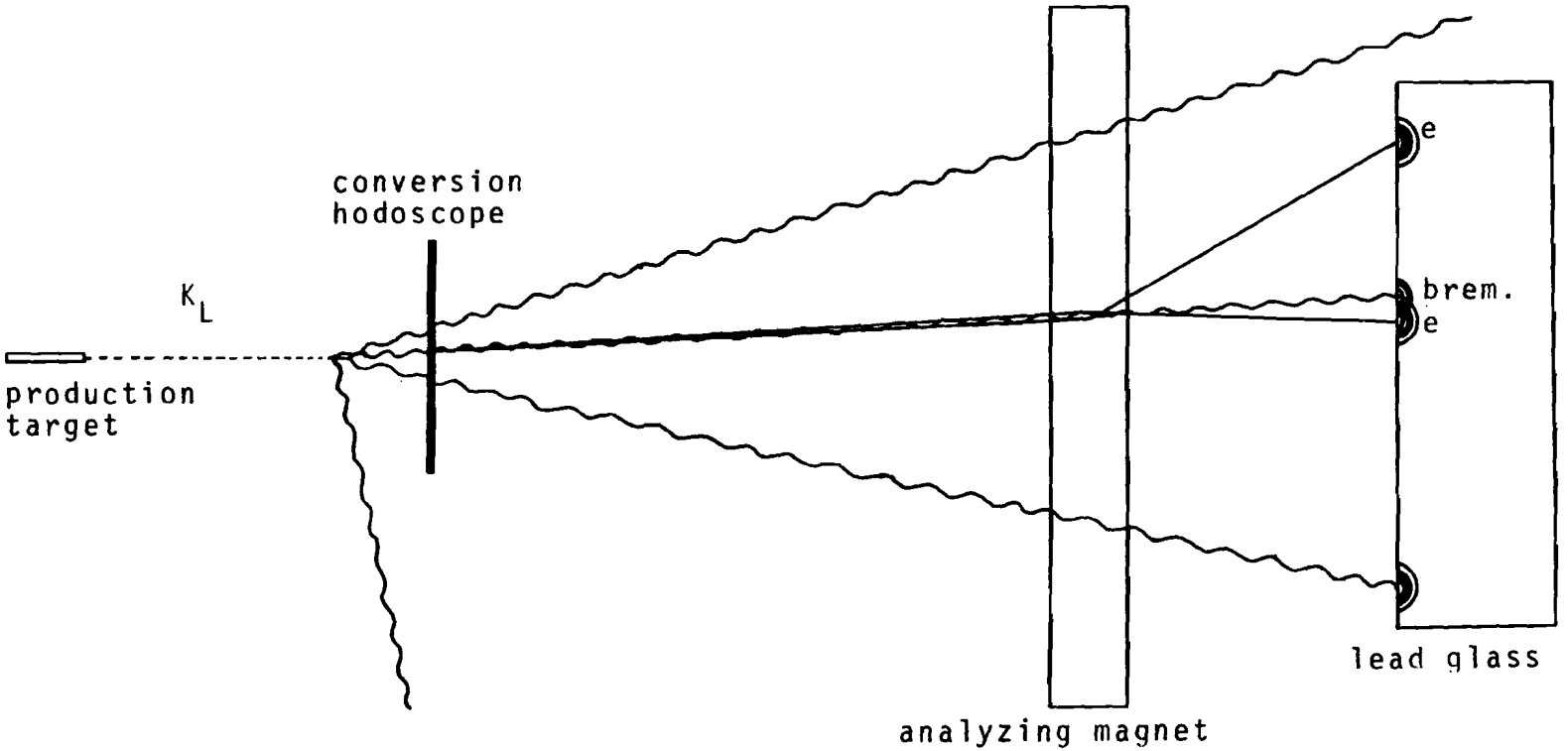

lead sheet π^0 event

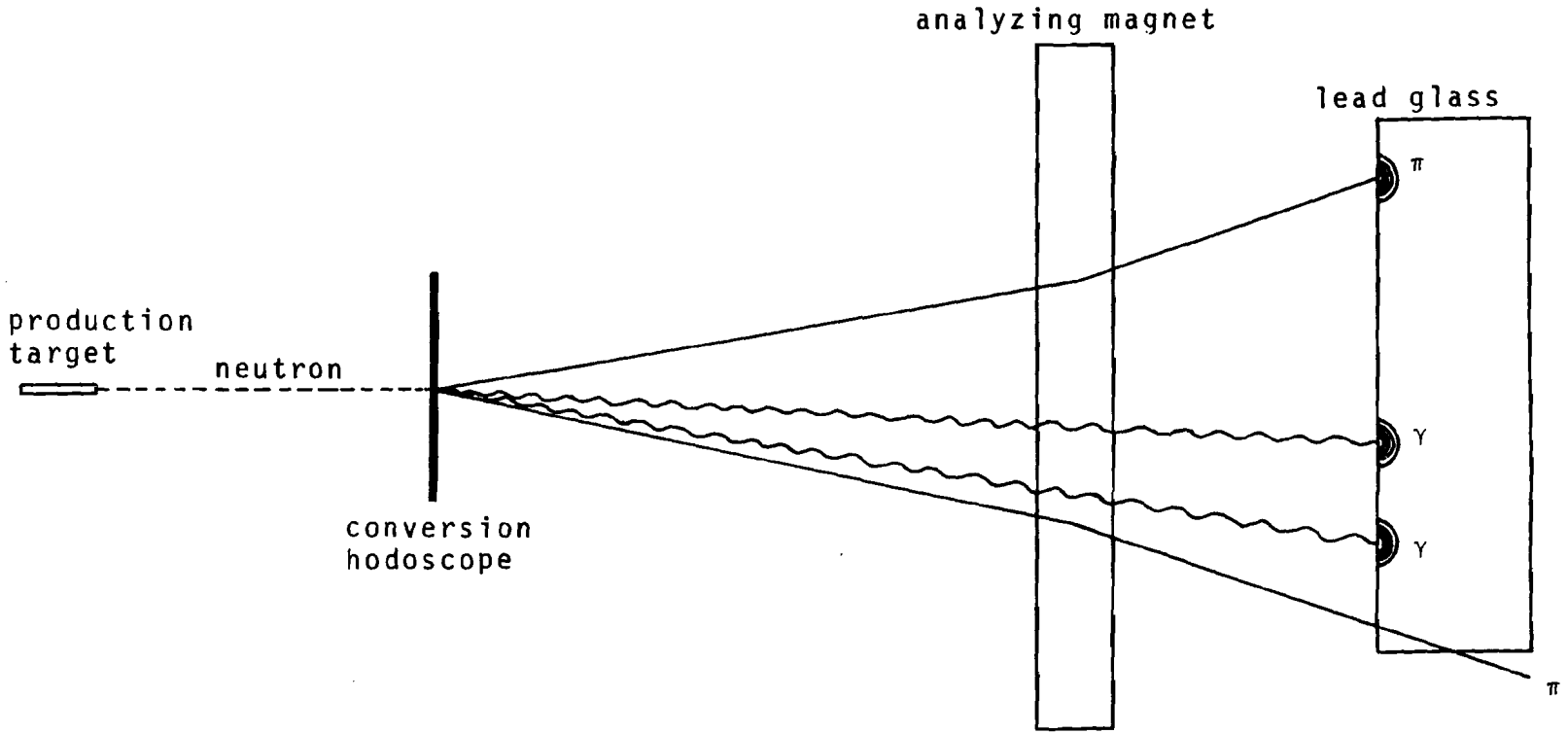

modules, as it was nearly linear in the logarithm of the pulse height ratios. The invariant mass of such an event is given to an excellent approximation by:

$$m = (E_1 E_2 r^2 / z^2)^{1/2}$$

where E_1 and E_2 are the energies of the photons, r is their separation at the lead glass, and z is the distance from the decay vertex to the lead glass. In this case, m is the known π° mass, r and z are known accurately, and therefore, one can infer the product of the photon energies. This product may be compared with the same quantity measured in the lead glass, after corrections for missing blocks have been made.

The obvious drawback of such a method of calibration is that it is not clear how to determine the response of a specific block to a given amount of energy deposition. Let us treat the problem in stages, taking first the idealized case in which the response of every module is linear and constant in time. In this case we must find only a single parameter per module: the number of ADC counts per GeV of energy deposited on a block. This parameter shall be known as the gain of the module.

Let us start our procedure by assuming that all gains equal some constant, say 60. Using these constants, which we store in an array called "Old Gains," we may analyze

both as calculated using Old Gains:

$$\text{weight} = \sqrt{E_{block}} \times \frac{E_{block}}{E_{shower}} .$$

We may now record our best guess for the new gain for each module involved in the event by updating the New Gains array. We take a weighted average of the previous New Gains and the best guess for this event, in a module by module fashion. The New Gain for a given module will be:

$$\text{New Gain} = \frac{(\text{New Gain} \times \text{Sum of Weights}) + (\text{best guess new gain} \times \text{weight})}{\text{Sum of Weights} + \text{weight}}$$

The Sum of Weights array is then updated by adding to it the weight calculated from this event.

After repeating the above process for all of the lead sheet π° events, we will have our best guess as to the array of New Gains. This is not the best job we can do to find the real gains of the lead glass, as for every event, the Old Gains entered into the calculation of the weight. We may repeat the entire process after filling Old Gains with New Gains. This iterative method is continued until it converges on a set of gains, which may take many tens of iterations.

dependence can be used to correct the Old Gains array for every event, after which the iteration may proceed as before.

A combination of the three methods described above was finally used to calibrate the lead glass: muon events, electron events, and lead sheet π° events. It is appropriate to describe in some detail how this was done.

Six irregularly spaced data-taking runs were devoted to muon triggers for calibration. Files were created from these data giving the average number of ADC counts for a muon event in each block for each muon run.

All of the data taking runs devoted to the neutral decay trigger recorded electron pairs, primarily from $K_L \rightarrow 3\pi^\circ$ decays. A subset of the data in which an electron was aimed at the central quarter of a block was used for calibration, and contained $\sim$500,000 electrons. A file was created giving the number of ADC counts per GeV/c of electron momentum as measured by our spectrometer, together with the number of electron events which had been used in the calculation of this number.

This file had separate entries of gain and number of events for each of 804 modules, for each of $\sim$300 runs, for each of 10 intervals of ADC counts. The intervals used were 150 counts wide, from 0 to 1500 counts, which was the high energy limit to the validity of this method due to bremsstrahlung contamination. One overall constant for the

produced a sample biased against events with any high ADC count modules, and hence was enhanced in events where one or both gammas struck near the edge or corner of a block, sharing its energy nearly equally among two or four blocks. Unfortunately, the missing block correction was tabulated as a function of energy, averaged over impact point in the block; the correction for a gamma ray hitting the edge or corner of a block is much less than that for one hitting the center. This problem was mitigated but not completely solved by requiring that both gamma rays would be determined even if all the energy in each shower were concentrated in its central block.

The three methods of calibration now had to be combined into one master gain file. The program which generated this file started with six muon gain files, the smoothed and normalized electron gain file, and ∿80,000 lead sheet π° events, roughly half in each of the two data sets.

An iteration technique was used, fitting in six intervals of ADC counts. These intervals were 0-300, 300-600, 600-900, 900-1500, 1500-2500, and 2500-4032. The first four intervals exactly covered the ADC count range of the electron gain file, and had interval boundaries which were also interval boundaries in that file. A first pass through the π° data was then made to find the total Sum of Weights array for each data set separately. To distinguish this

If the electron gain entry is undetermined and the Total Weights entry is less than 0.5, then if any electron gain entry for this module and run is determined, the one closest in ADC counts is used. If no such entry is determined, the muon gain is used.

Once all the modules in the event have been calibrated in this fashion, the mass is calculated, and for every module which was calibrated by Old Gains (and only for such modules) an updated entry is made in New Gains and Sum of Weights. One then iterates until New Gains and Old Gains converge, as previously described.

Once this lead sheet π° gain file has converged, the three gain files are combined into one master file with twelve entries in ADC counts (the ten of the electron file plus the highest two of the lead sheet π° file) for each module for each run. The gain for each entry is determined by exactly the same rules as were used to find the gain for a module hit in an event in a given run with a given number of ADC counts.

Shown in Figure 15 is the gain of a representative lead glass module as a function of ADC count interval and time. Figures 16 through 21 show the lead sheet π° mass peaks as determined by the master gain file, for all π°'s from one of our data sets and for the same events broken up into bins of different average gamma ray energy. From the

lead glass module 294, gain versus time and ADC counts

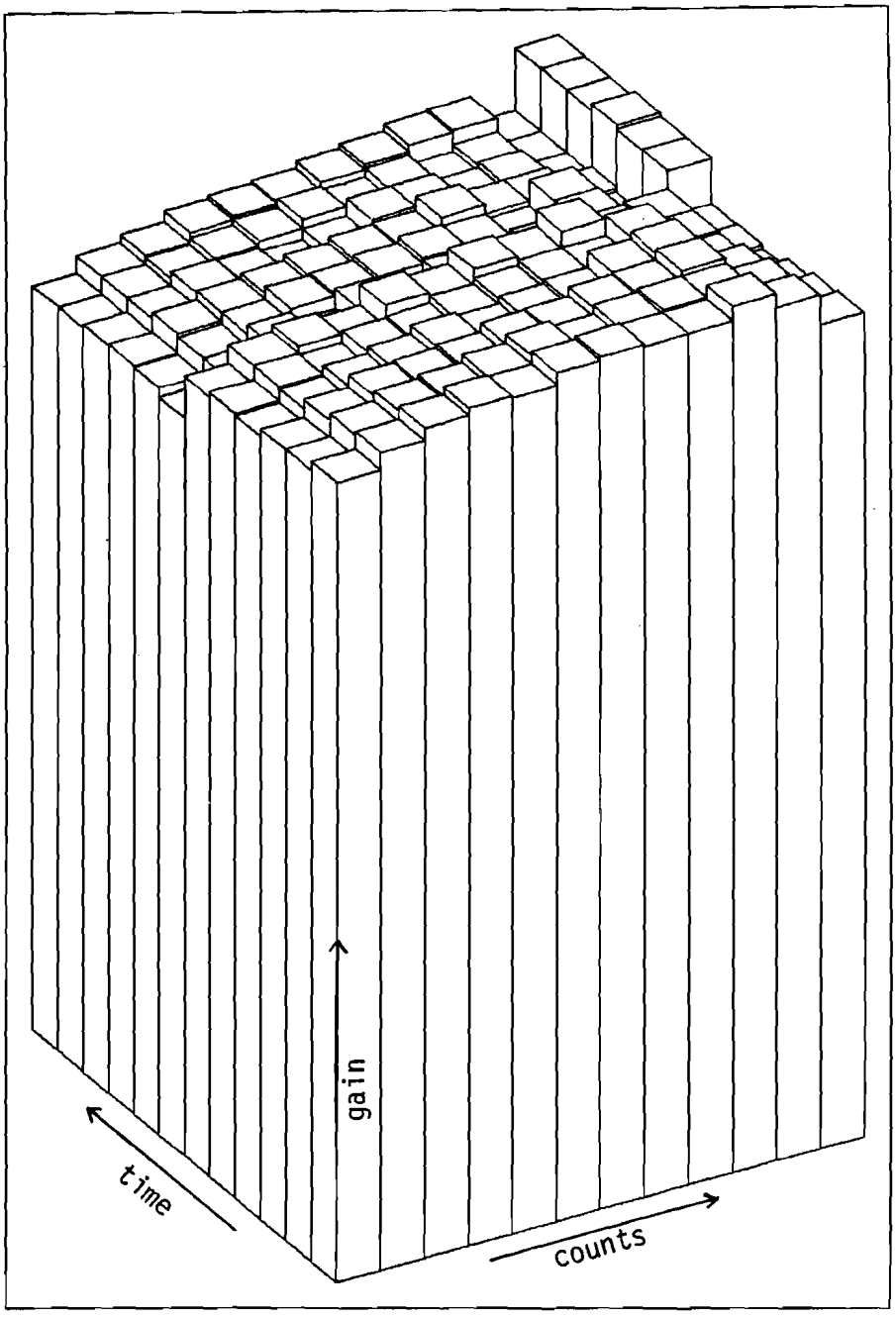

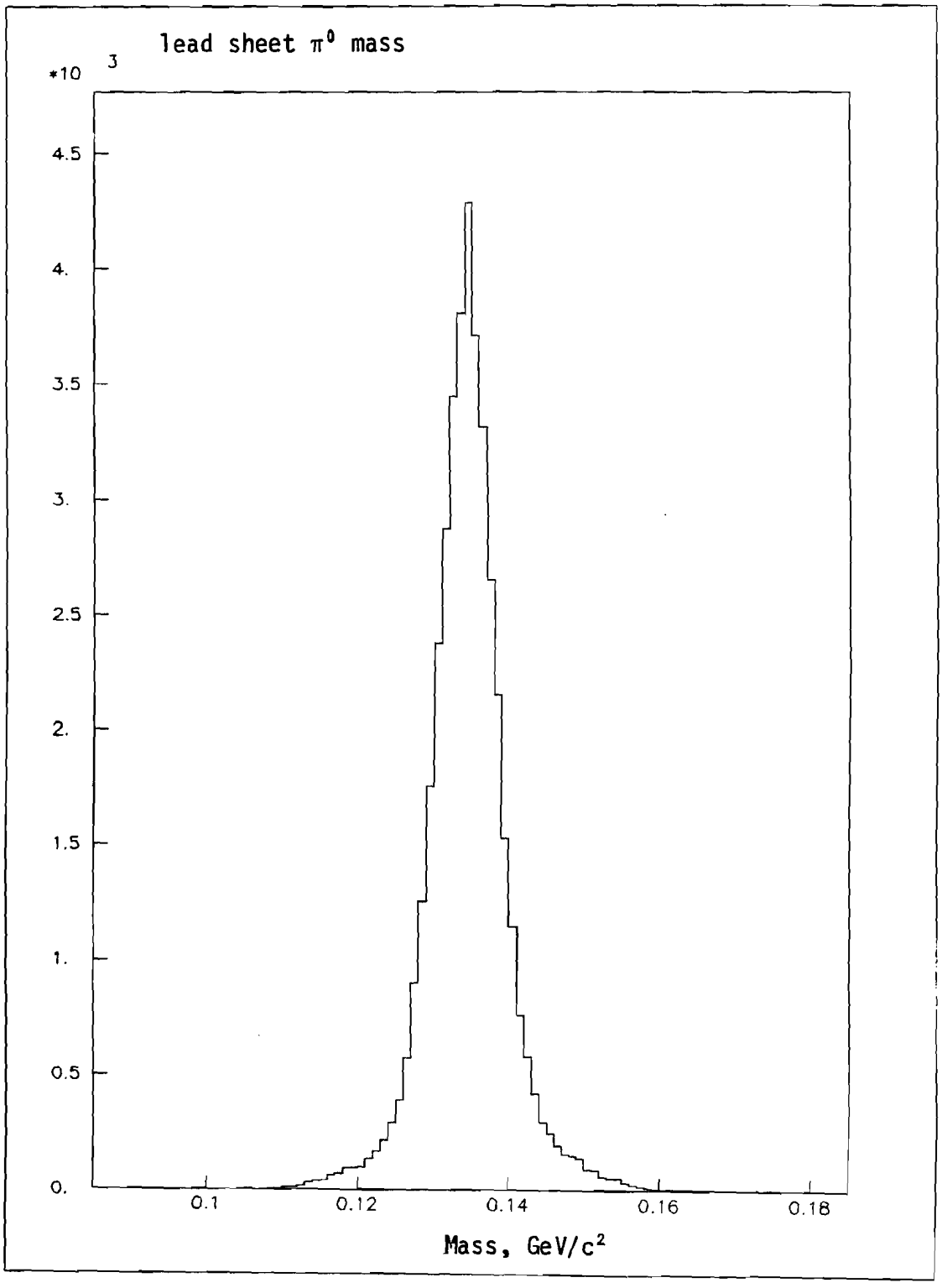
lead sheet π^0 mass
*10 3
4.5
4.
3.5
3.
2.5
2.
1.5
1.
0.5
0.
0.1
0.12
0.14
0.16
0.18
Mass, GeV/c^2

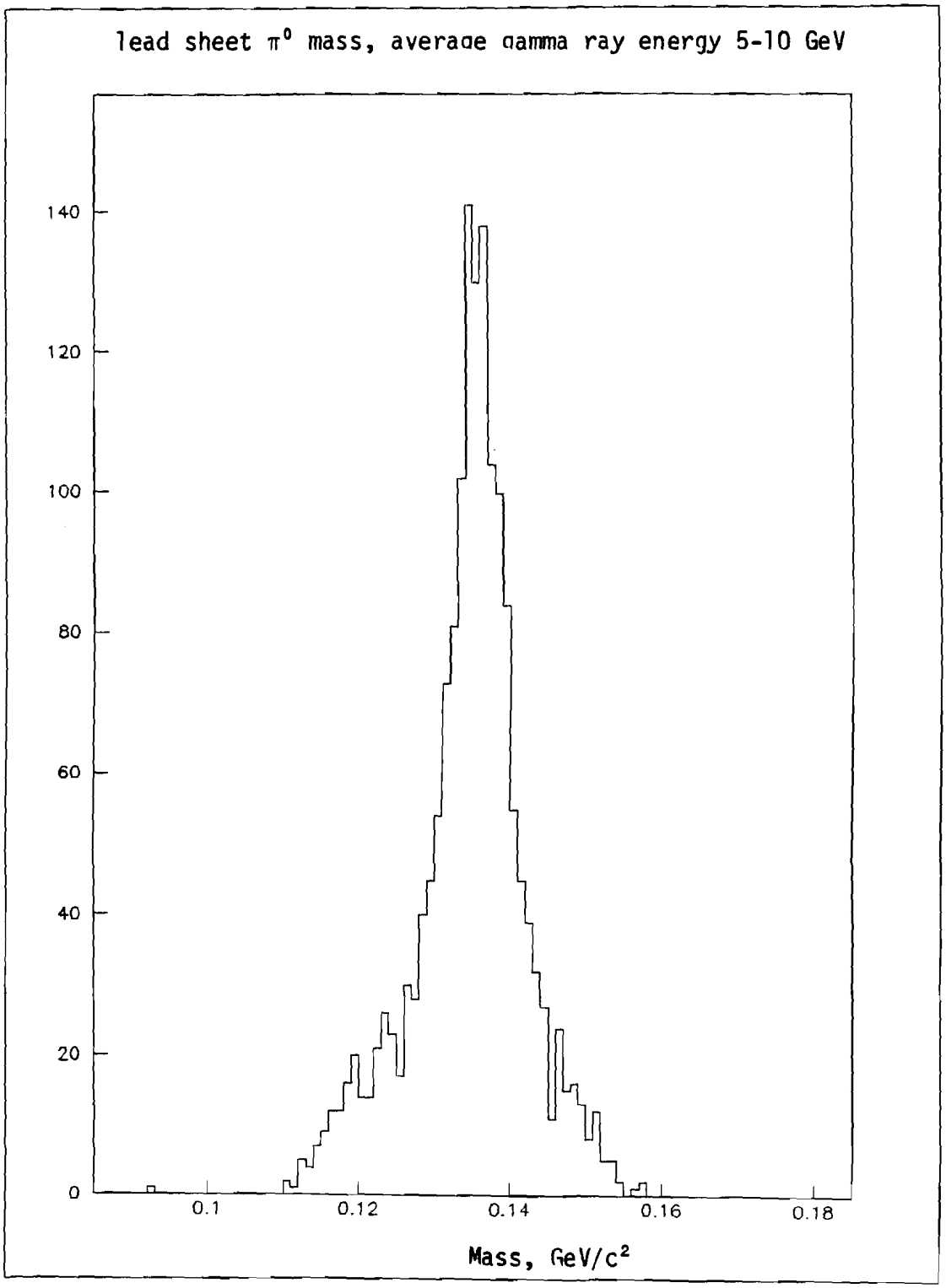
lead sheet π⁰ mass, average gamma ray energy 5-10 GeV
140
120
100
80
60
40
20
0
0.1
0.12
0.14
0.16
0.18
Mass, GeV/c²

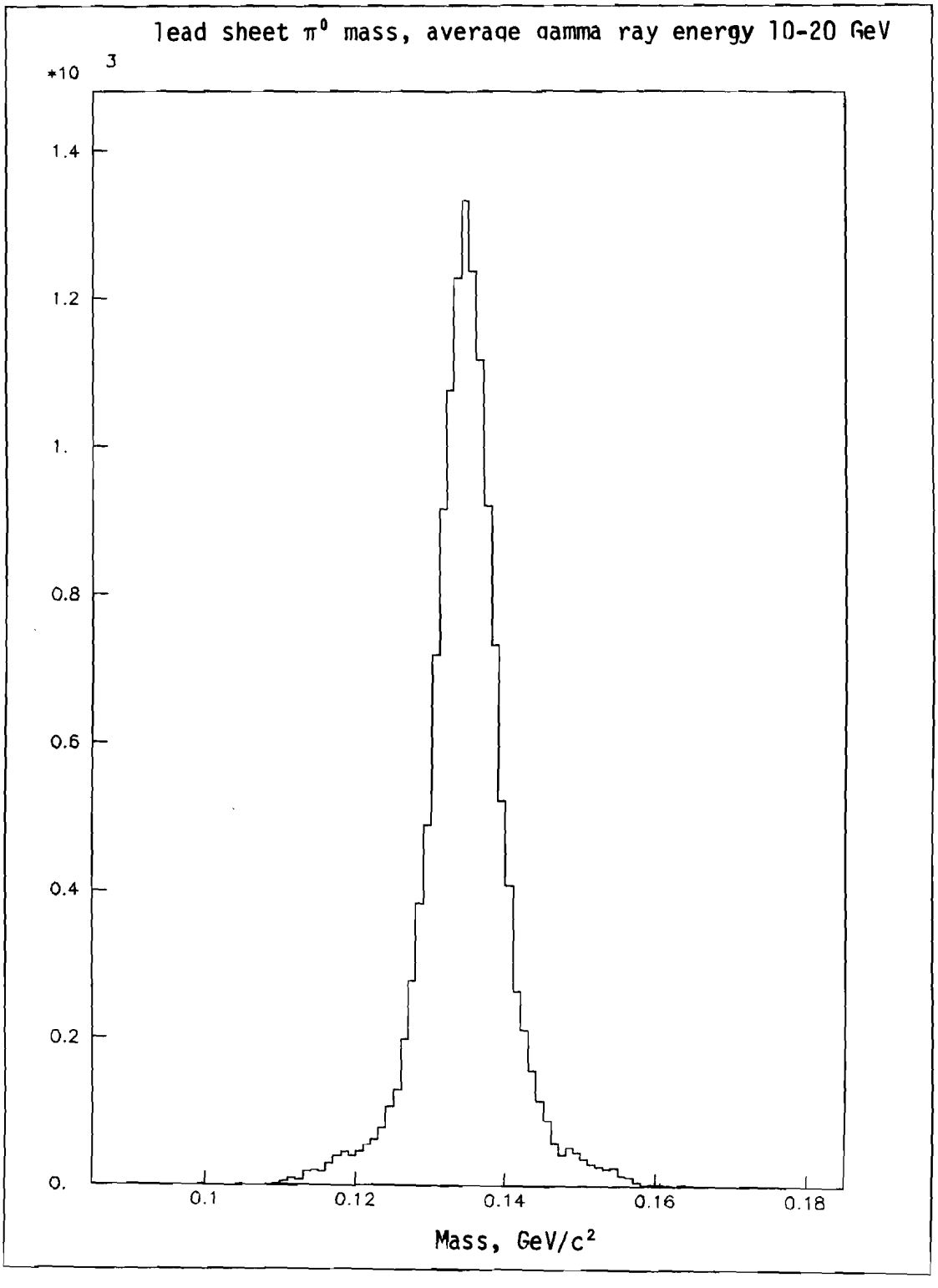
lead sheet π^0 mass, average gamma ray energy 10-20 GeV
*10 3
1.4
1.2
1.
0.8
0.6
0.4
0.2
0.
0.1
0.12
0.14
0.16
0.18
Mass, GeV/c²

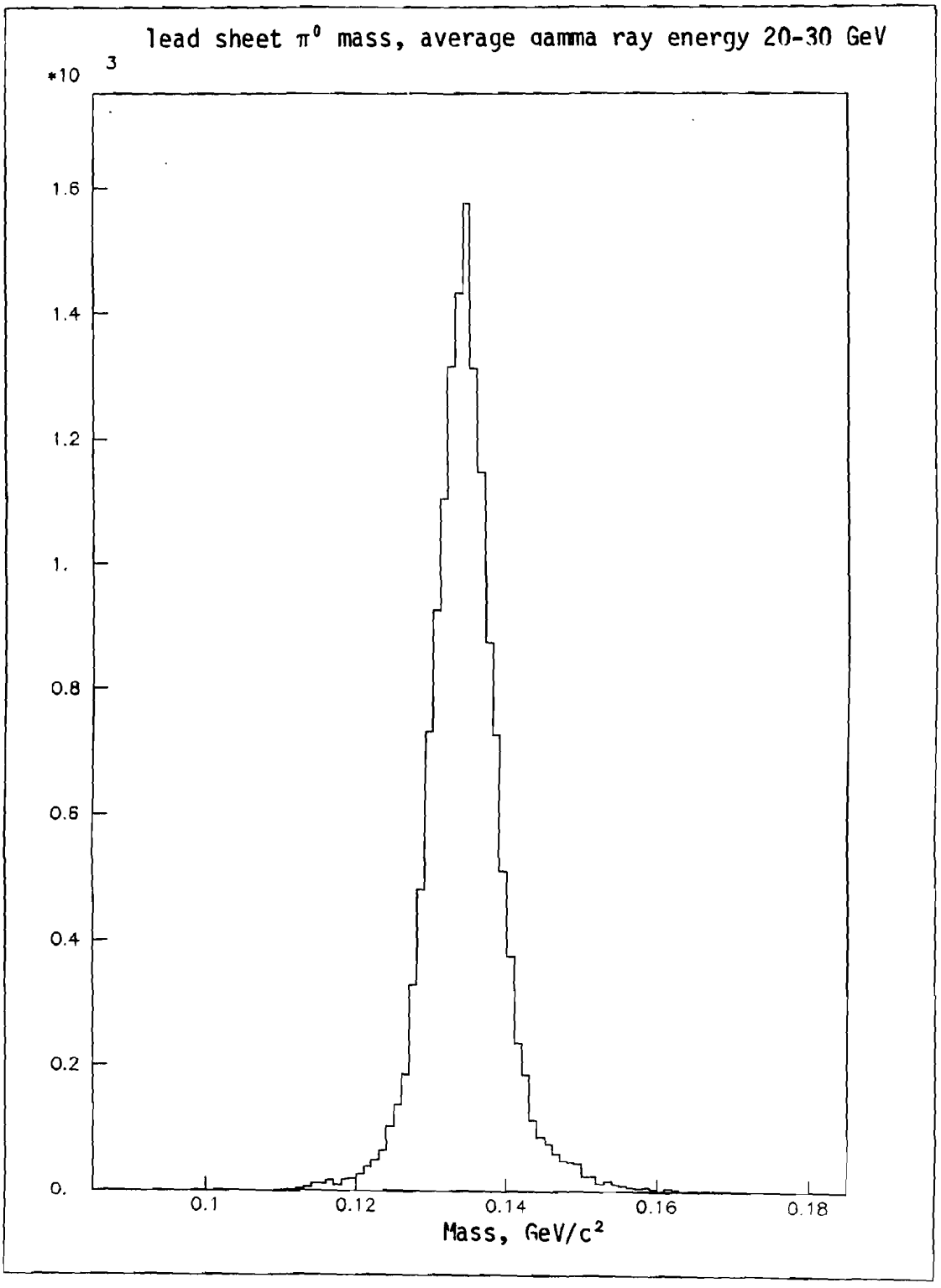
lead sheet π^0 mass, average gamma ray energy 20-30 GeV
*10 3
1.6
1.4
1.2
1.
0.8
0.6
0.4
0.2
0.
0.1
0.12
0.14
0.16
0.18
Mass, GeV/c²

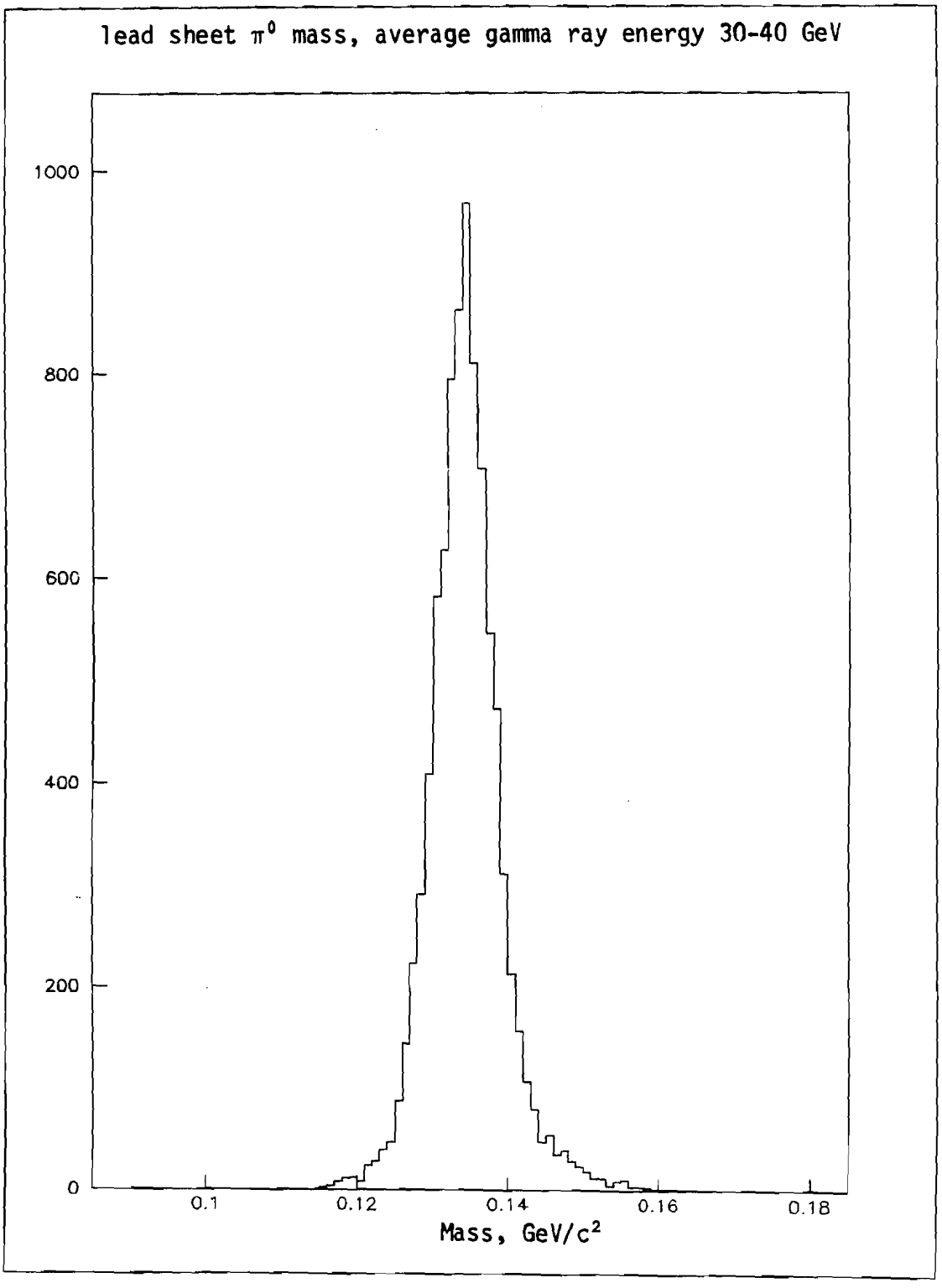
lead sheet π^0 mass, average gamma ray energy 30-40 GeV
1000
800
600
400
200
0
0.1
0.12
0.14
0.16
0.18
Mass, GeV/c^2

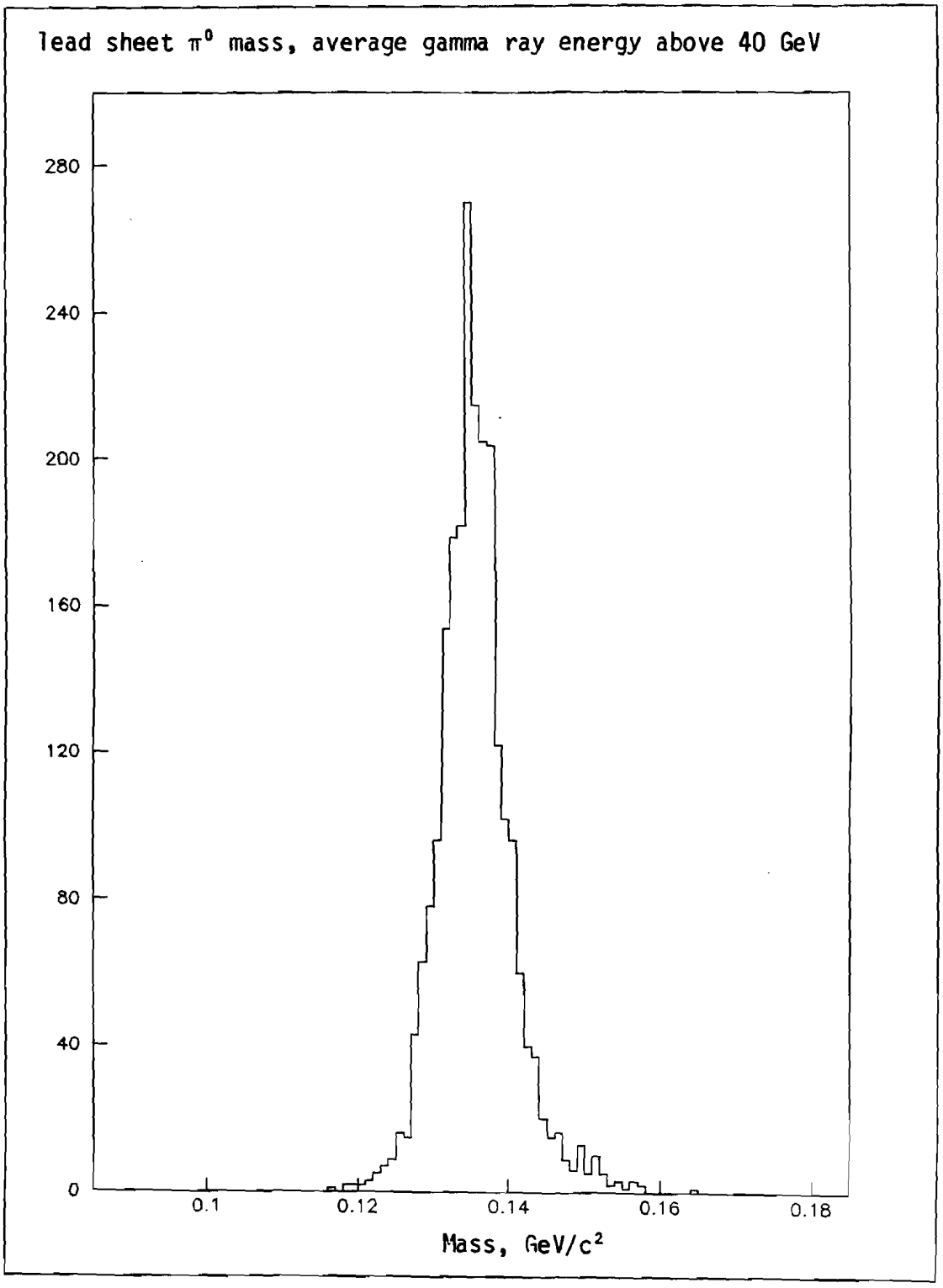
lead sheet π^0 mass, average gamma ray energy above 40 GeV
280
240
200
160
120
80
40
0
0.1
0.12
0.14
0.16
0.18
Mass, GeV/c^2

CHAPTER VI

MONTE CARLO SIMULATION OF THE ACCEPTANCE

As previously discussed, the acceptance of our apparatus for $K_L \to 3\pi^\circ$ and $K_L \to \gamma\gamma$ decays was very different. In order to find the true ratio of decay rates, this acceptance had to be calculated by a Monte Carlo simulation of the apparatus. This chapter will describe the method of the simulation; a later one will describe the results and their verification.

The Monte Carlo program generated events according to the true decay momentum spectrum and beam profile. The distribution of decay vertices over our region of non-zero acceptance was simulated according to the K_L lifetime, and the decay products were propagated through our apparatus. Multiple scattering, pair production and bremsstrahlung were simulated (electrons could make bremsstrahlung photons and those photons could pair produce, etc.) and the pair production cross section per unit radiation length was varied as a function of radiator material and photon energy. Accurate detector resolution functions were employed, and the Monte Carlo data were written to tape as raw data events, in a format indistinguishable from that written by our online PDP-11. These tapes were run through our standard analysis programs in order to determine the acceptance for a given

analysis, is given in the Appendix.

Extreme care was used in determining how many radiation lengths a particle traversed. This was important because the ratio of the acceptance of $K_L \to \gamma\gamma$ to $K_L \to 3\pi^\circ$ depended strongly on the probability that a photon would convert somewhere in our apparatus. In some cases, decay photons aimed at the calorimeter could traverse masonite boards at a grazing angle, and in such cases, the total path length in the material was calculated.

Electrons were allowed to multiple scatter and produce bremsstrahlung photons in all parts of the apparatus. These bremsstrahlung photons were allowed to convert in any part of the apparatus, although the electrons from bremsstrahlung pair production were not themselves allowed to produce bremsstrahlung photons.

Electrons followed a helical path through our analyzing magnet, after the line integral of the magnetic field had been calculated from a detailed field map. Small vertical components of the total magnet P_T kick were applied afterwards in an impulse approximation.

Gaussian multiple scattering was sufficient for our purposes, but was treated very carefully. Objects that were struck by relatively few photons, such as the wires that supported our beam pipe, were modeled accurately in space, rather than being treated as an average small thickness of material over a large area.

trigger topology requirements were met. The output of the lead glass trigger processor was modeled on the assumption that the energy deposition from a gamma ray or electron occurred at a single point in the calorimeter, and that all photomultiplier tubes were run at the same gain. The trigger processor rejected typically 30 events per million generated, and essentially all of these would have been cut in the data analysis anyway, as their kaon momentum was too low.

If an event survived the trigger, it was written to tape. The state of the scintillation counters was easy to determine, but before writing to tape, the drift chamber and lead glass data had to be simulated.

For each electron track, its transverse position at every plane of drift chamber sense wires was smeared by 220 μ, and then digitized according to a drift time versus distance function determined from the data. When all tracks had been digitized, some entries were removed from the list of wire hits due to dead time and known inefficiencies in the drift chambers.

In order to fill the list of lead glass pulse heights, an electromagnetic shower was generated according to our measured shower shape at the impact point of every electron and photon, with the appropriate normalization. These showers were then integrated over the area occupied

CHAPTER VII

DATA REDUCTION

Data reduction and analysis took place in several stages. Performing accurate track reconstruction using the drift chamber and hodoscope information proved easier than analyzing the lead glass information, and was done first.

All of our raw data tapes were analyzed for events which had two good charged tracks, and for which all lead glass and drift chamber information had been recorded without errors.

We defined two good tracks as follows: two distinct track segments had to be observed in the X-view (plan view) downstream of the analyzing magnet. Upstream of the analyzing magnet, a single X-view track was accepted, as the two tracks might not be separated enough to be resolved. The downstream and upstream track segments were required to meet in the center of the analyzing magnet. In the Y-view (elevation view) tracks were not separated by the analyzing magnet, so events with only one track apparent in this view were accepted. In both X and Y-views, the tracks were required to project back to a struck conversion hodoscope counter.

After track fitting, the analyzed compressed track

The charged tracks were projected into the lead glass, in order to determine which showers corresponded to them. The most probable pairing of tracks and showers also determined which Y-view track corresponded to a given X-view track. The momentum of the tracks was then calculated, and if either track had a reconstructed momentum less than 2/3 GeV/c, the event was cut, since the track finder had an extremely low efficiency for tracks which actually had such a low momentum.

The number of gamma rays in the event was then determined. This task was not as simple as it may sound, because a bremsstrahlung photon often accompanied the two charged tracks of the converted gamma, and in 10% of the events, an "accidental" shower, completely unrelated to the others was observed. These accidental showers were out of synchronization with the trigger, and had a monotonically falling energy spectrum, which reached nearly to zero by 3 GeV.

The most difficult gamma ray to reconstruct was the converted one. Its energy was given by adding the energy of the showers corresponding to the charged tracks plus any bremsstrahlung energy. The standard deviation due to scattering of the position of the center of energy of the electron showers was calculated, and any shower within a two standard deviation radius, which had an energy less

the rear of the lead glass. Events with either electrons or photons which struck the inner or outer ring of the lead glass array were discarded, as such events had an unknown amount of energy leak out the sides of the array. Finally, any event was discarded in which the absolute x or y coordinate of a shower at the glass was larger than the corresponding coordinate of the thick aluminum frame of the most downstream drift chamber.

Events which passed these cuts underwent further analysis before being written to disk. The first quantity calculated was the Z-vertex (distance along the beam from the lead glass) of the K_L decay, which was found by projecting the track of the converted photon back to its intersection with the kaon trajectory.

The track of the converted photon was calculated in such a way as to minimize the effects of multiple scattering. It was known which conversion hodoscope counters were struck, and this knowledge, together with the projected positions of the drift chamber tracks at the hodoscope, gave a most probable point at the hodoscope plane. Then, the drift chamber tracks were projected to the six foot thin window, which was a source of considerable scattering, to obtain the most probable point there. These two points determined the converted photon trajectory.

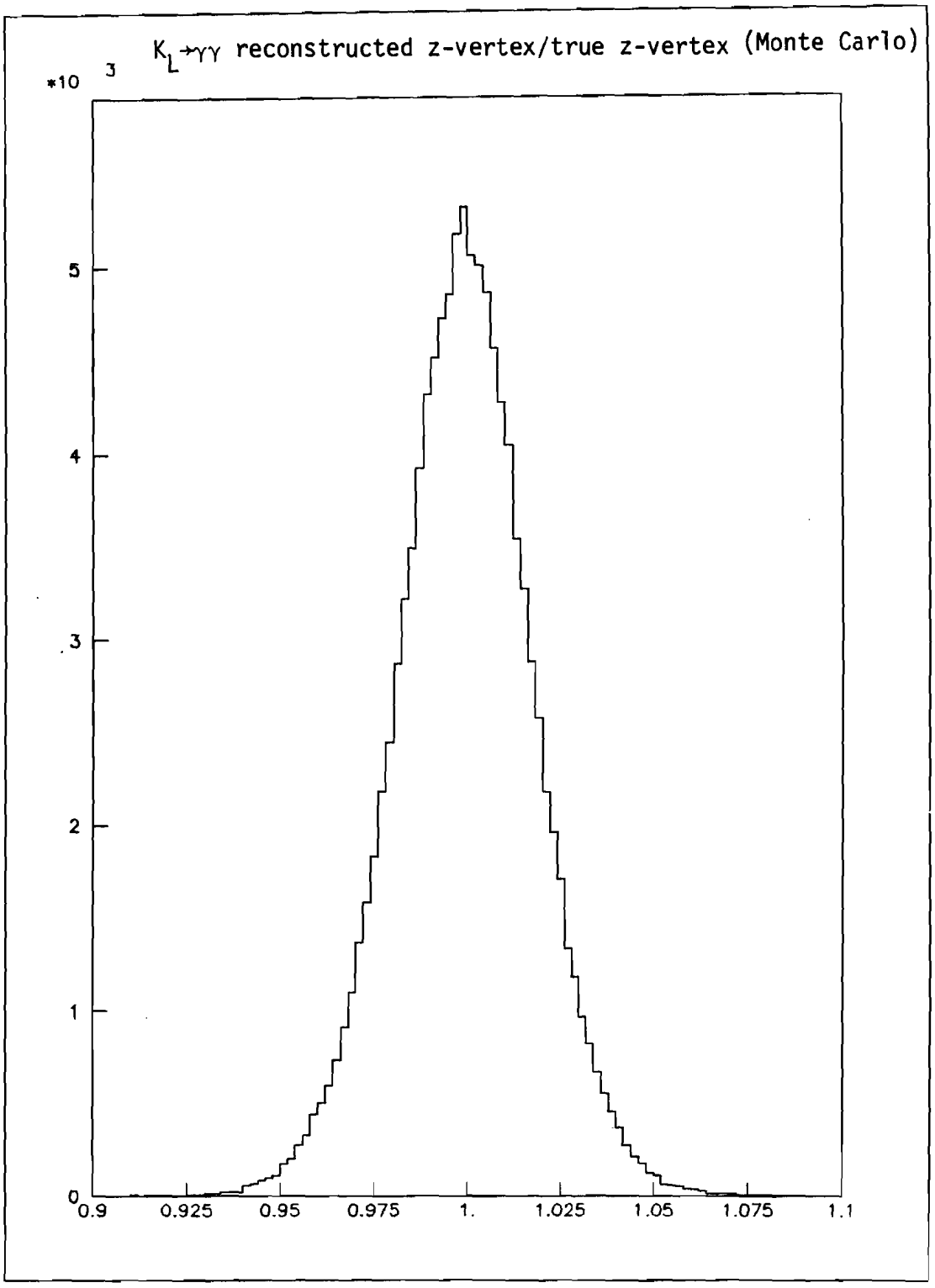
$K_L \to \gamma\gamma$ reconstructed z-vertex/true z-vertex (Monte Carlo)
*10 3
5
4
3
2
1
0
0.9
0.925
0.95
0.975
1.
1.025
1.05
1.075
1.1

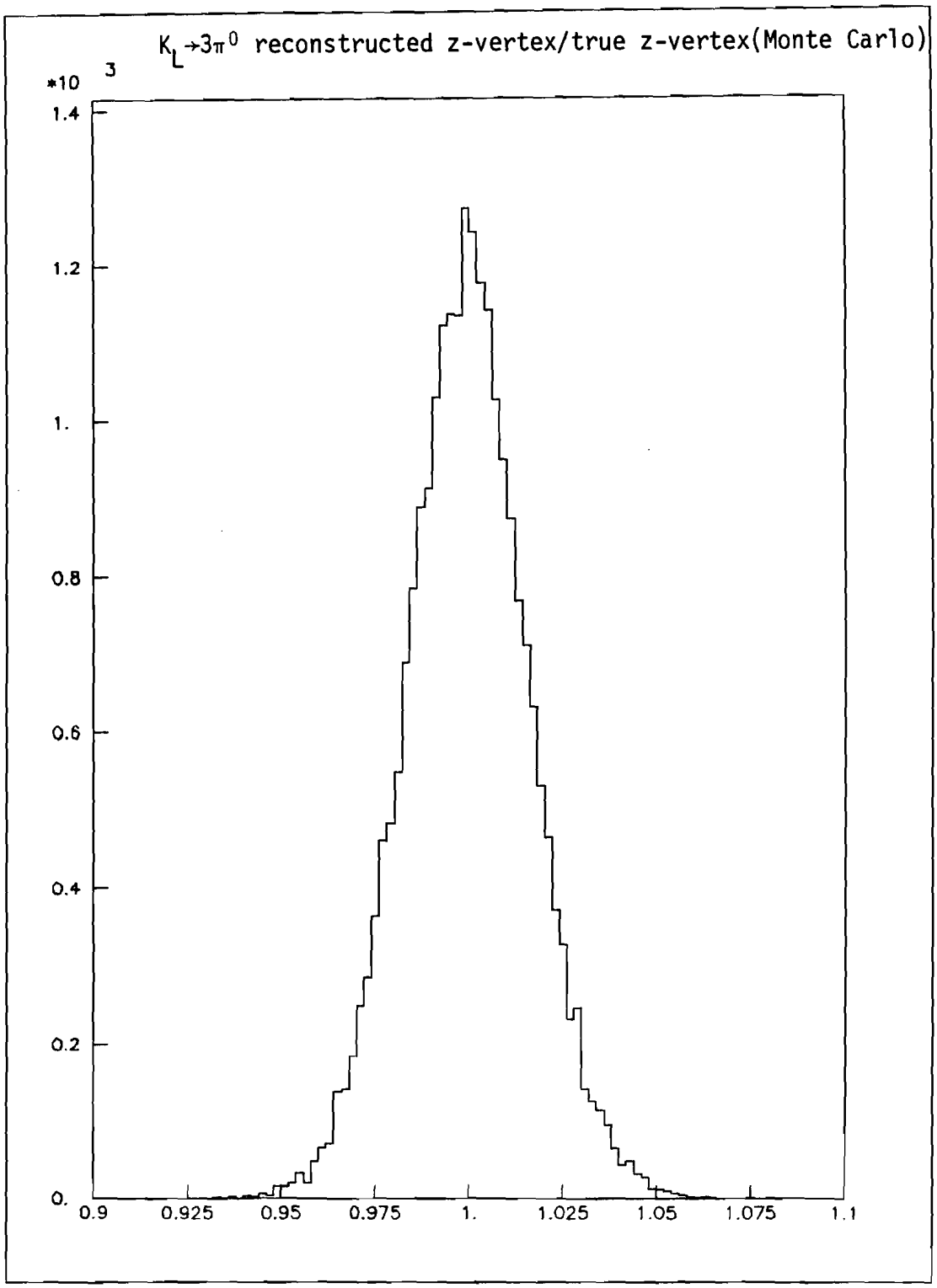
$K_L \to 3\pi^0$ reconstructed z-vertex/true z-vertex(Monte Carlo)
*10 3
1.4
1.2
1.
0.8
0.6
0.4
0.2
0.
0.9
0.925
0.95
0.975
1.
1.025
1.05
1.075
1.1

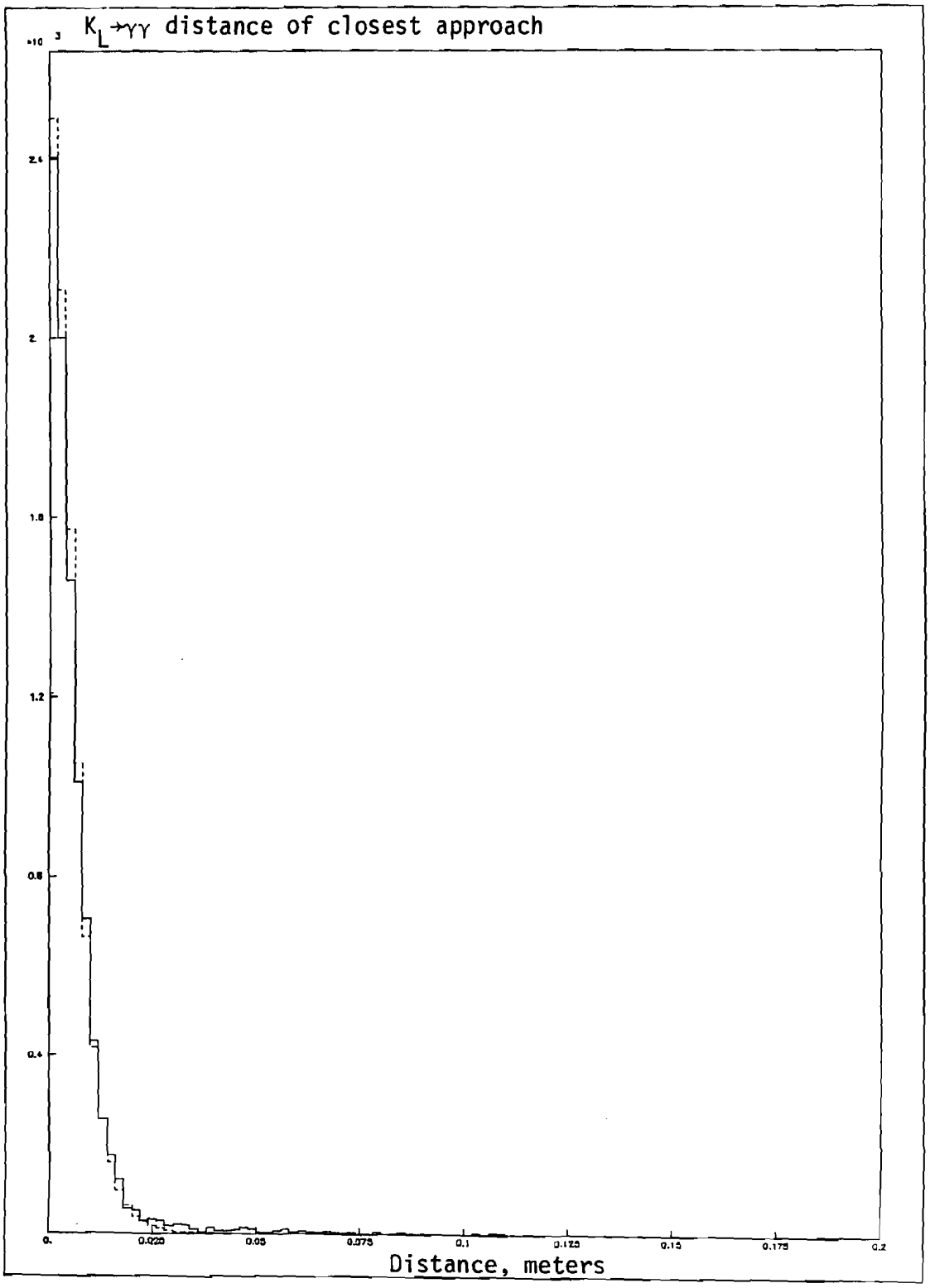
$K_L \to \gamma\gamma$ distance of closest approach
×10 3
2.4
2.
1.6
1.2
0.8
0.4
0.
0.025
0.05
0.075
0.1
0.125
0.15
0.175
0.2
Distance, meters

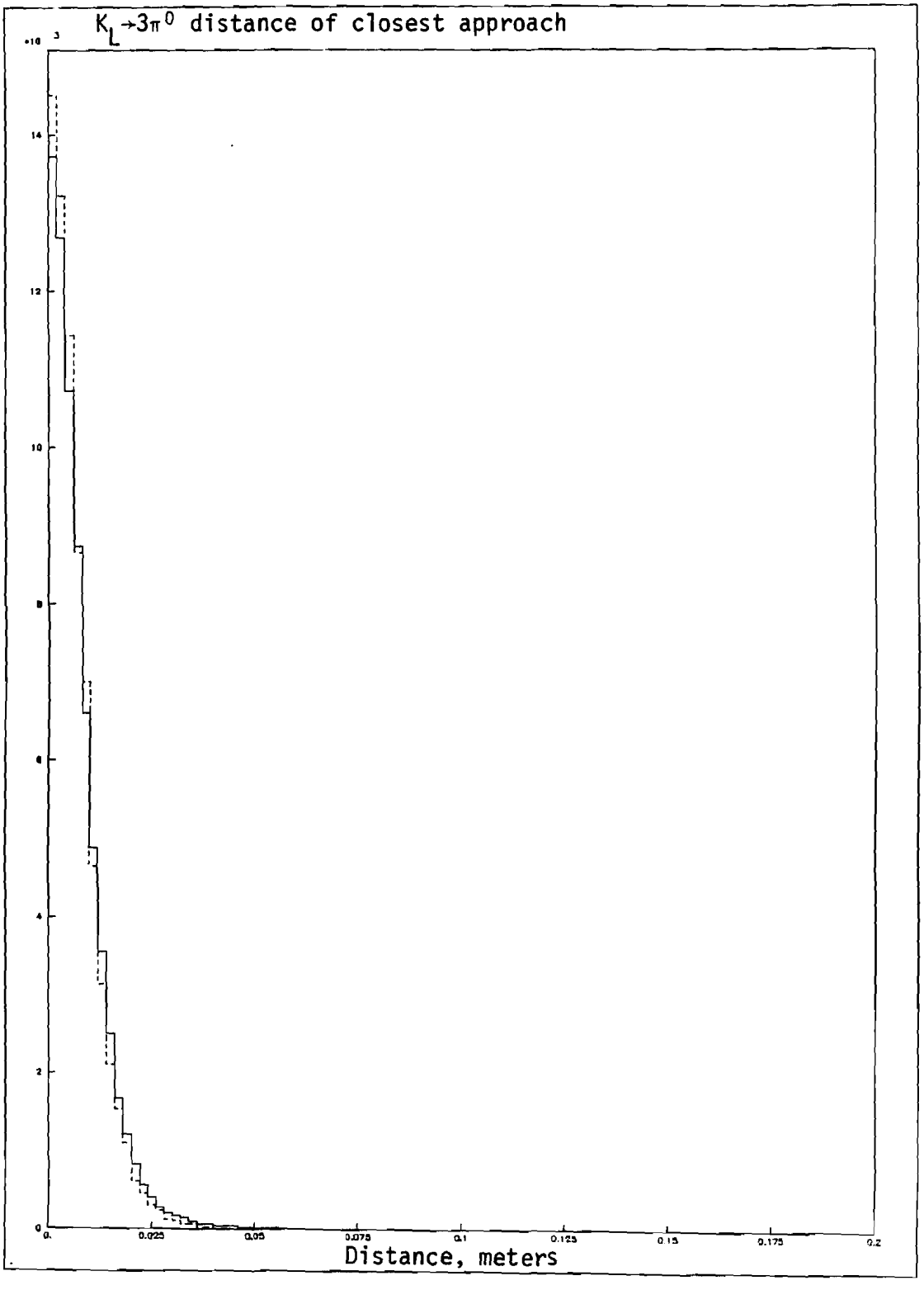
$K_L \rightarrow 3\pi^0$ distance of closest approach
x10 3
14
12
10
8
6
4
2
0
0.
0.025
0.05
0.075
0.1
0.125
0.15
0.175
0.2
Distance, meters

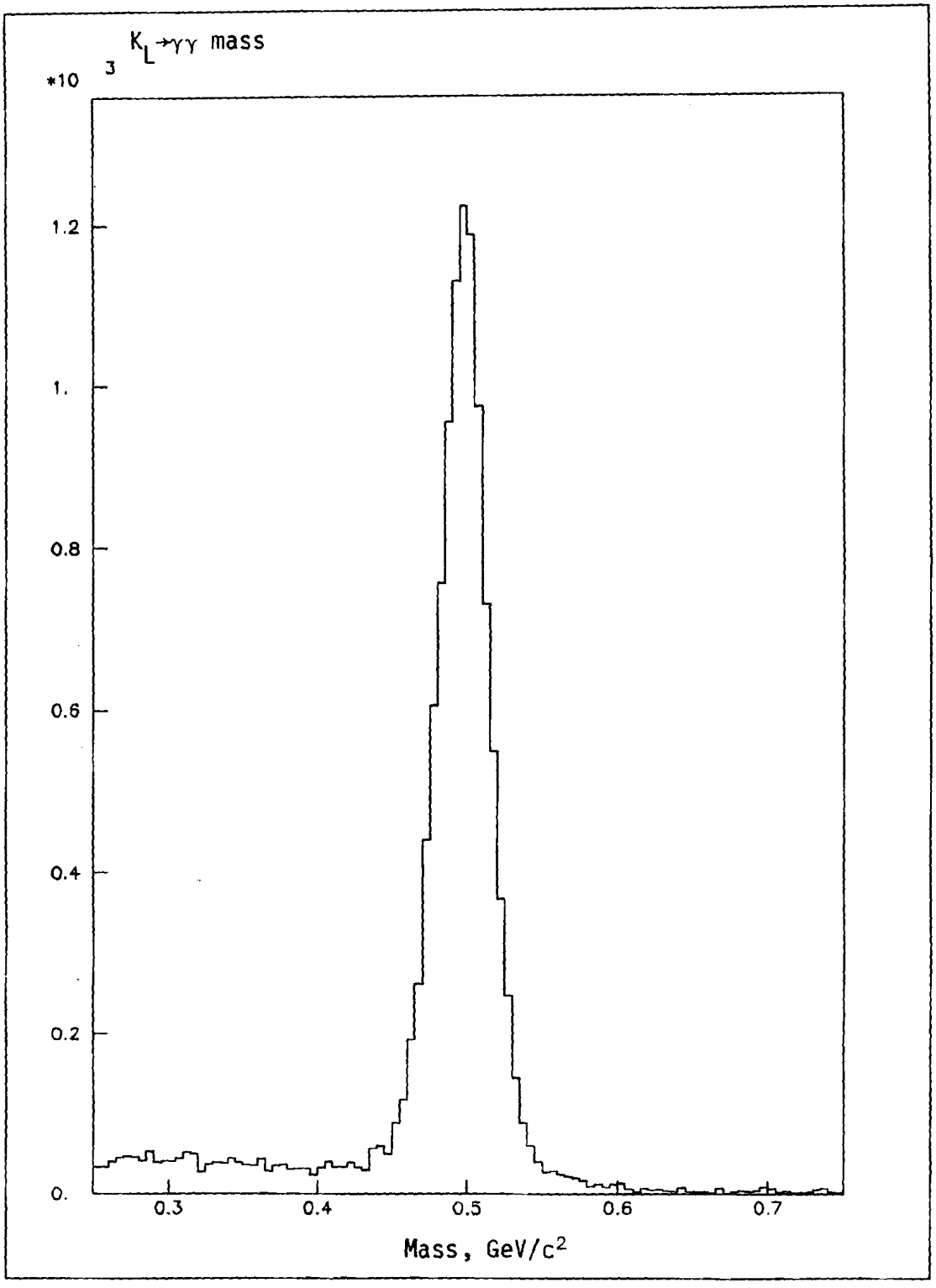
$K_L \to \gamma\gamma$ mass
*10 3
1.2
1.
0.8
0.6
0.4
0.2
0.
0.3
0.4
0.5
0.6
0.7
Mass, GeV/c^2

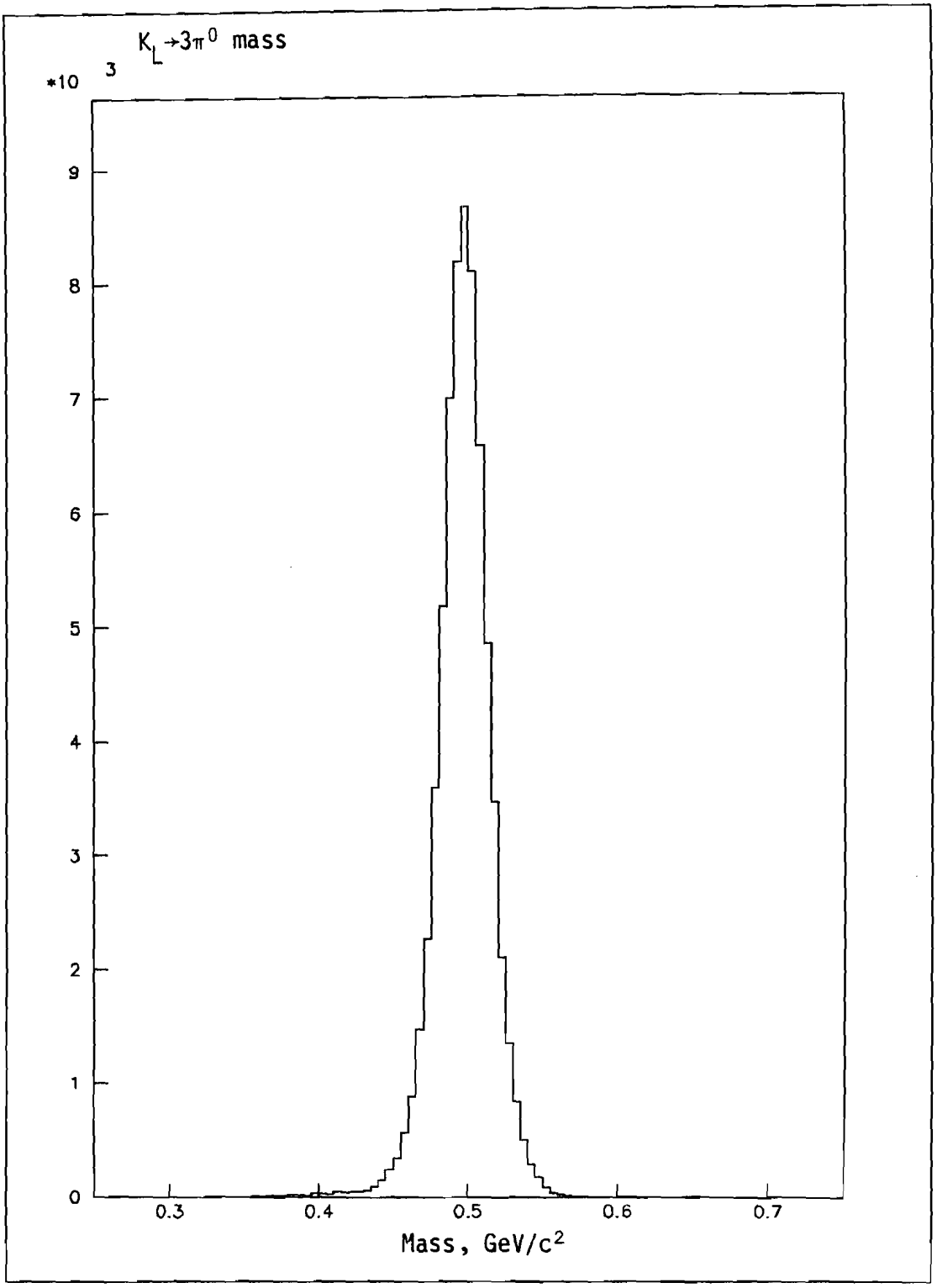
$K_L \to 3\pi^0$ mass
*10 3
9
8
7
6
5
4
3
2
1
0
0.3
0.4
0.5
0.6
0.7
Mass, GeV/c^2

function as follows:

$$\chi^2 = \left(\frac{m_1 - m_{\pi^\circ}}{m_{\pi^\circ} \times 0.047}\right) + \left(\frac{m_2 - m_{\pi^\circ}}{m_{\pi^\circ} \times 0.047}\right) + \left(\frac{m_3 - m_{\pi^\circ}}{m_{\pi^\circ}\sqrt{0.047^2 + \text{XTERM}}}\right)^2$$

where m_1 and m_2 are the invariant masses of the gamma ray pairs not involving the converted photon, m_3 is the mass of the pair which includes the converted photon, and m_{π° is the known mass of the pion, 134.96 MeV/c^2. The quantity labeled XTERM accounts for the small additional error in the mass determination of the gamma ray pair containing the converted photon, due to multiple scattering of the electrons in our apparatus. This extra error is defined:

$$\text{XTERM} = \frac{0.1}{R^2 * (E_{e_1}^2 + E_{e_2}^2)}$$

where R is the distance at the lead glass between the two gamma rays, E_{e_1} is the energy of one of the electrons from the converted gamma, and E_{e_2} is the energy of the other.

The best of the fifteen pairings could be found by minimizing this chi-squared function. Chi-squared for the best pairing of good $K_L \to 3\pi^\circ$ events is shown in Figure 28. The long tail in this and in the distance of closest approach plot for $K_L \to 3\pi^\circ$ events is due to the presence of accidental showers superimposed on one of the true gamma rays.

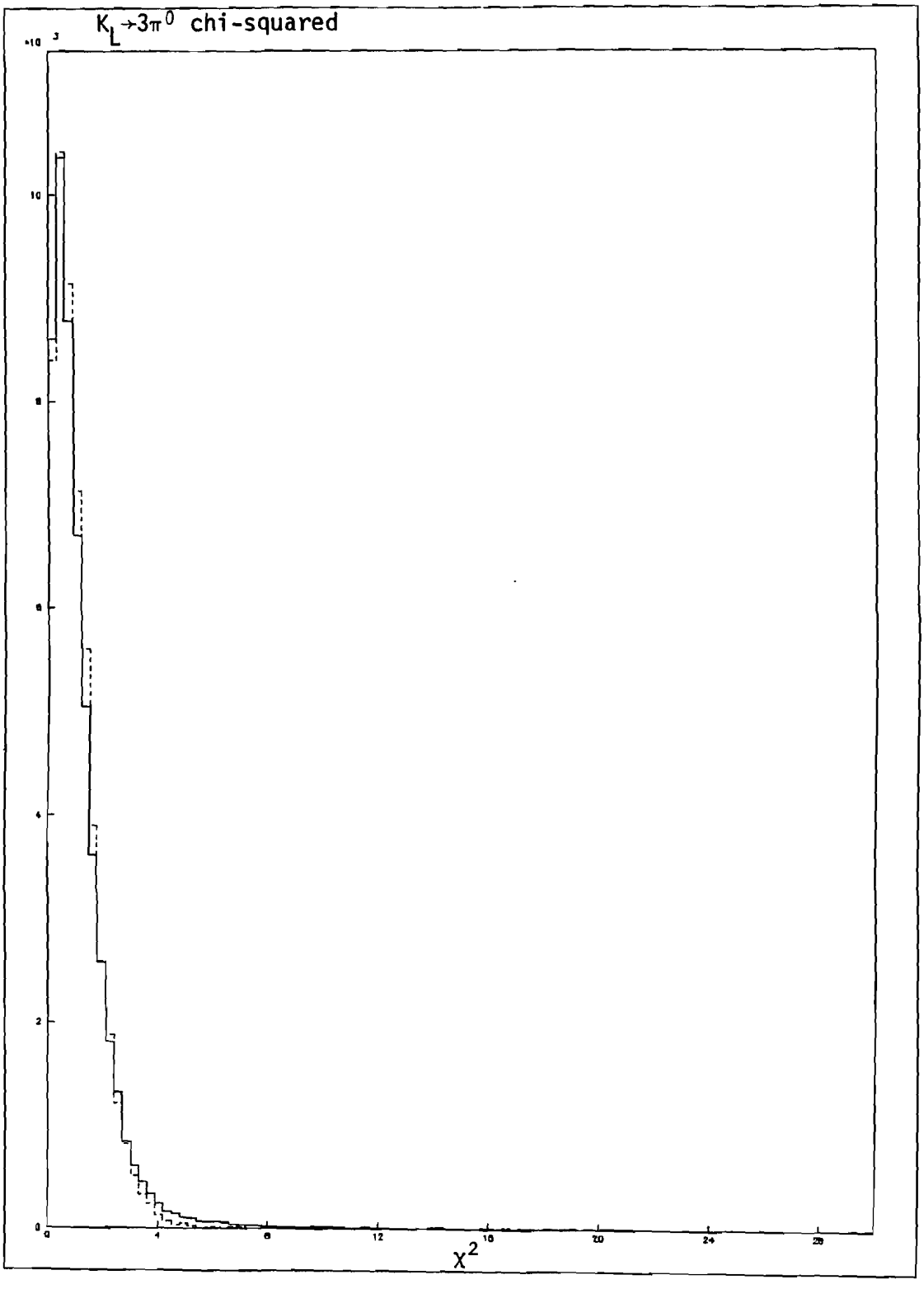
$K_L \to 3\pi^0$ chi-squared
χ^2

CHAPTER VIII

VERIFICATION OF THE MONTE CARLO

Given the importance of the acceptance of the spectrometer in the calculation of the $K_L \to \gamma\gamma$ branching ratio, one must verify that the Monte Carlo program used to calculate the acceptance was working properly. This chapter will compare various distributions in both data and Monte Carlo and demonstrate that the simulation was indeed quite accurate. Verification will come primarily from $K_L \to 3\pi^\circ$ events, where essentially no background was present, after fairly loose cuts on chi-squared, distance of closest approach and mass. The agreement between data and Monte Carlo for $K_L \to \gamma\gamma$ events is also quite good when allowance is made for the $\sim$10% background.

At this point, one must mention several caveats. The calibration of the lead glass was measurably imperfect. While any remaining nonlinearities were not directly observable in $3\pi^\circ$ data, a small quadratic nonlinearity of 0.0004/GeV was observed in $K_L \to \gamma\gamma$ data, which has a very different gamma ray energy spectrum. Both types of events had their reconstructed decay vertices shifted systematically by $\sim$25 cm from the correct Z-vertex, as measured by the reconstructed position of the conversion hodoscope. These problems have been corrected in the comparison of data

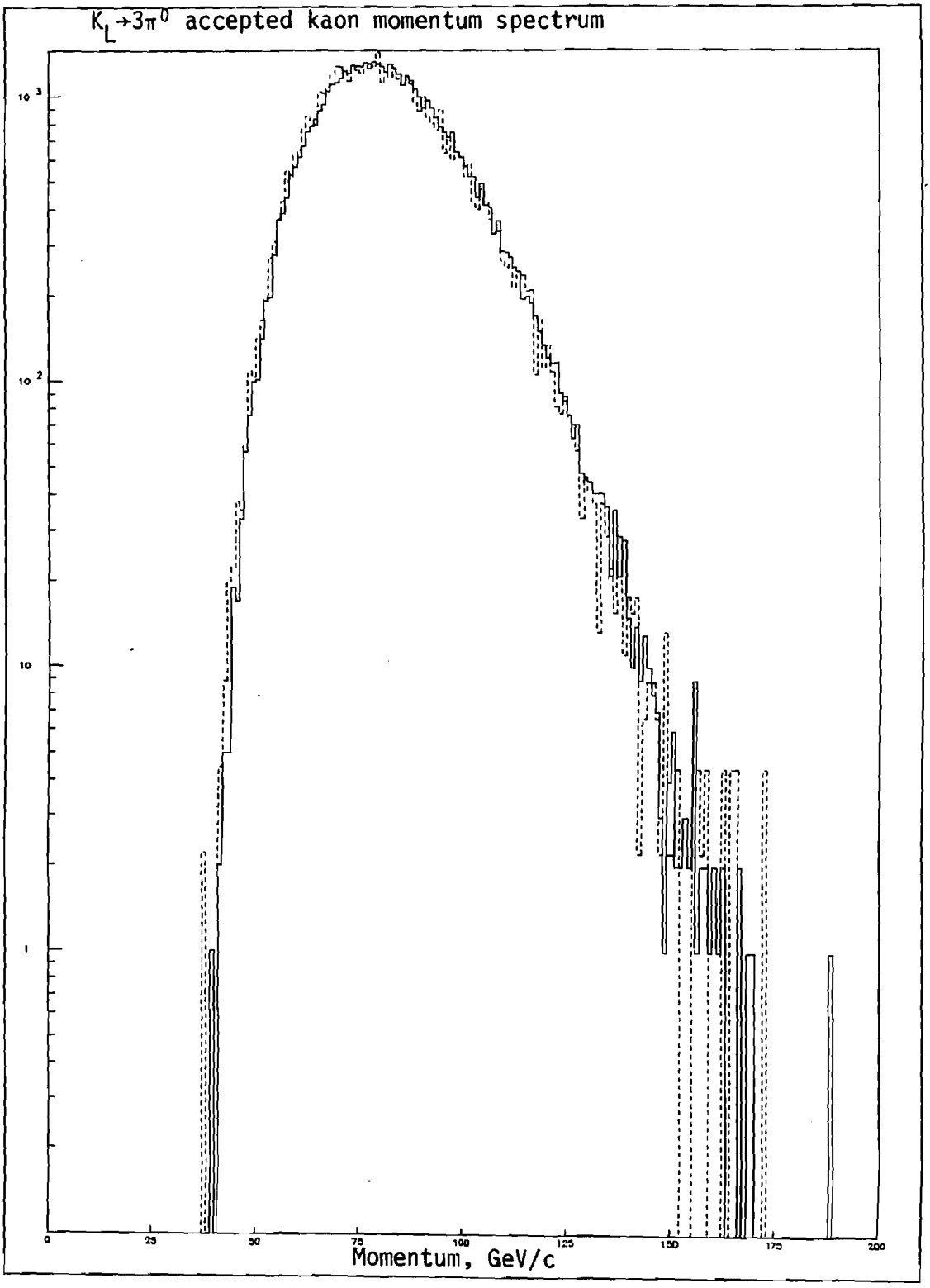
$K_L \rightarrow 3\pi^0$ accepted kaon momentum spectrum
10^3
10^2
10
1
0
25
50
75
100
125
150
175
200
Momentum, GeV/c

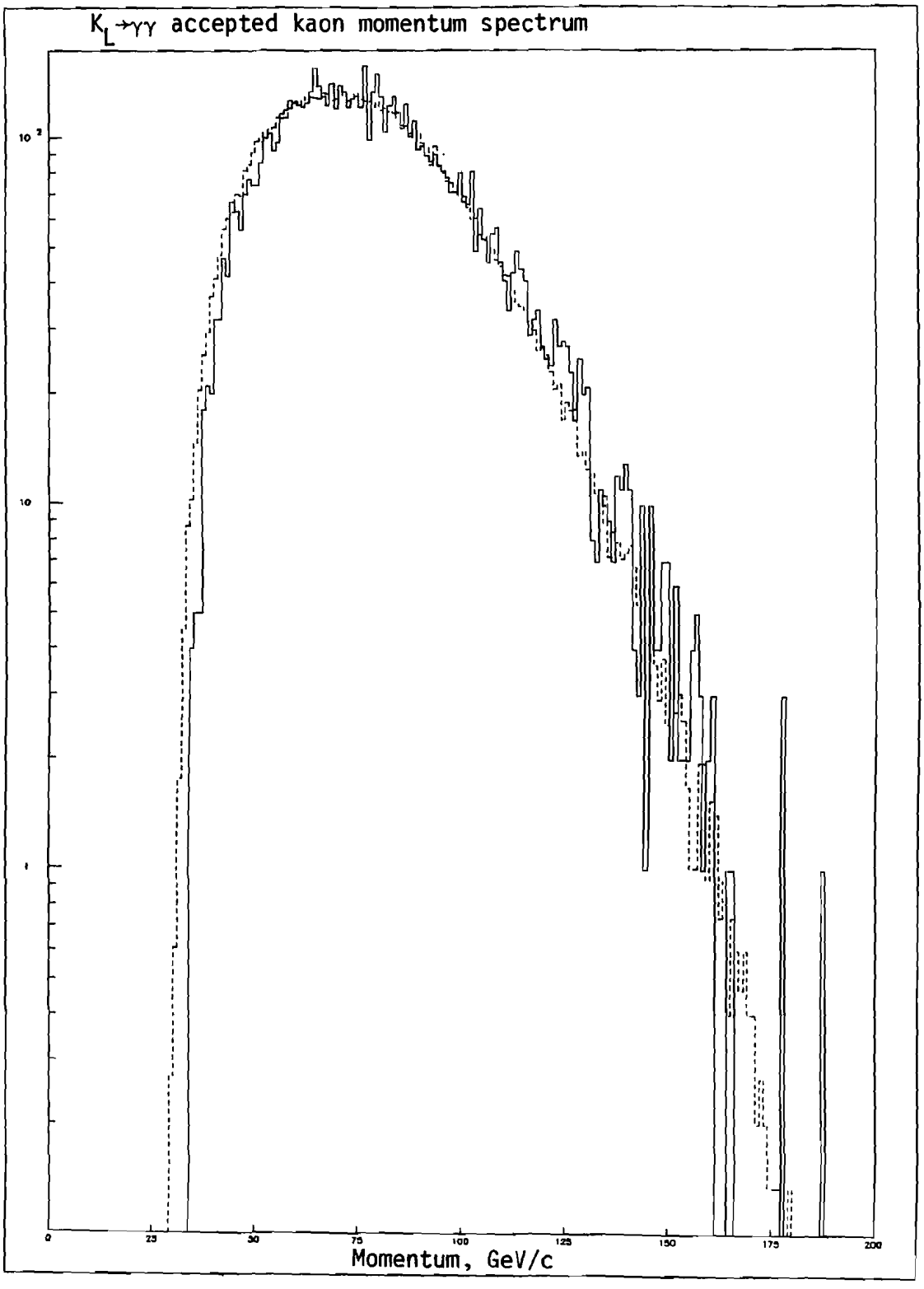
$K_L \to \gamma\gamma$ accepted kaon momentum spectrum
10^2
10
1
0
25
50
75
100
125
150
175
200
Momentum, GeV/c

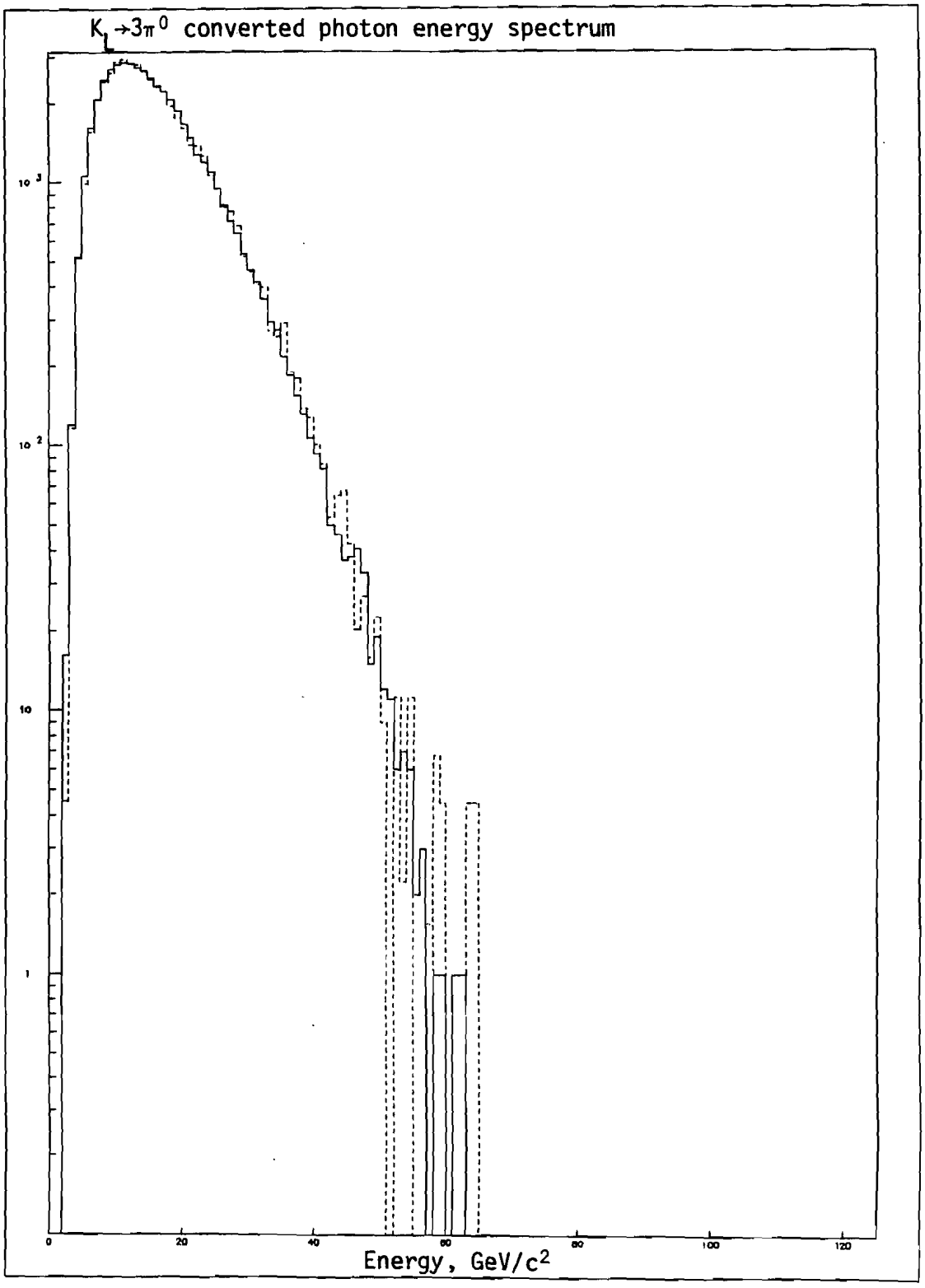
$K_L \to 3\pi^0$ converted photon energy spectrum
10^3
10^2
10
1
0
20
40
60
80
100
120
Energy, GeV/c^2

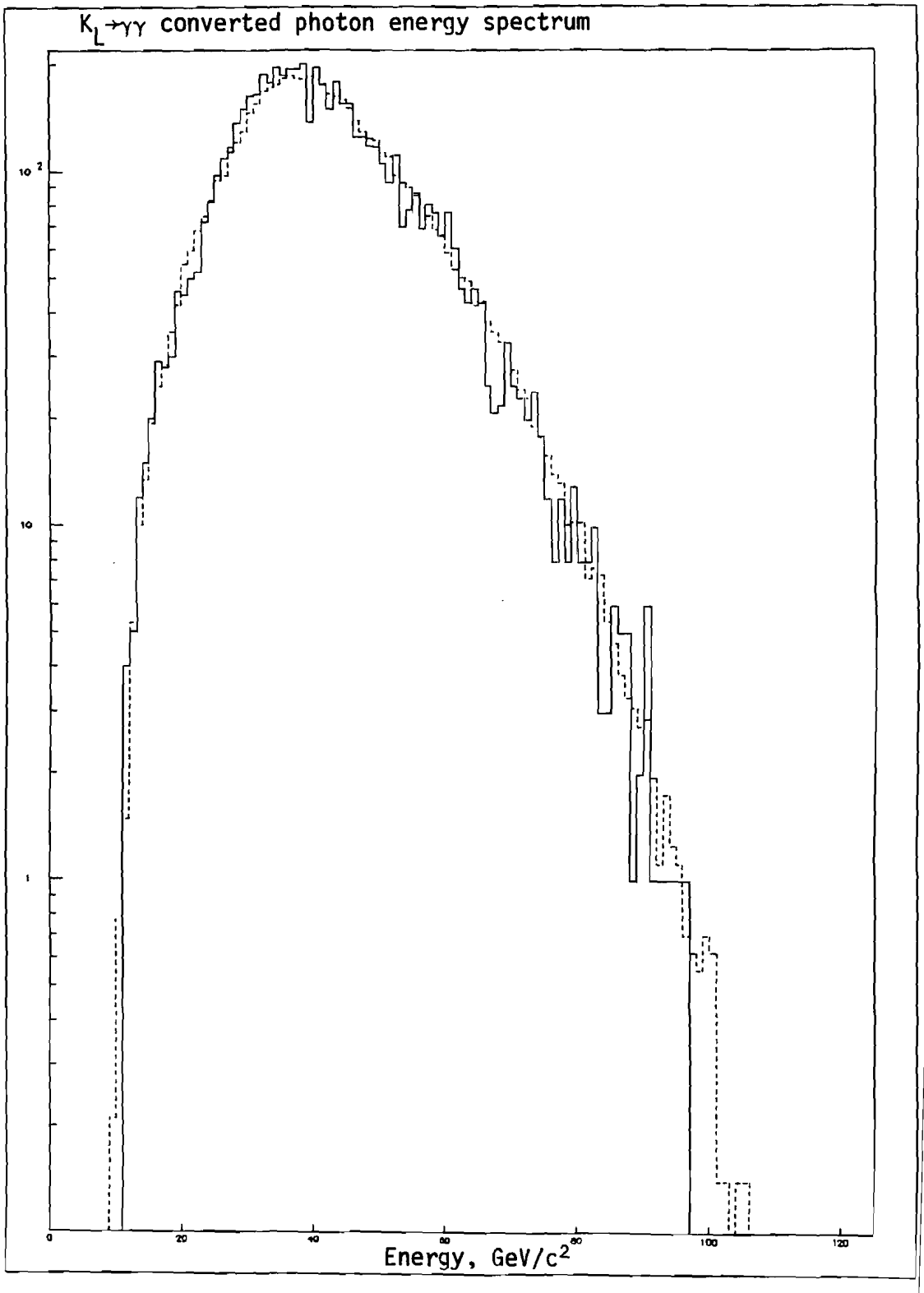
$K_L \to \gamma\gamma$ converted photon energy spectrum
10^2
10
1
0
20
40
60
80
100
120
Energy, GeV/c^2

Figures 33 and 34 show the unconverted photon spectra. These verify the acceptance for gamma rays.

It will be shown to be important in the data analysis that one make a cut on the distance between two neighboring showers in the lead glass. The shower finding program cannot tell to which shower to assign energy deposited in a region of shower overlap. Since this problem does not exist in $K_L \to \gamma\gamma$ events, which have two gamma rays on opposite sides of the beam pipe, one must eliminate events with shower overlap in $K_L \to 3\pi^\circ$ events if they are to be treated similarly. Figures 35 and 36 show the distance between the nearest pair of unconverted gamma ray showers, or an unconverted gamma ray and a charged track. (The distance between two charged tracks does not matter, as their energy is summed.)

Figures 37 and 38 show the Z-vertex (distance of decay vertex from lead glass) distribution for good $3\pi^\circ$ and 2γ events. This shows that the acceptance is understood even for events whose decay products must pass through the regenerator-sweeping magnet assembly, located $\sim$74 meters from the lead glass.

Figures 39 and 40 show the "true" Z-vertex superimposed on the reconstructed Z-vertex in Monte Carlo, in order to show the effects of smearing.

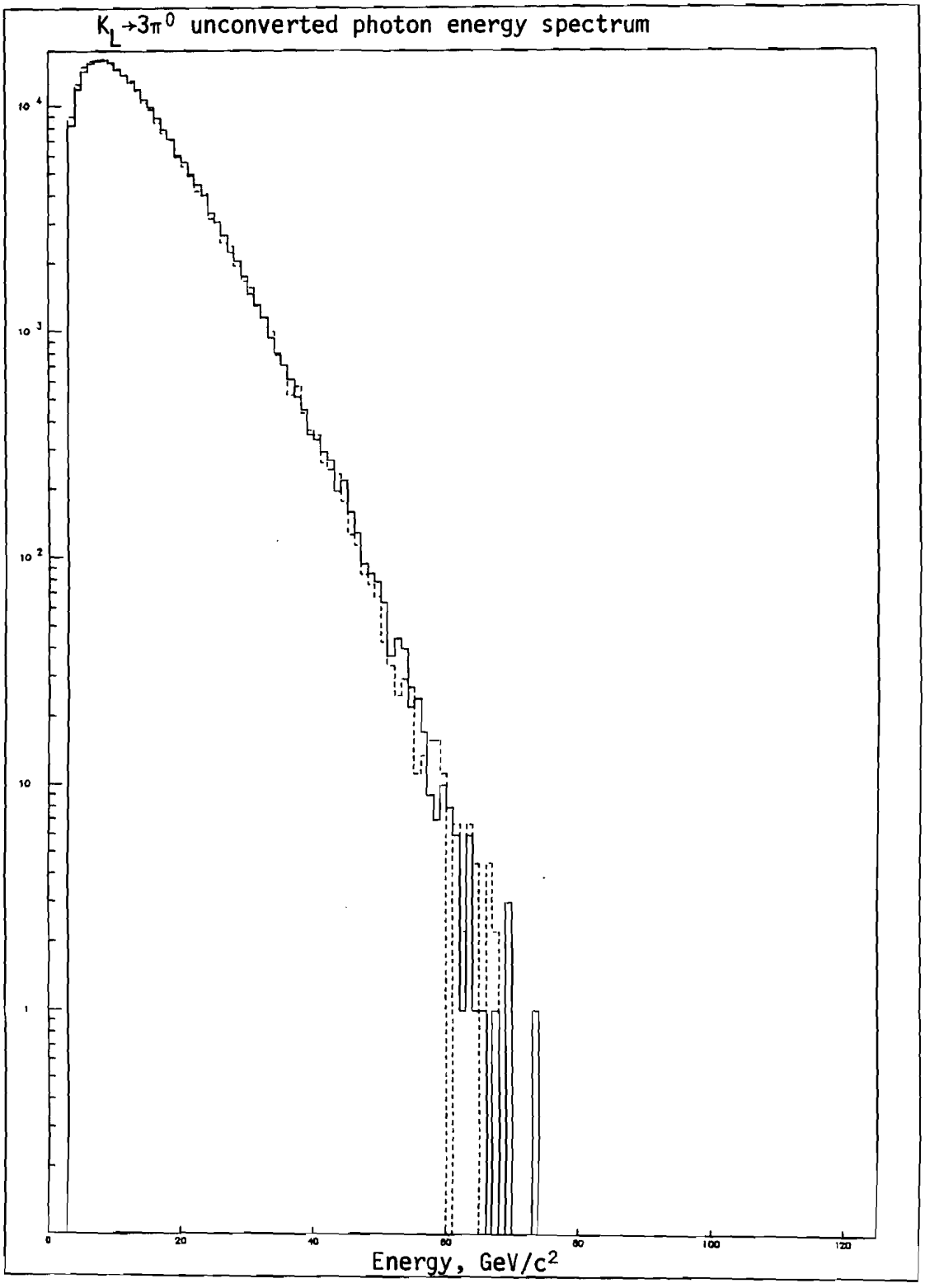
$K_L \to 3\pi^0$ unconverted photon energy spectrum
10^4
10^3
10^2
10
1
0
20
40
60
80
100
120
Energy, GeV/c^2

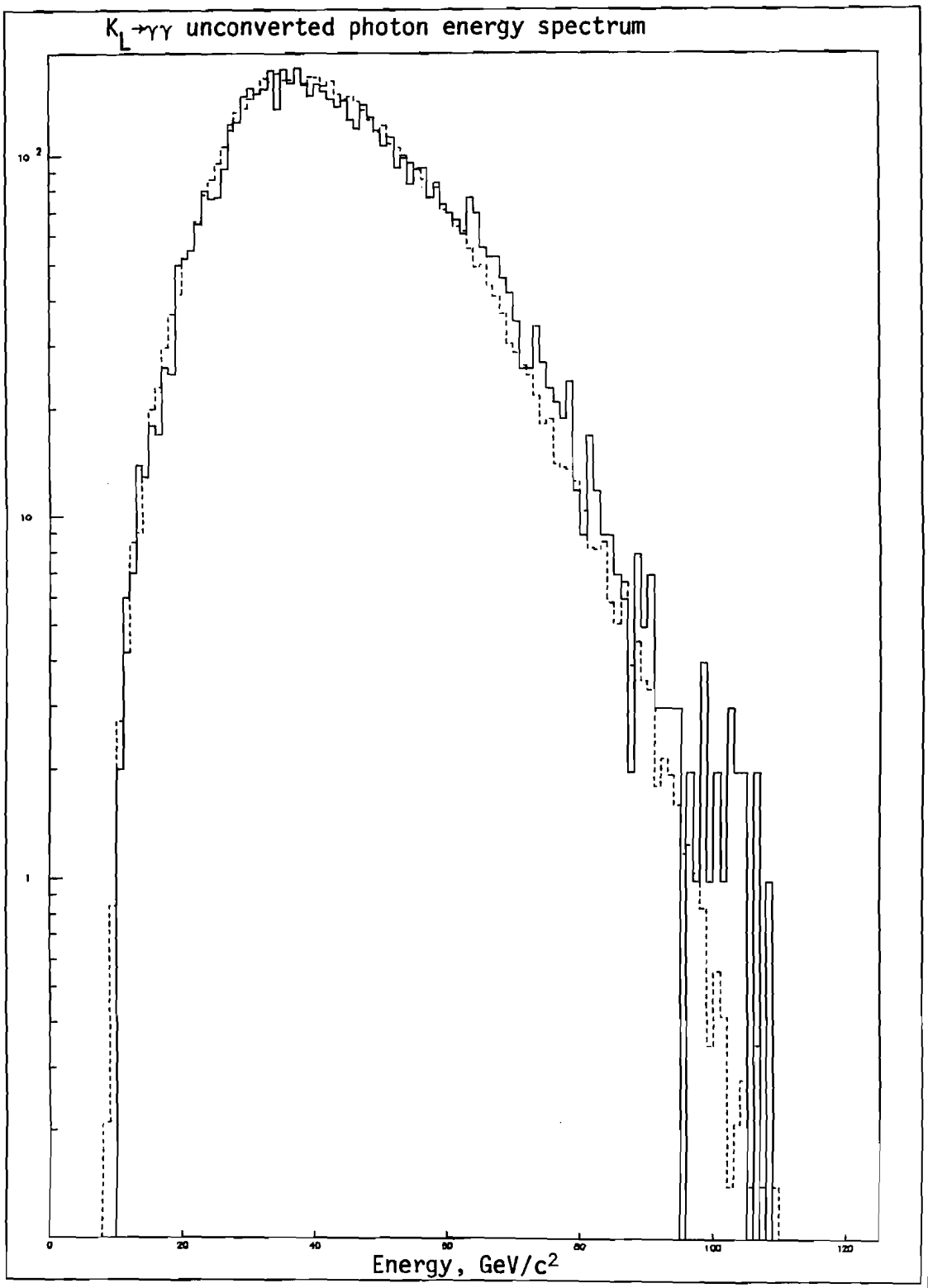
$K_L \to \gamma\gamma$ unconverted photon energy spectrum
10^2
10
1
0
20
40
60
80
100
120
Energy, GeV/c^2

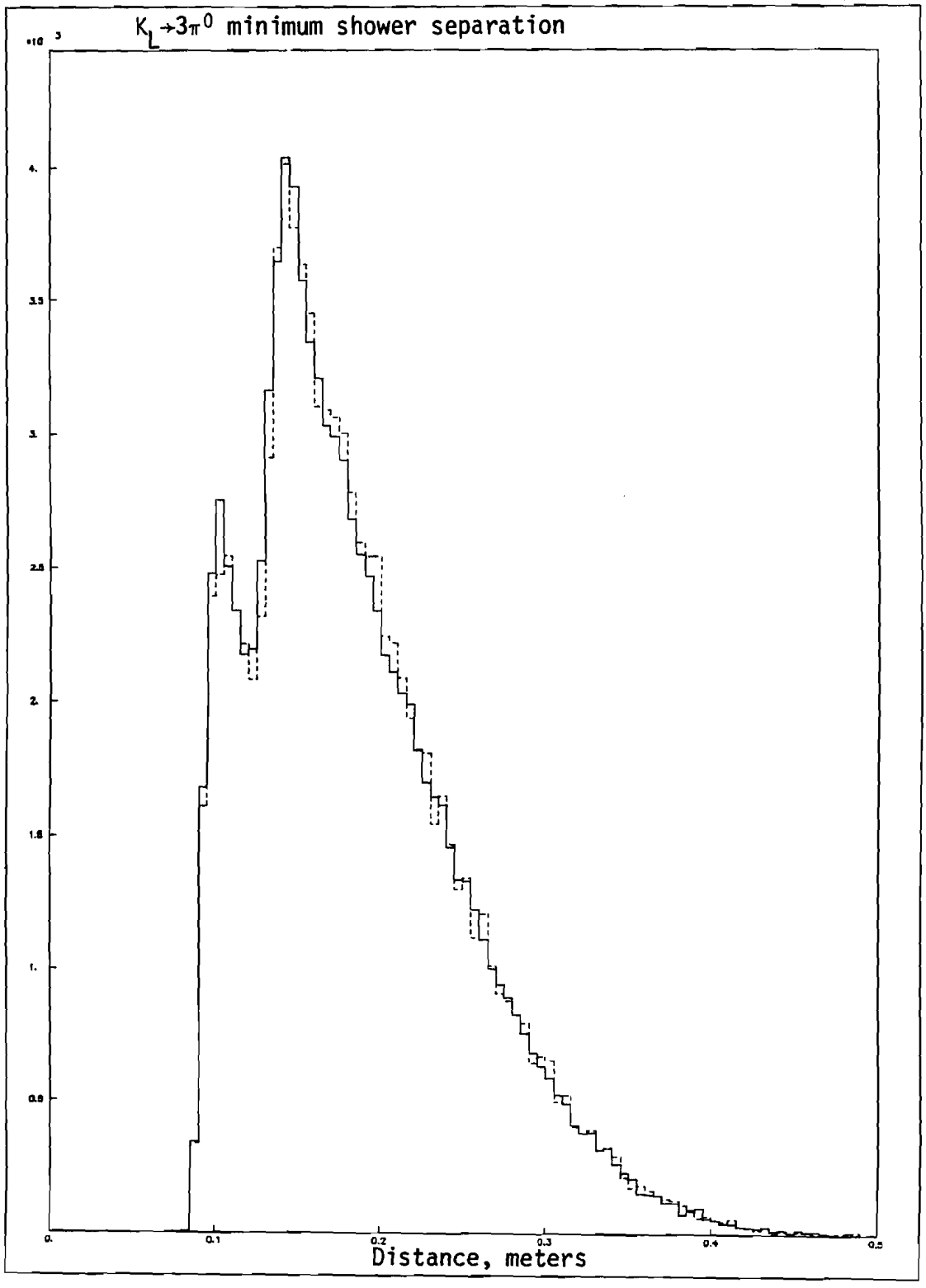
$K_L \to 3\pi^0$ minimum shower separation
Distance, meters

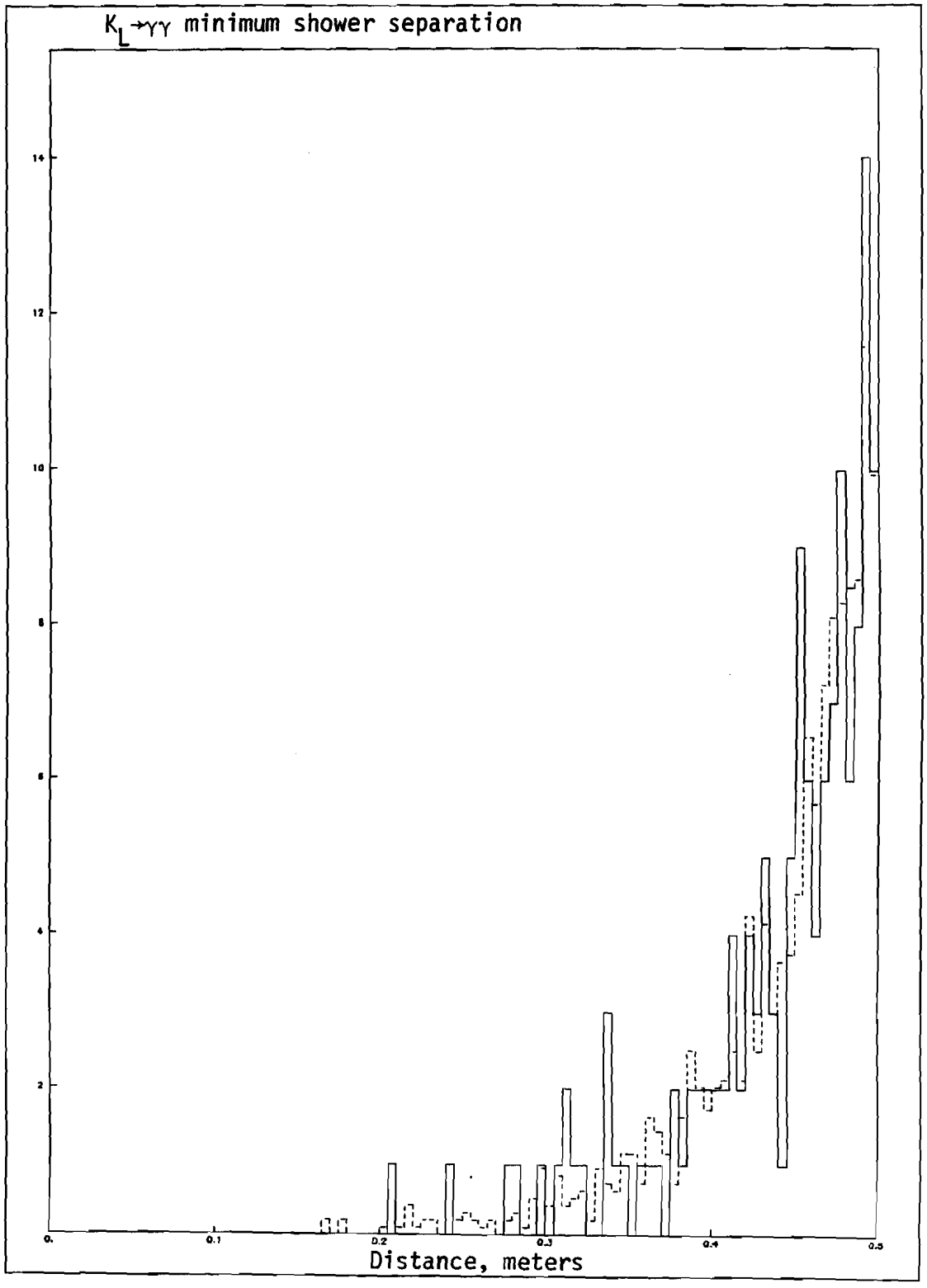
$K_L \to \gamma\gamma$ minimum shower separation
14
12
10
8
6
4
2
0.
0.1
0.2
0.3
0.4
0.5
Distance, meters

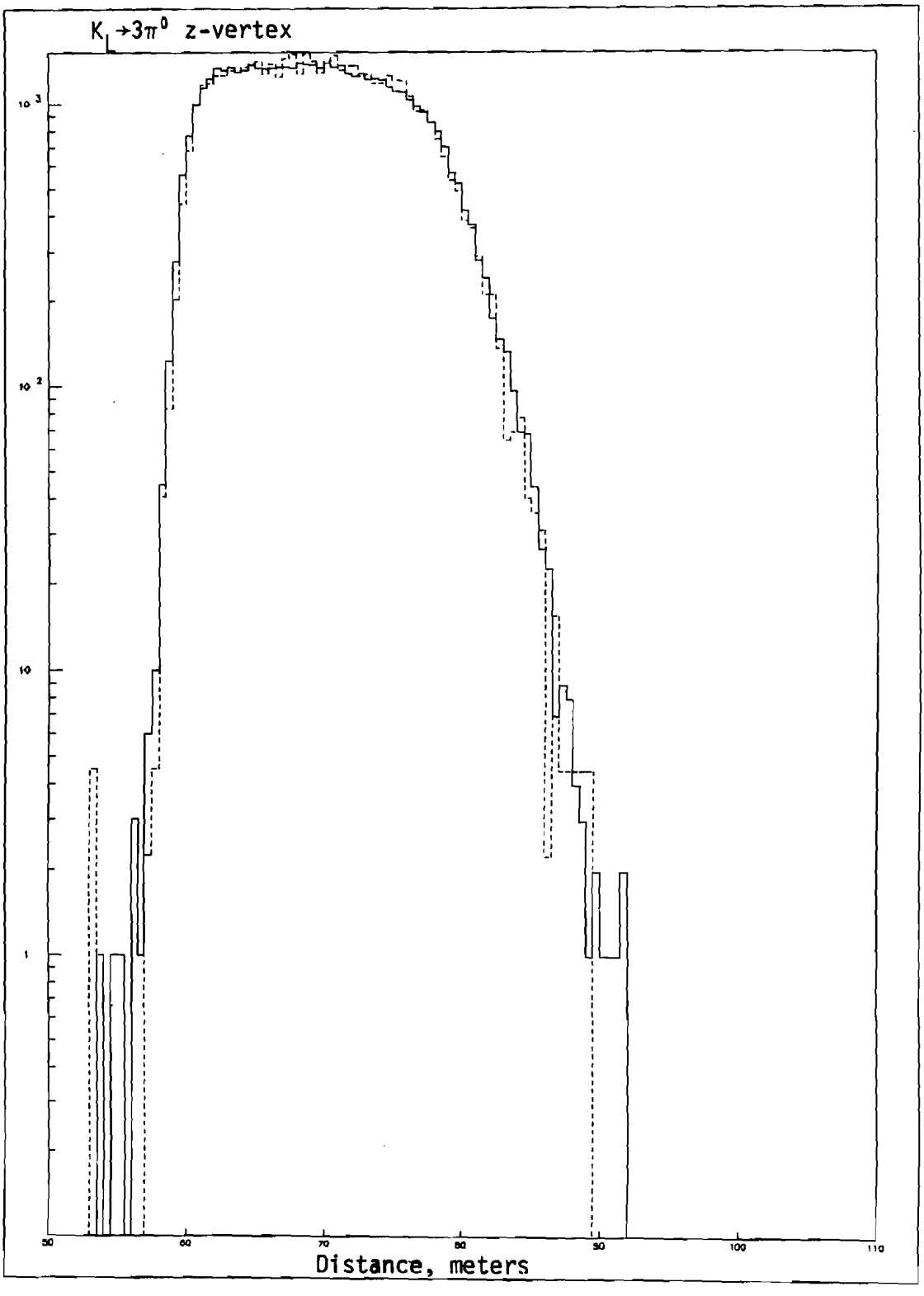
$K_L \rightarrow 3\pi^0$ z-vertex
10^3
10^2
10
1
50
60
70
80
90
100
110
Distance, meters

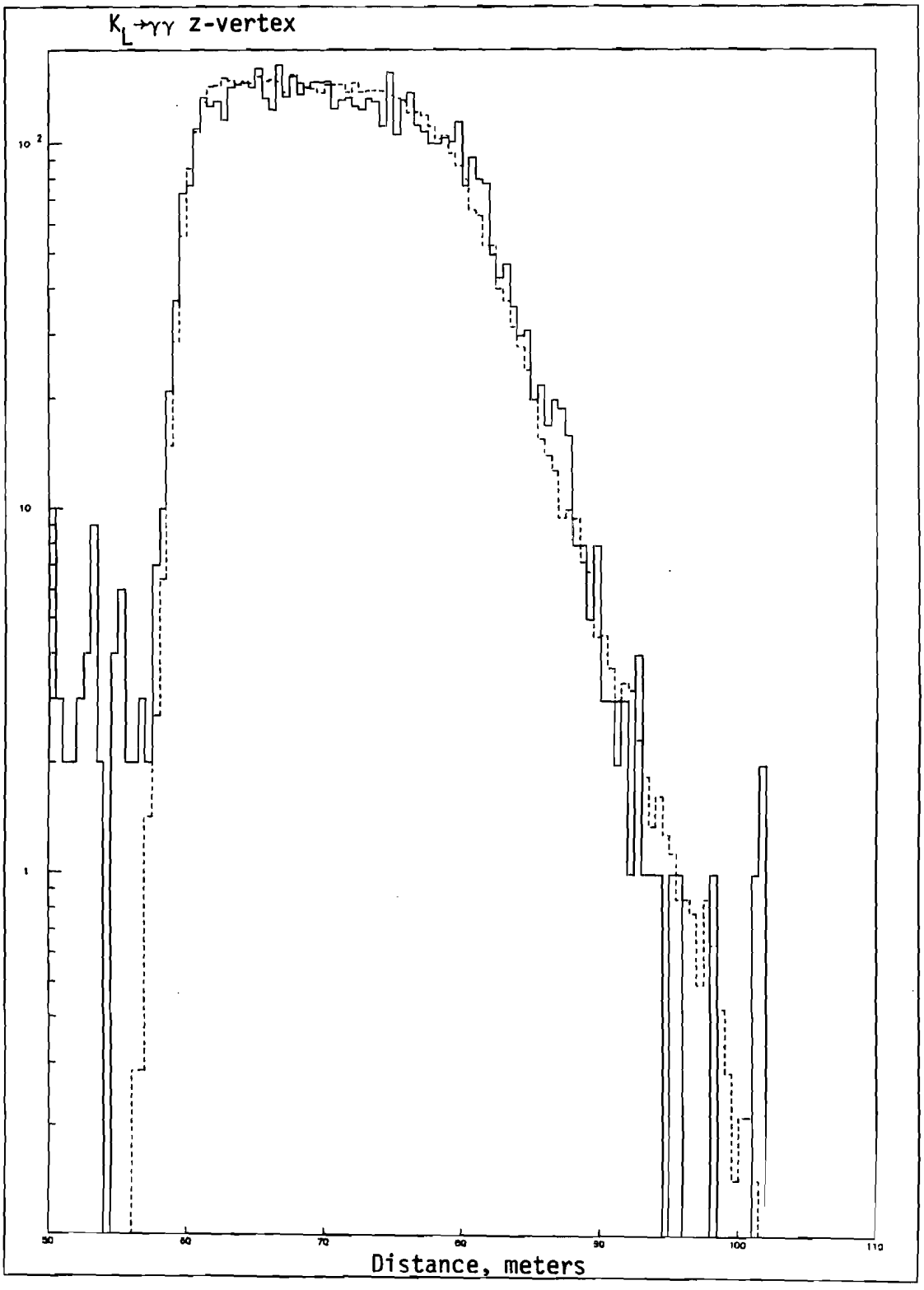
$K_L \to \gamma\gamma$ z-vertex
10^2
10
1
50
60
70
80
90
100
110
Distance, meters

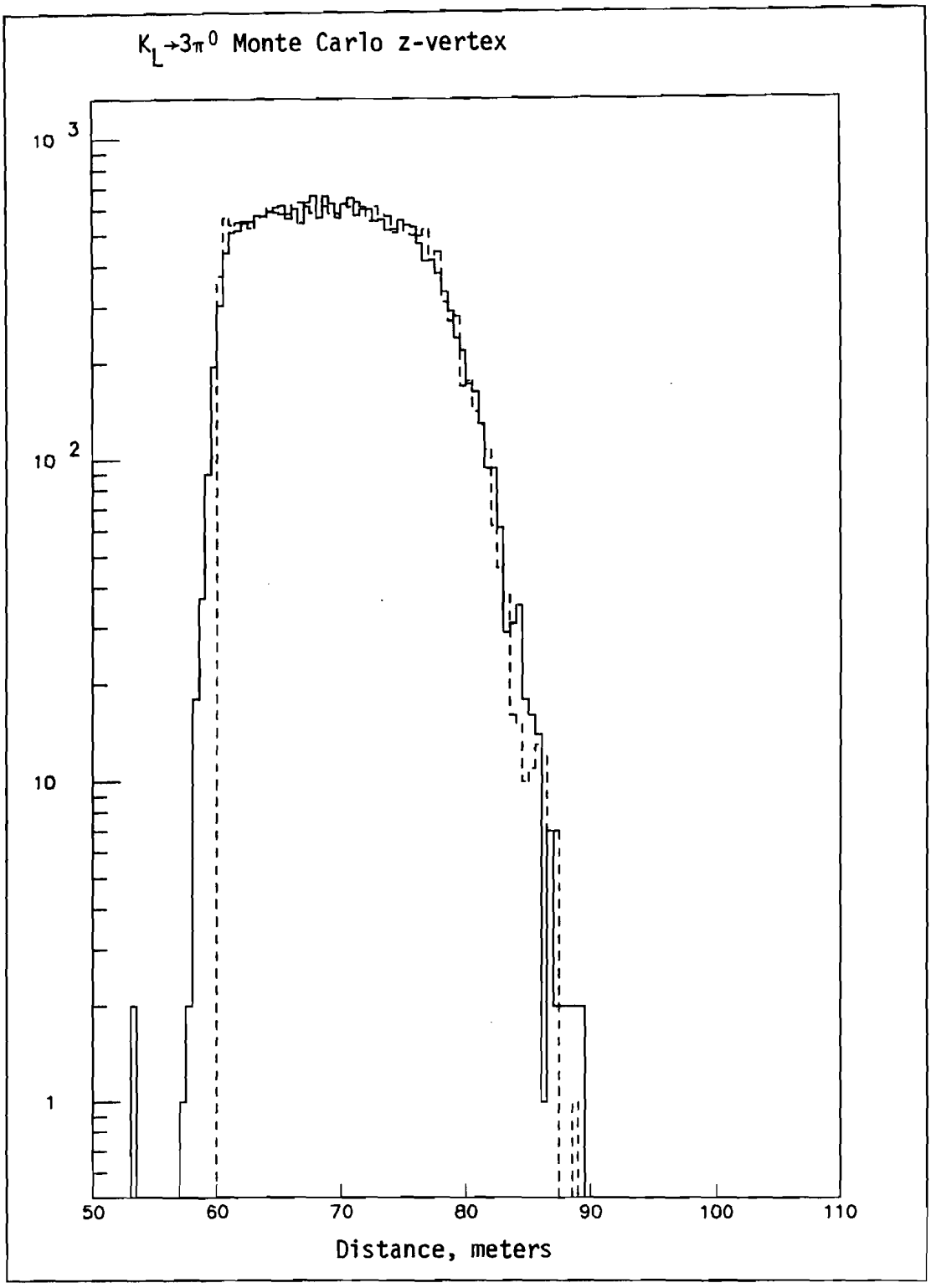
$K_L \rightarrow 3\pi^0$ Monte Carlo z-vertex
10^3
10^2
10
1
50
60
70
80
90
100
110
Distance, meters

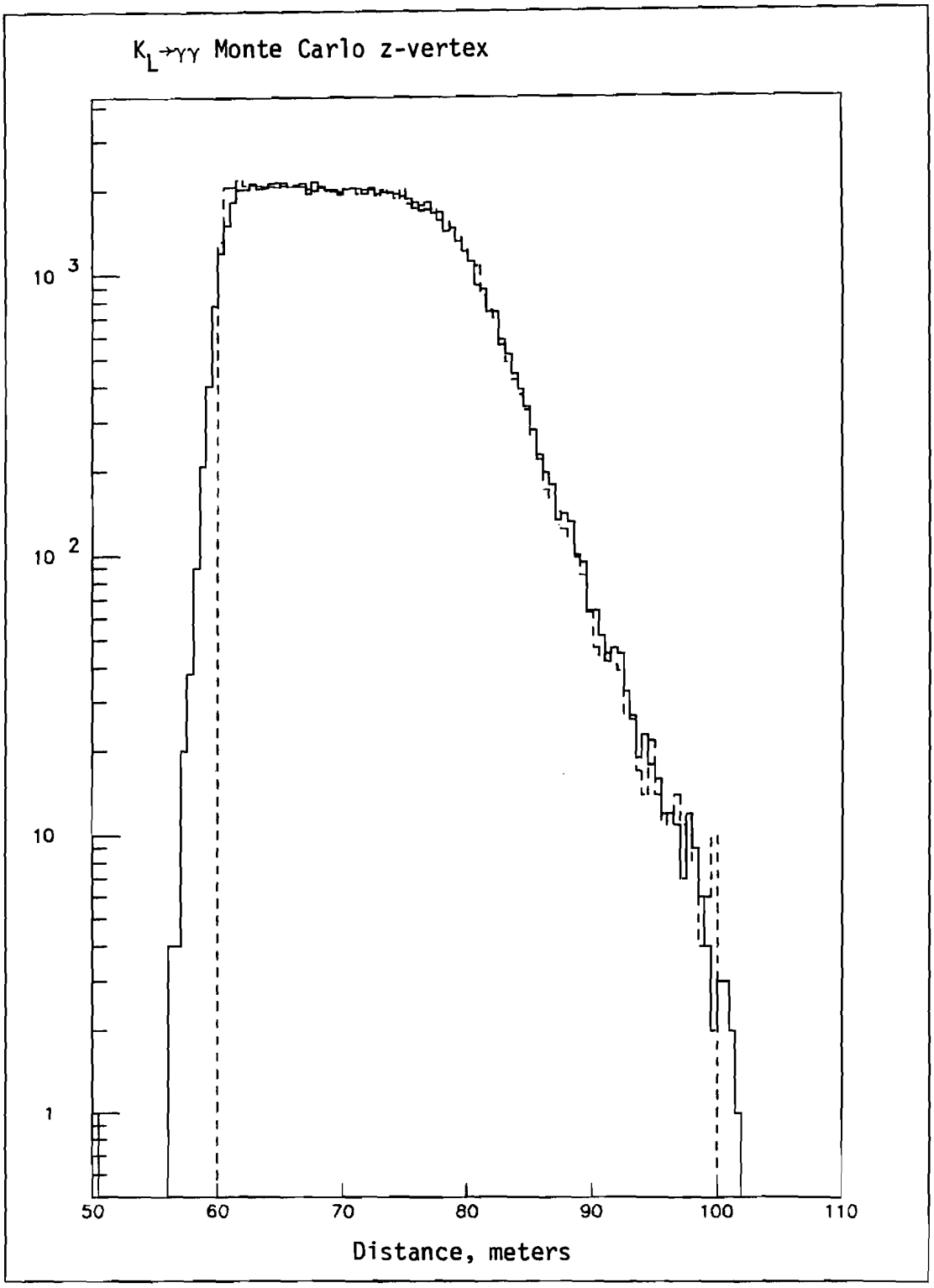
$K_L \to \gamma\gamma$ Monte Carlo z-vertex
10^3
10^2
10
1
50
60
70
80
90
100
110
Distance, meters

CHAPTER IX

CALCULATION OF THE BRANCHING RATIO

This chapter will present the calculation of the number of observed $K_L \to \gamma\gamma$ and $K_L \to 3\pi^\circ$ events, together with their acceptances. As a check on the $K_L \to \gamma\gamma$ branching ratio determined in this fashion, a calculation of the branching ratio of $K_L \to 2\pi^\circ$ also normalized to $K_L \to 3\pi^\circ$ was made, and used to determine the ratio of CP violation parameters

$$\frac{|\eta_{00}|^2}{|\eta_{+-}|^2}.$$

The data were analyzed in four bins of momentum: 80-80 GeV, 80-100 GeV, 100-120 GeV, and 120-140 GeV.

Several cuts were made on the final sample to ensure that the events were quite clean.

Events with a shower above 118 GeV were cut, as it was quite unlikely that a real electromagnetic shower would have this energy and not cause one of the ADC channels to saturate. (Events with a saturated channel had been cut earlier.) The distribution of the highest energy shower in $K_L \to 3\pi^\circ$ and $K_L \to \gamma\gamma$ events is shown in Figures 41 and 42.

Events in which the minimum distance between two gamma ray showers, or between an electron shower and a gamma ray shower was less than 17 cm were cut. This cut discarded

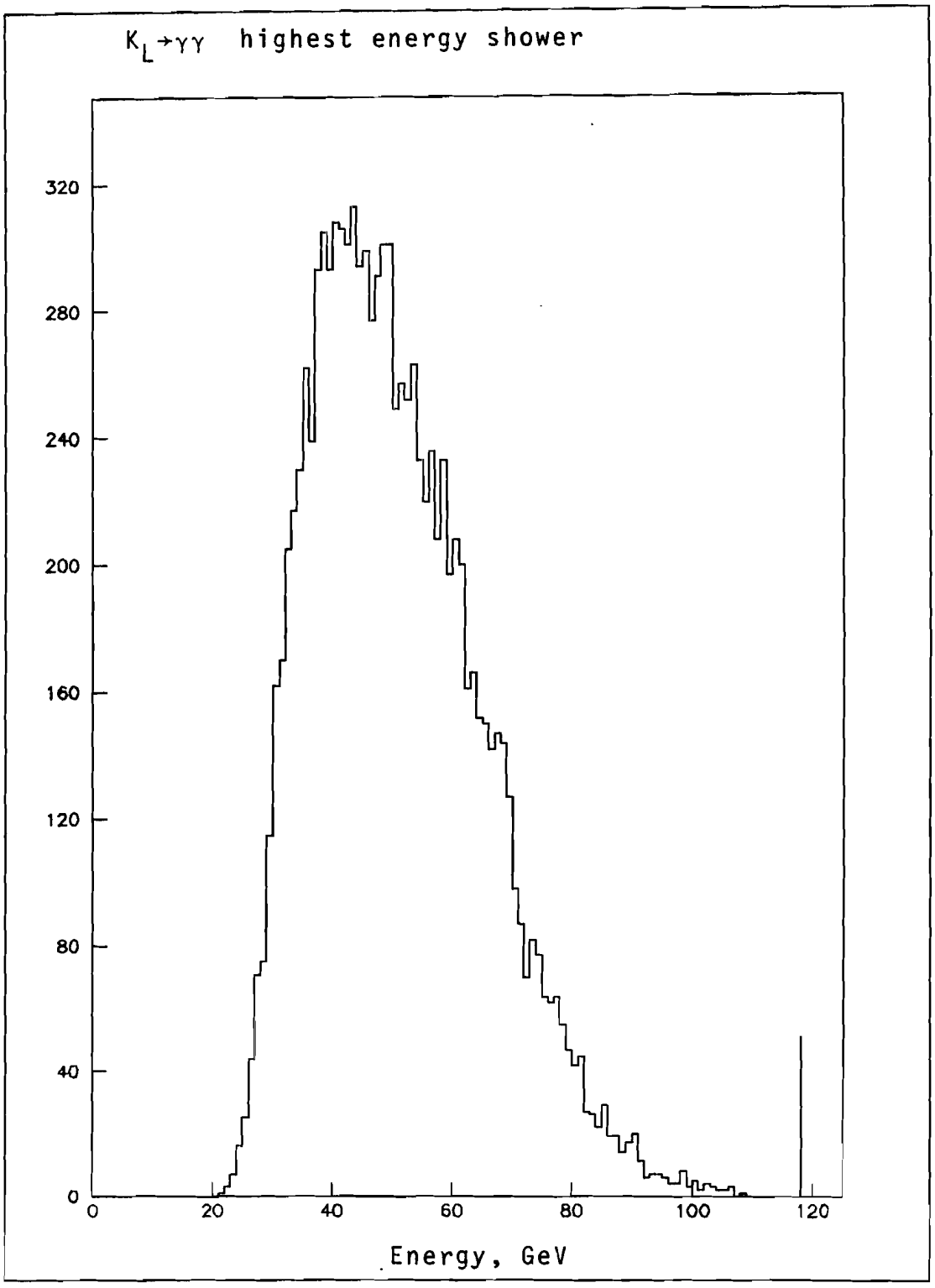
$K_L \to \gamma\gamma$ highest energy shower
320
280
240
200
160
120
80
40
0
0
20
40
60
80
100
120
Energy, GeV

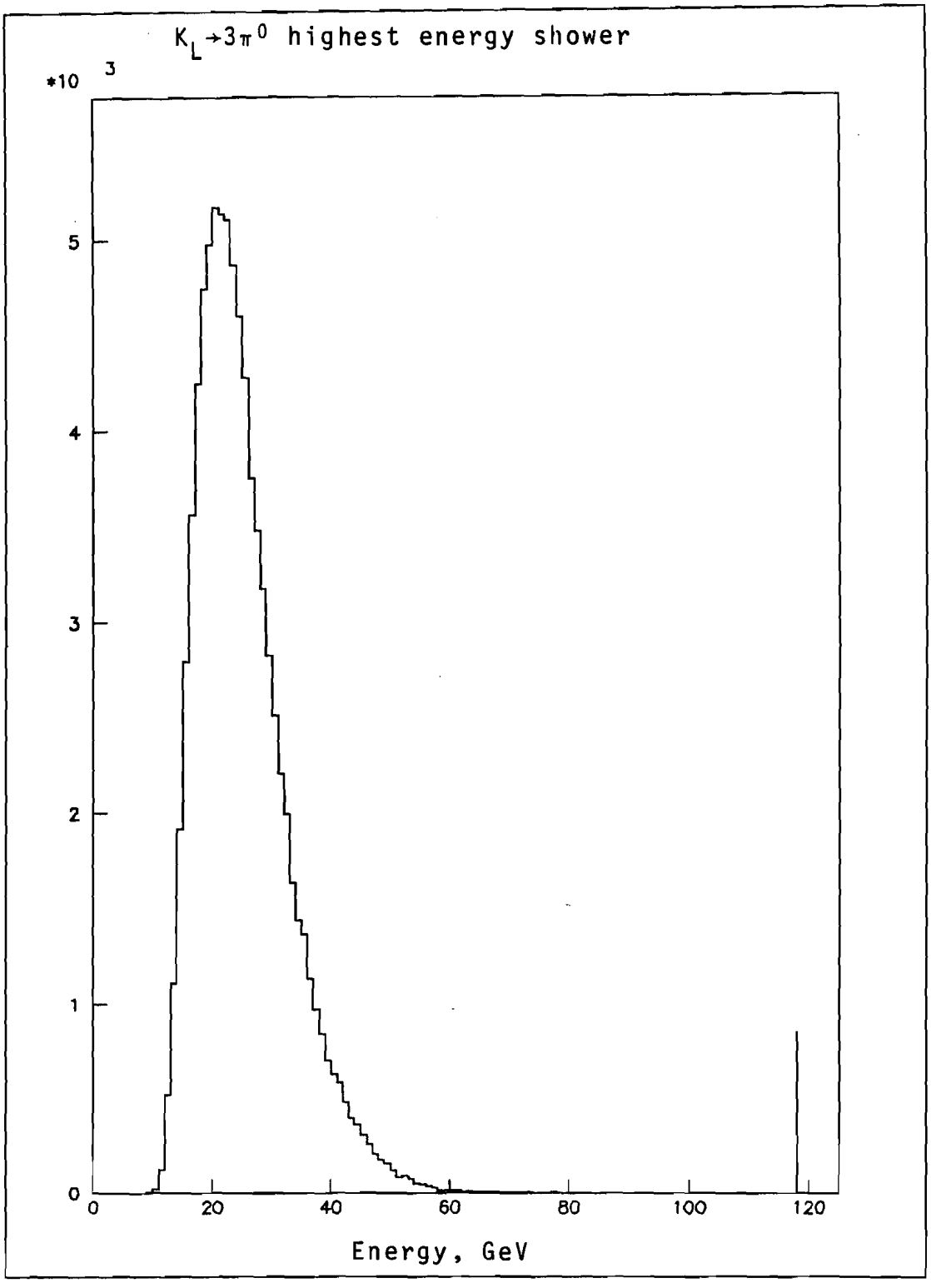
$K_L \to 3\pi^0$ highest energy shower
*10 3
5
4
3
2
1
0
0
20
40
60
80
100
120
Energy, GeV

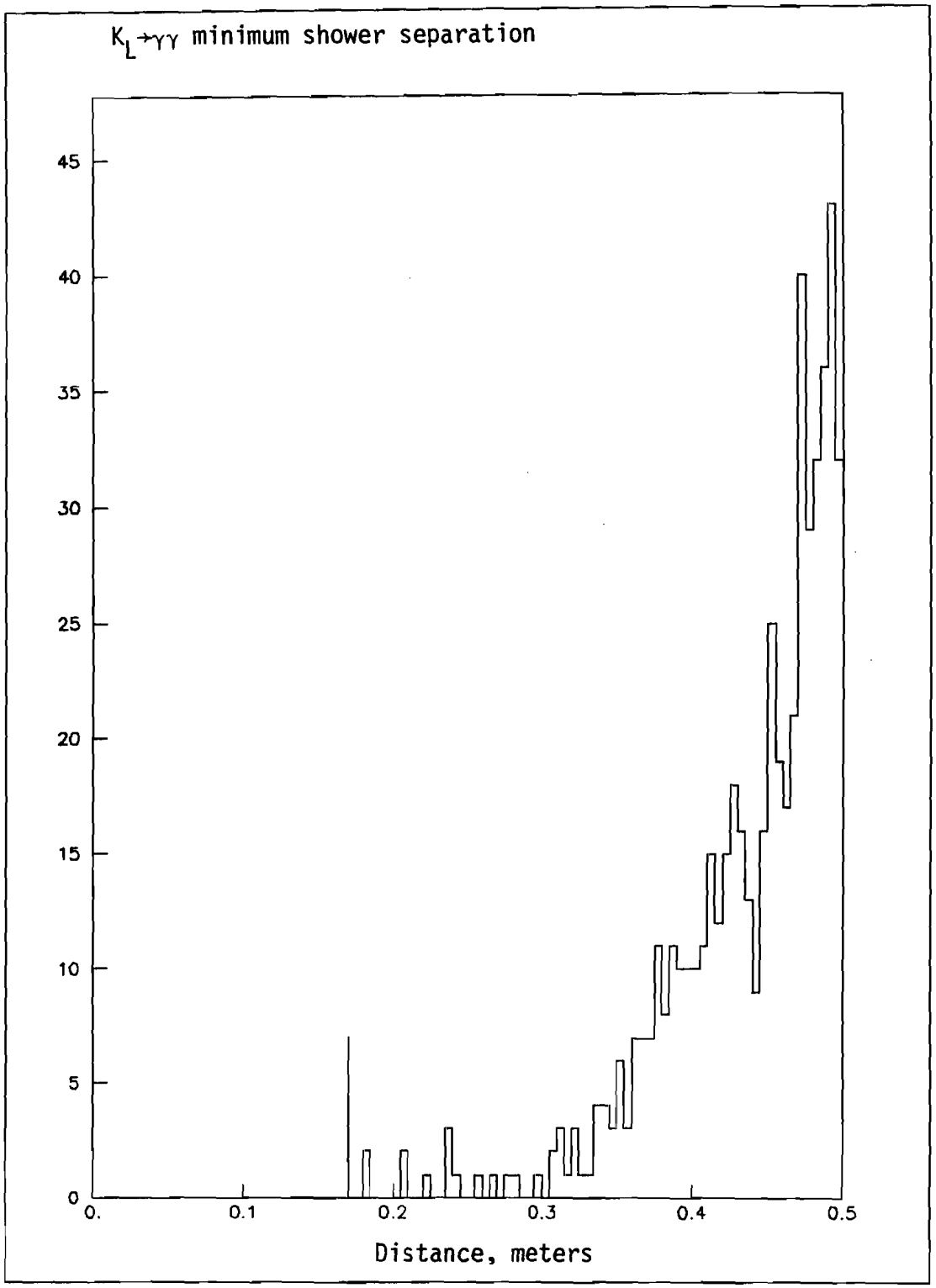
$K_L \to \gamma\gamma$ minimum shower separation
45
40
35
30
25
20
15
10
5
0
0.
0.1
0.2
0.3
0.4
0.5
Distance, meters

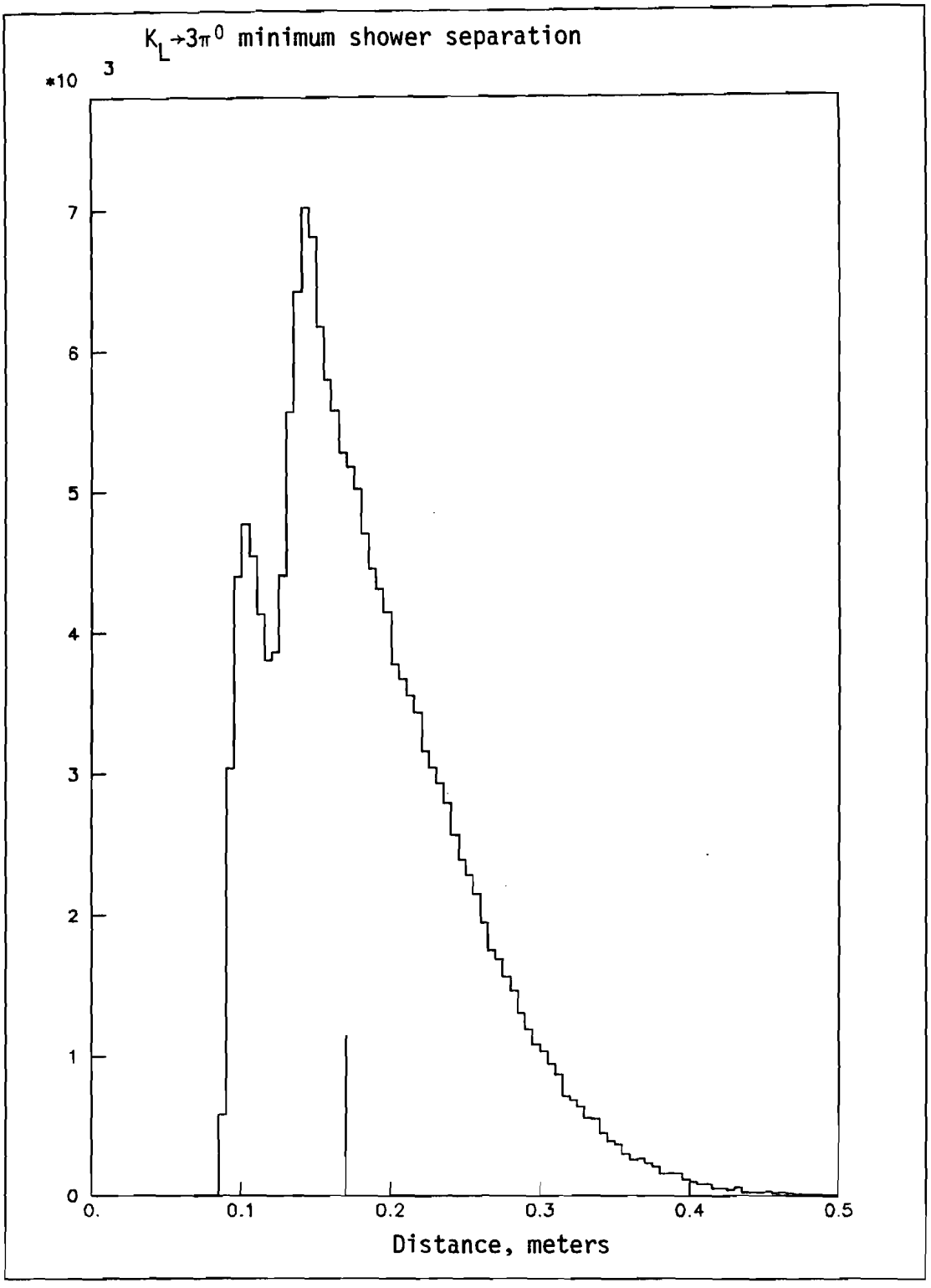
$K_L \to 3\pi^0$ minimum shower separation
*10 3
7
6
5
4
3
2
1
0
0.
0.1
0.2
0.3
0.4
0.5
Distance, meters

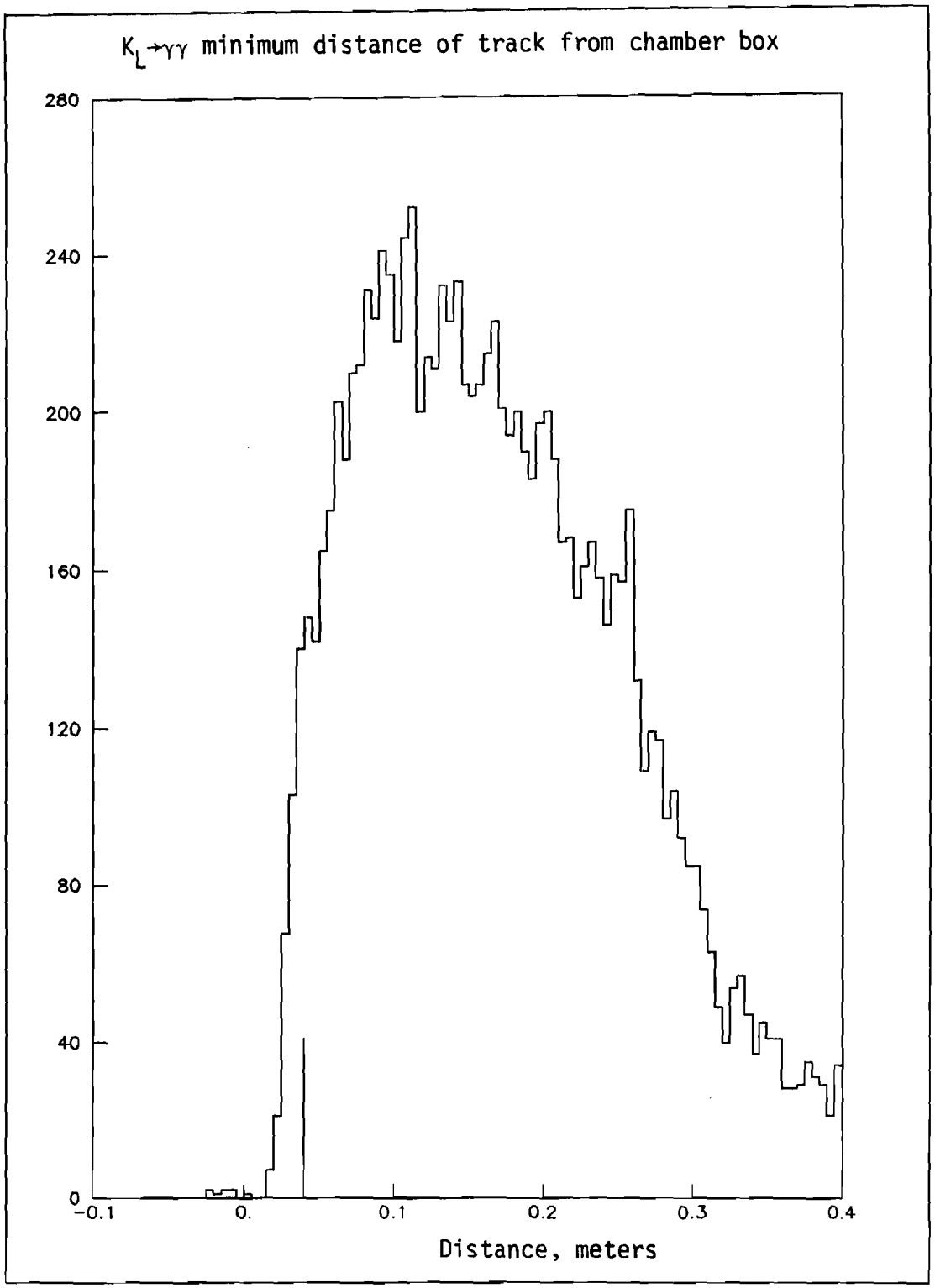
$K_L \to \gamma\gamma$ minimum distance of track from chamber box
280
240
200
160
120
80
40
0
−0.1
0.
0.1
0.2
0.3
0.4
Distance, meters

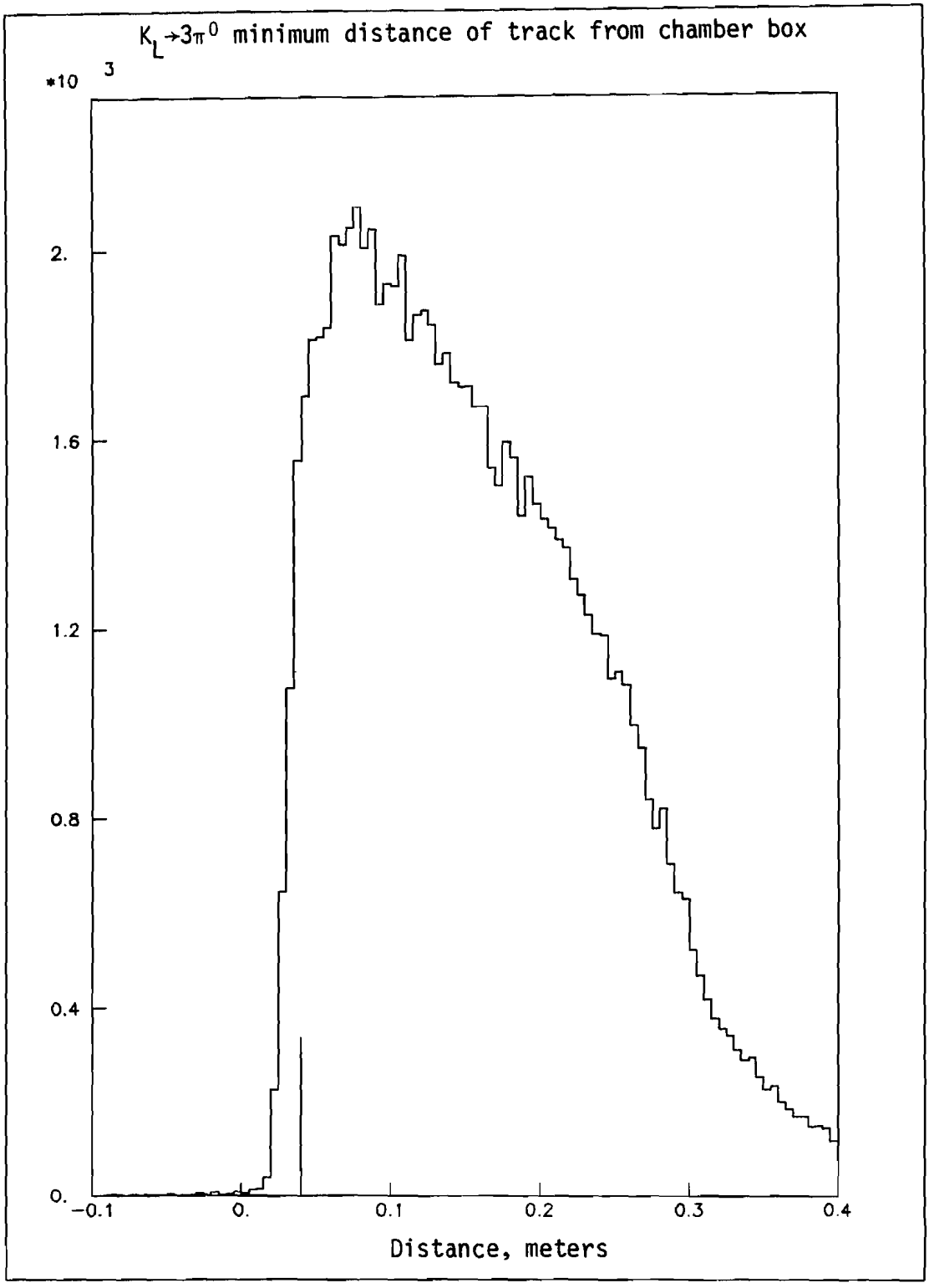
$K_L \to 3\pi^0$ minimum distance of track from chamber box
*10 3
2.
1.6
1.2
0.8
0.4
0.
−0.1
0.
0.1
0.2
0.3
0.4
Distance, meters

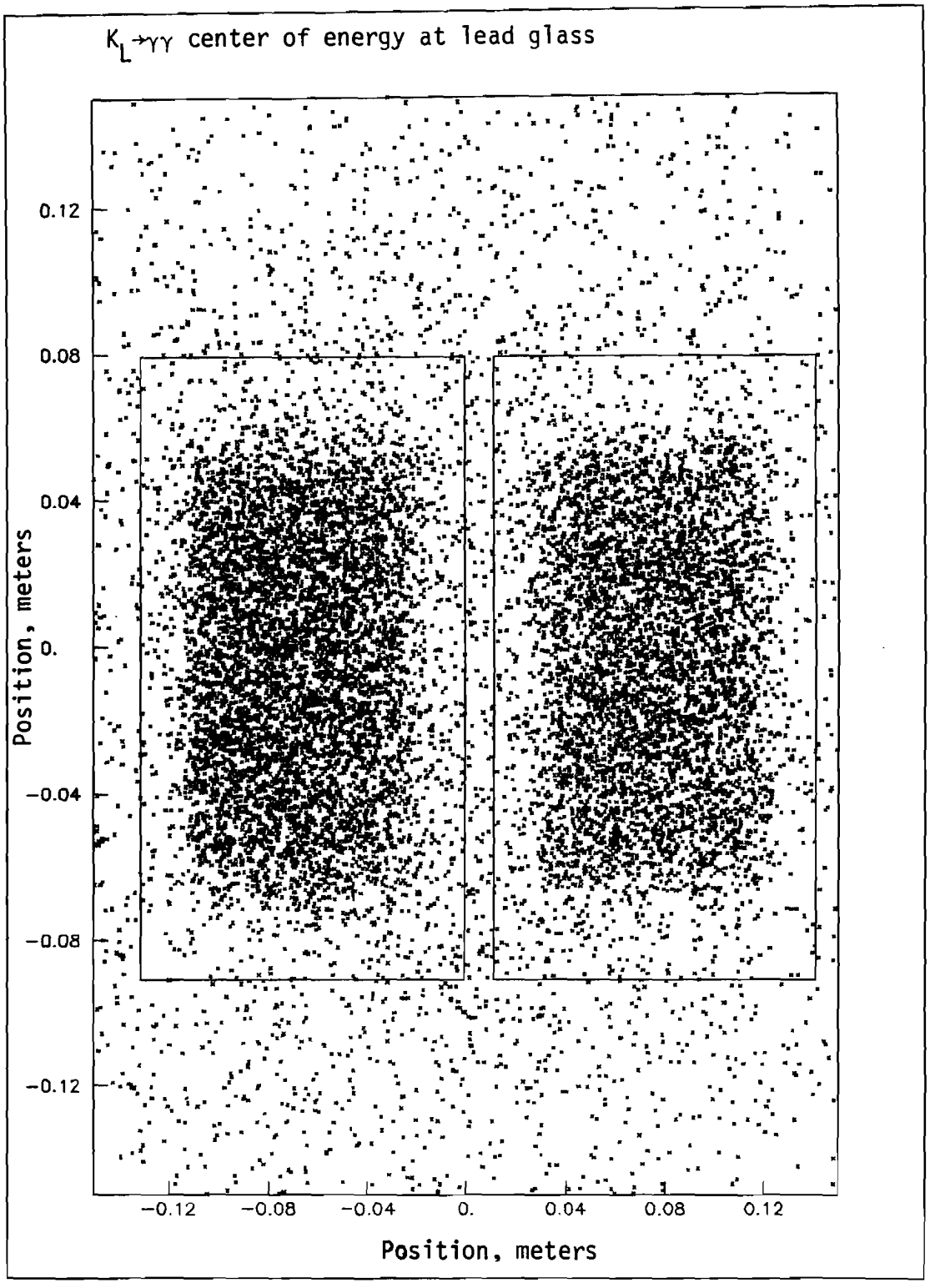
$K_L \to \gamma\gamma$ center of energy at lead glass
0.12
0.08
0.04
0.
−0.04
−0.08
−0.12
Position, meters
−0.12
−0.08
−0.04
0.
0.04
0.08
0.12
Position, meters

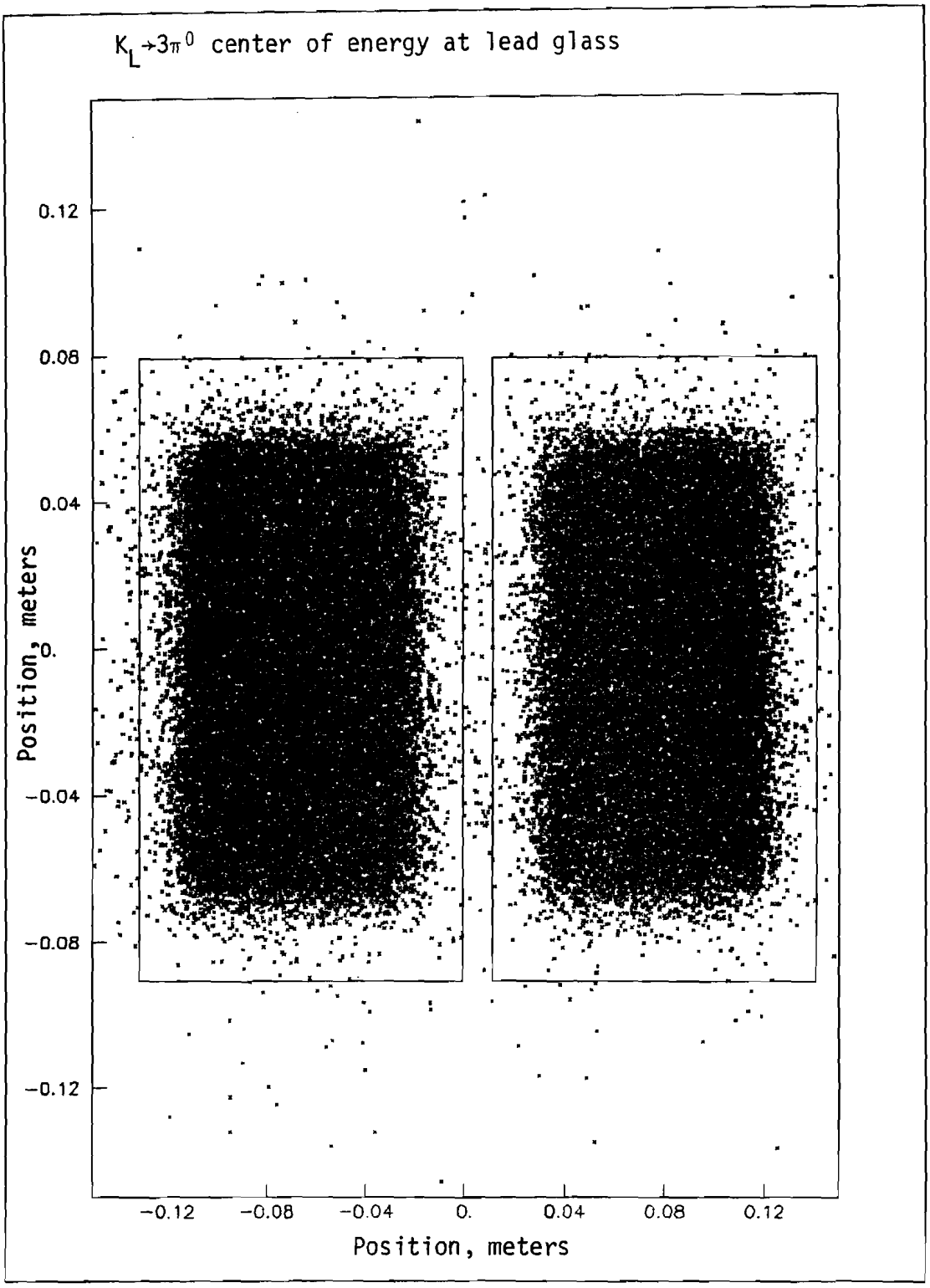
$K_L \to 3\pi^0$ center of energy at lead glass
0.12
0.08
0.04
0.
−0.04
−0.08
−0.12
Position, meters
−0.12
−0.08
−0.04
0.
0.04
0.08
0.12
Position, meters

large were cut. This distance was calculated as a check on the vertex reconstruction described earlier. (Recall that the vertex was assigned to the midpoint of the unique line segment perpendicular to both the converted gamma ray track and the kaon trajectory.) If the distance of closest approach was greater than 3 cm the event was likely to have had many of the same problems as an event with a bad center of energy. The distribution of distance of closest approach tegether with the cut is shown for $K_L \to \gamma\gamma$ and $K_L \to 3\pi^\circ$ events in Figures 49 and 50.

No further cuts were applied to $K_L \to \gamma\gamma$ events, although one more was applied to $K_L \to 3\pi^\circ$ events. The chi-squared quantity defined earlier was required to be less than 15 (for three degrees of freedom). This cut removed events in which a relatively high energy accidental shower fused with a shower in the event. The occurrence was much more likely to cause a $K_L \to \gamma\gamma$ event to be vetoed than a $K_L \to 3\pi^\circ$ without this cut. The chi-squared distribution is shown in Figure 51, with the cut superimposed.

Mass plots for $K_L \to 3\pi^\circ$ events with all these cuts applied are shown in Figures 52 through 55. The mass resolution we achieved was roughly 15 MeV/c^2. The width of the mass peak was due primarily to our vertex resolution of about 2 meters, or $\sim$3% of the distance between the decay

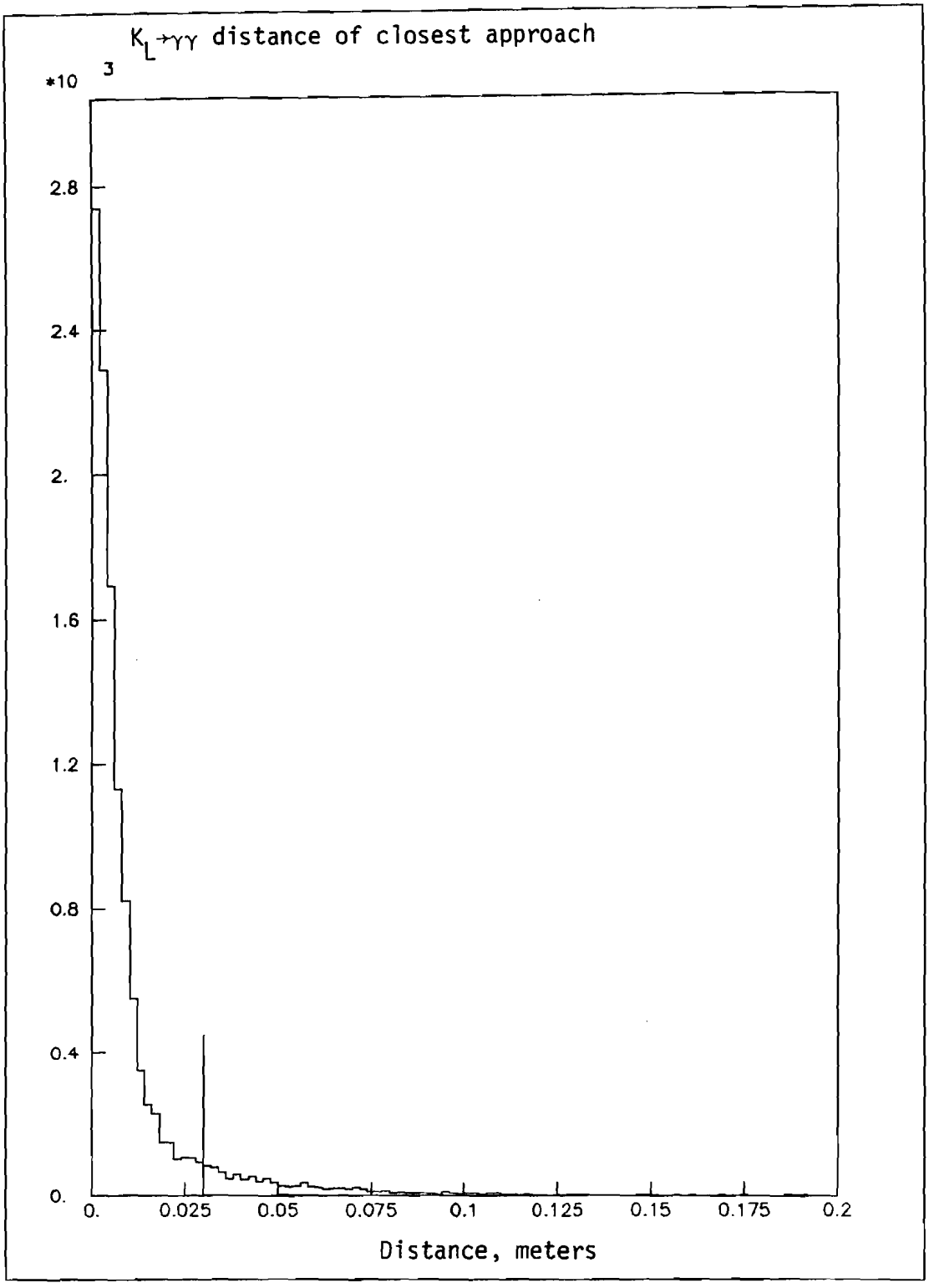
$K_L \to \gamma\gamma$ distance of closest approach
*10 3
2.8
2.4
2.
1.6
1.2
0.8
0.4
0.
0.
0.025
0.05
0.075
0.1
0.125
0.15
0.175
0.2
Distance, meters

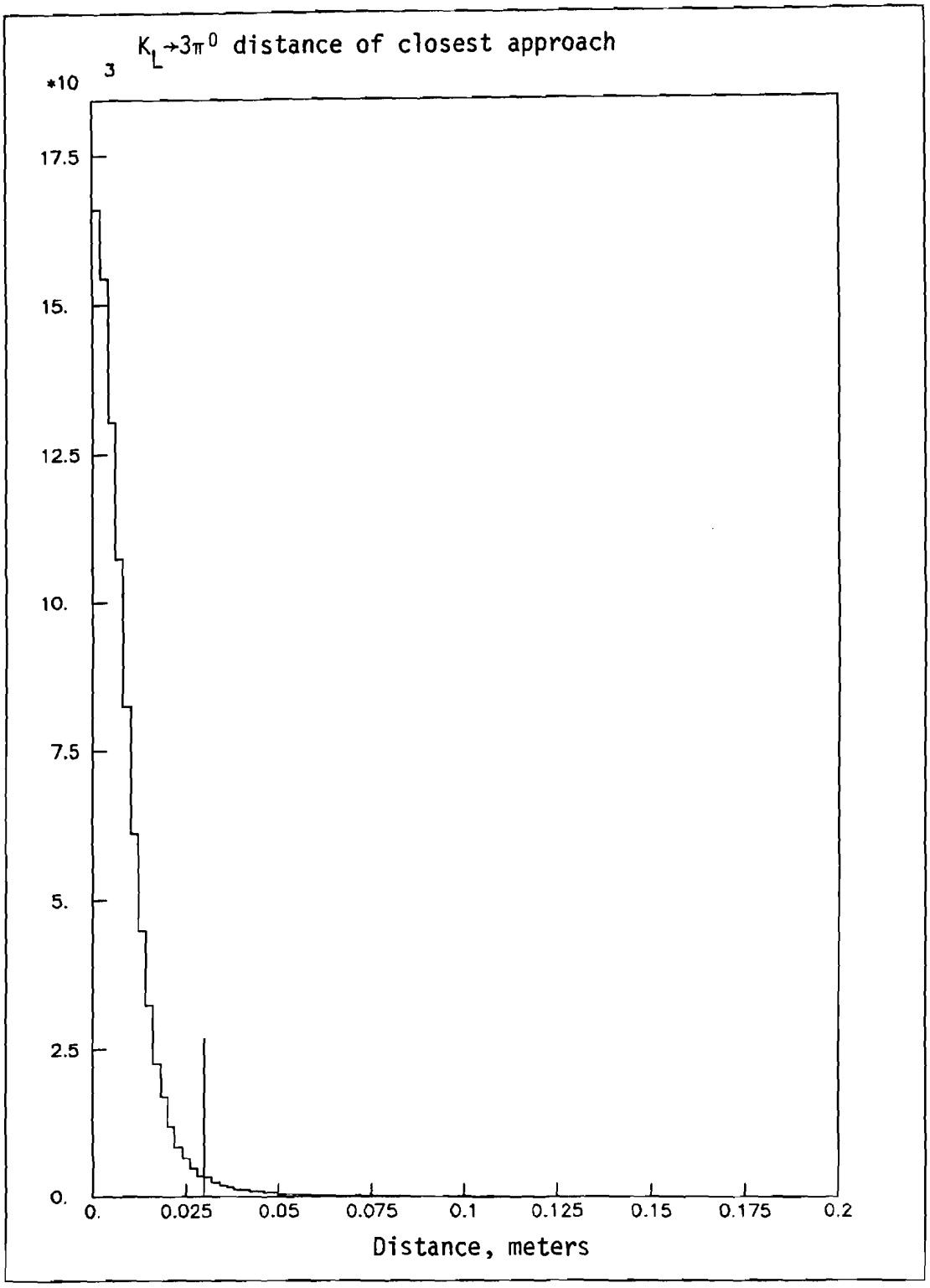
$K_L \to 3\pi^0$ distance of closest approach
*10 3
17.5
15.
12.5
10.
7.5
5.
2.5
0.
0.
0.025
0.05
0.075
0.1
0.125
0.15
0.175
0.2
Distance, meters

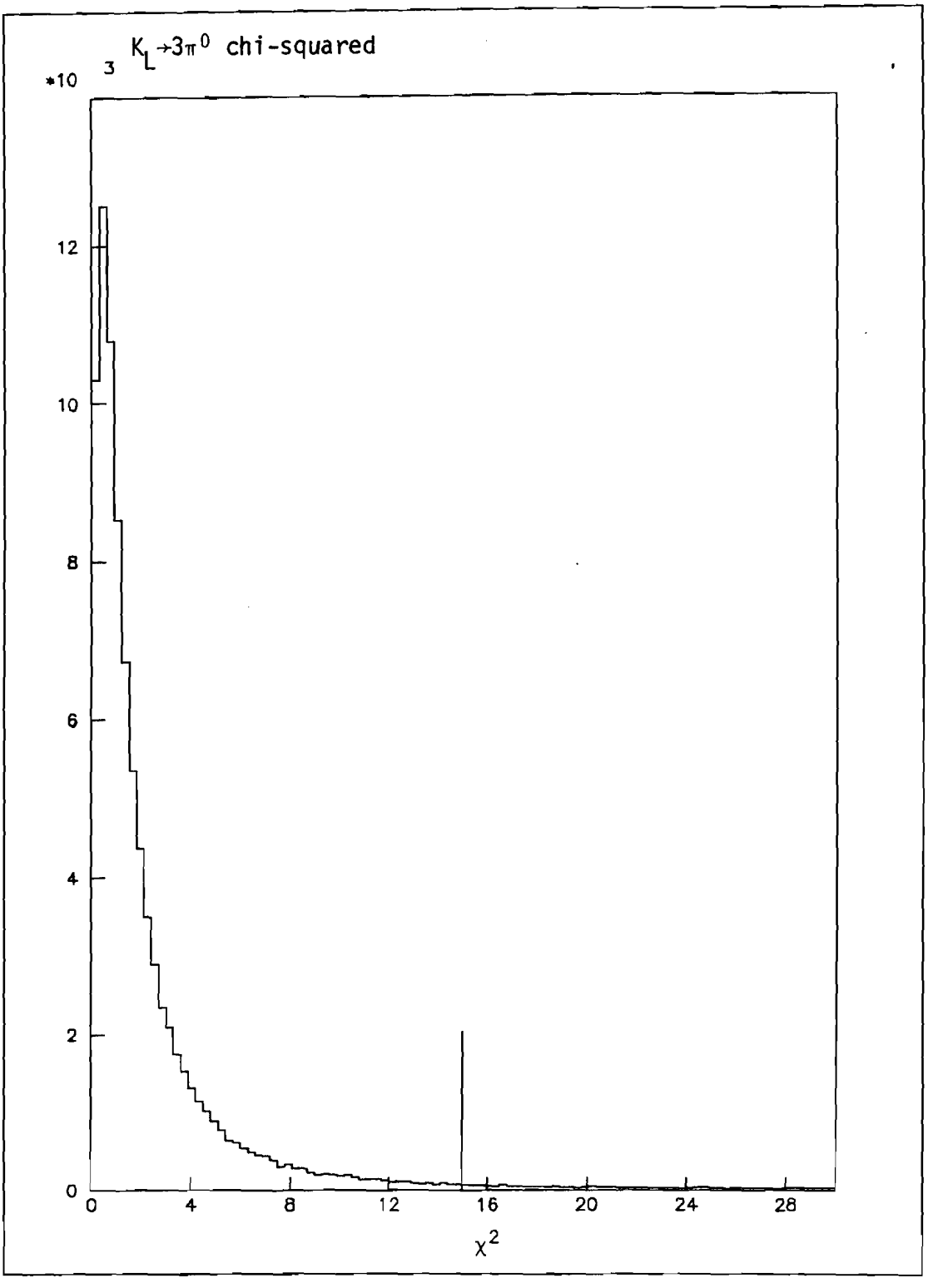
$K_L \to 3\pi^0$ chi-squared
*10 3
12
10
8
6
4
2
0
0
4
8
12
16
20
24
28
χ^2

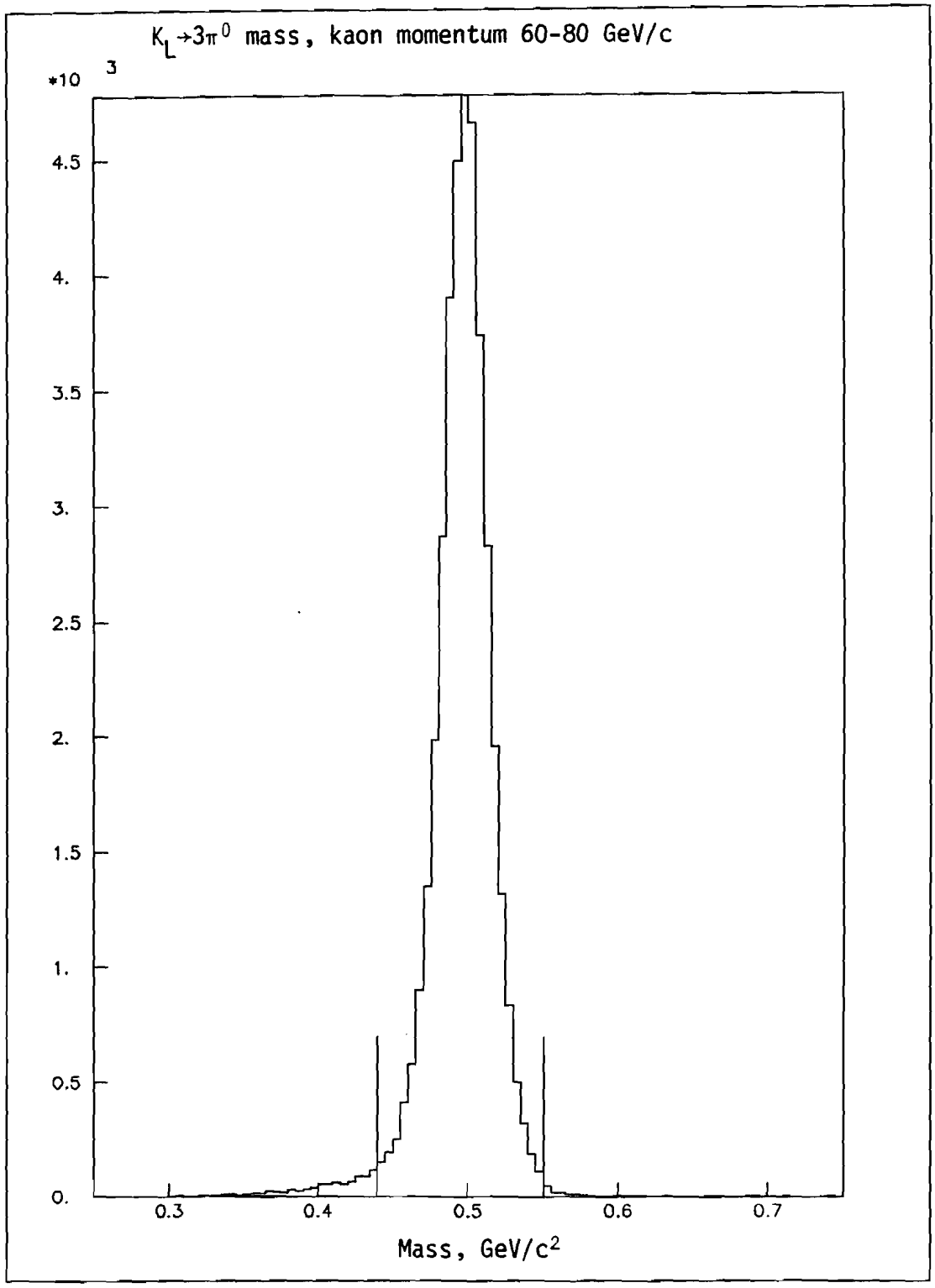
$K_L \to 3\pi^0$ mass, kaon momentum 60-80 GeV/c
*10 3
4.5
4.
3.5
3.
2.5
2.
1.5
1.
0.5
0.
0.3
0.4
0.5
0.6
0.7
Mass, GeV/c^2

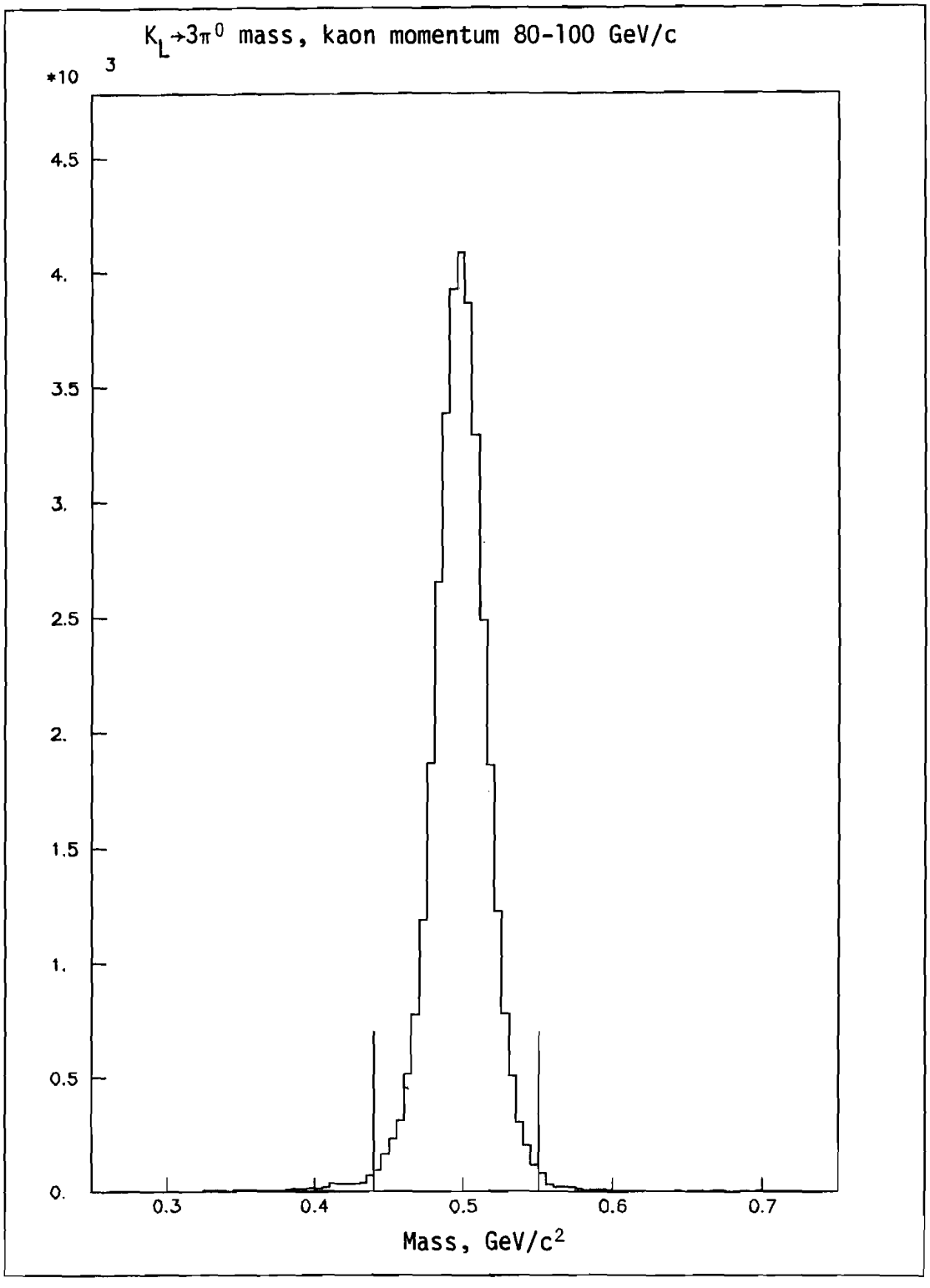
$K_L \to 3\pi^0$ mass, kaon momentum 80-100 GeV/c
*10 3
4.5
4.
3.5
3.
2.5
2.
1.5
1.
0.5
0.
0.3
0.4
0.5
0.6
0.7
Mass, GeV/c^2

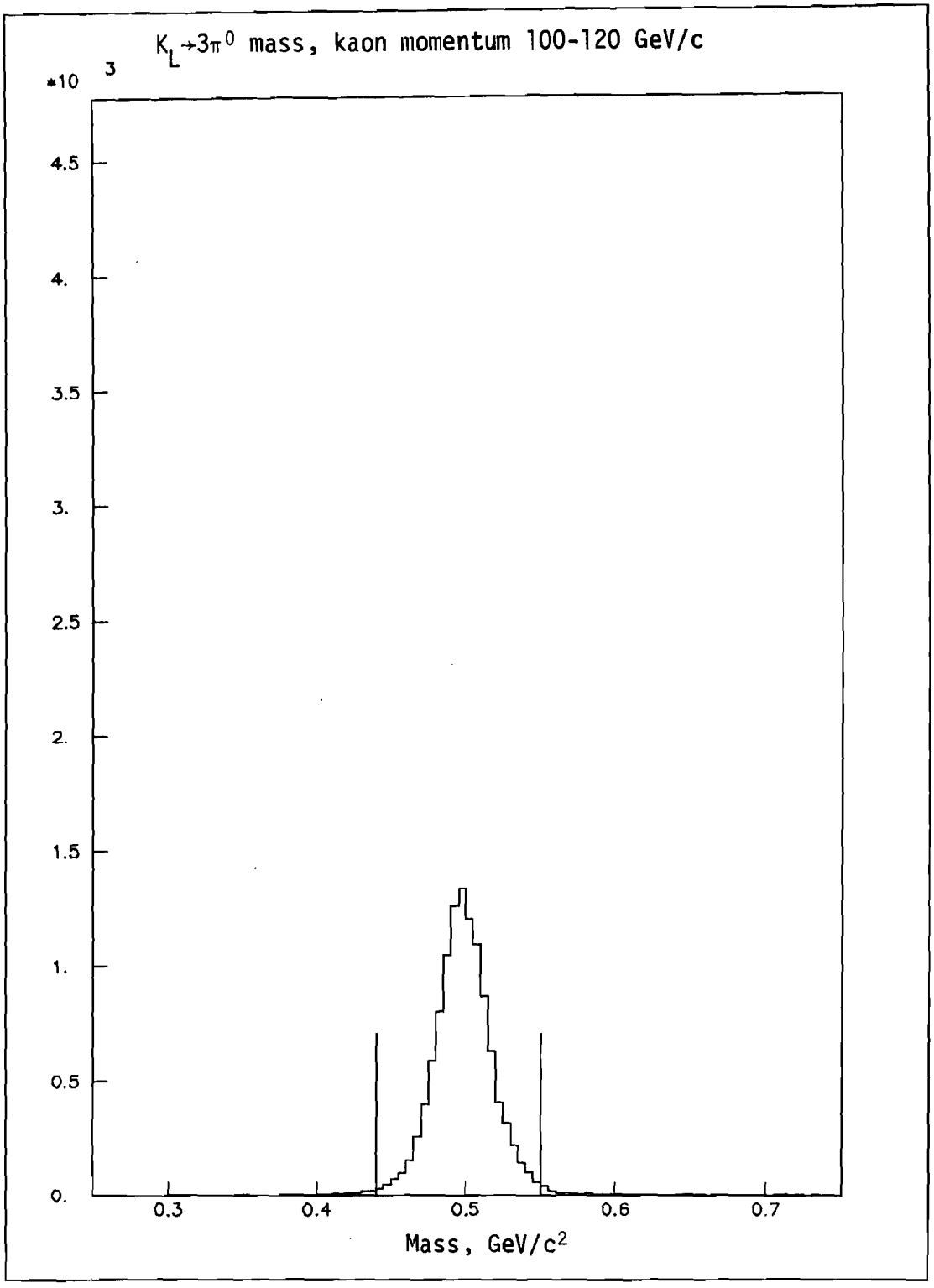
$K_L \to 3\pi^0$ mass, kaon momentum 100-120 GeV/c
*10 3
4.5
4.
3.5
3.
2.5
2.
1.5
1.
0.5
0.
0.3
0.4
0.5
0.6
0.7
Mass, GeV/c^2

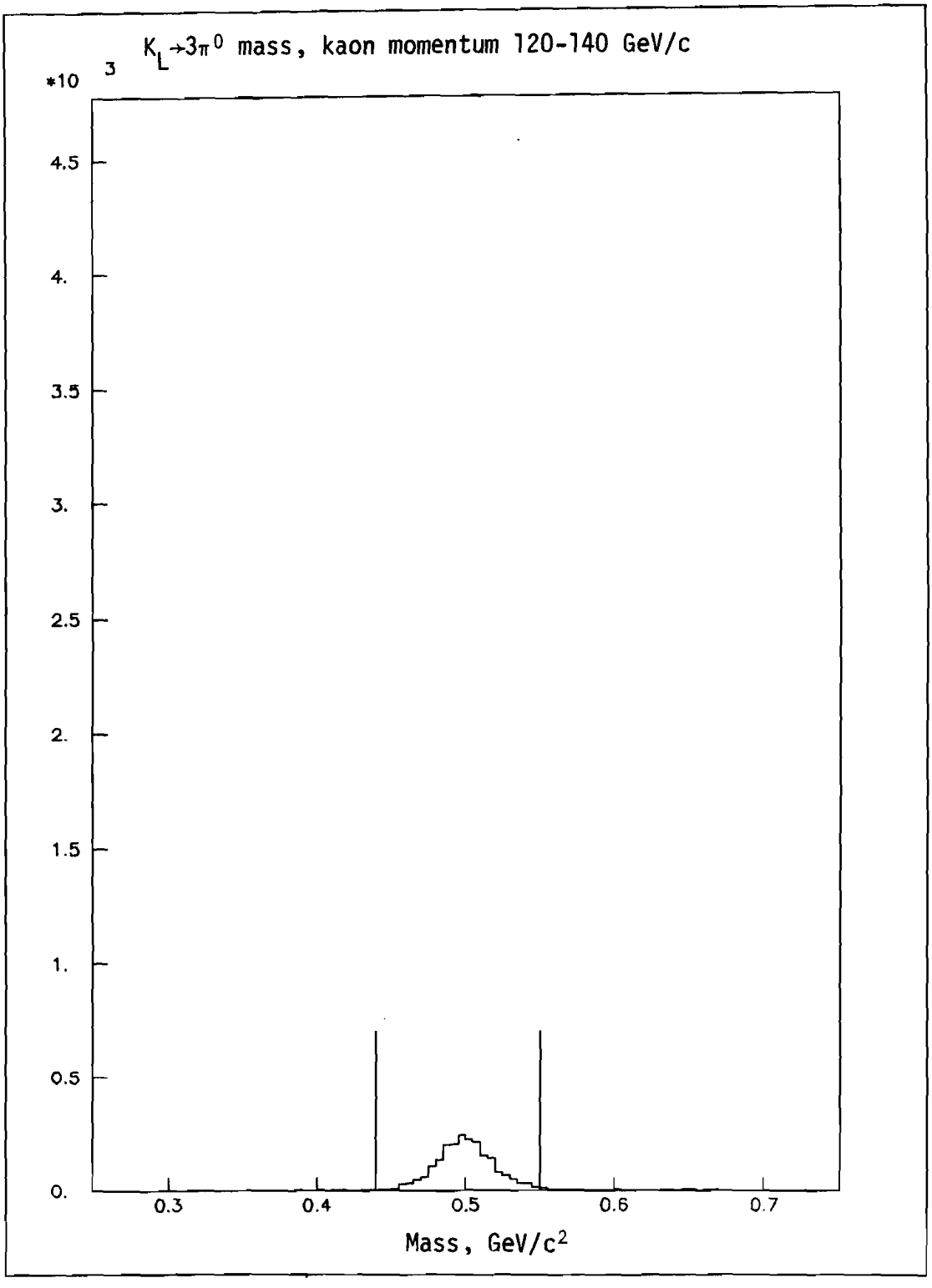
$K_L \to 3\pi^0$ mass, kaon momentum 120-140 GeV/c
*10 3
4.5
4.
3.5
3.
2.5
2.
1.5
1.
0.5
0.
0.3
0.4
0.5
0.6
0.7
Mass, GeV/c^2

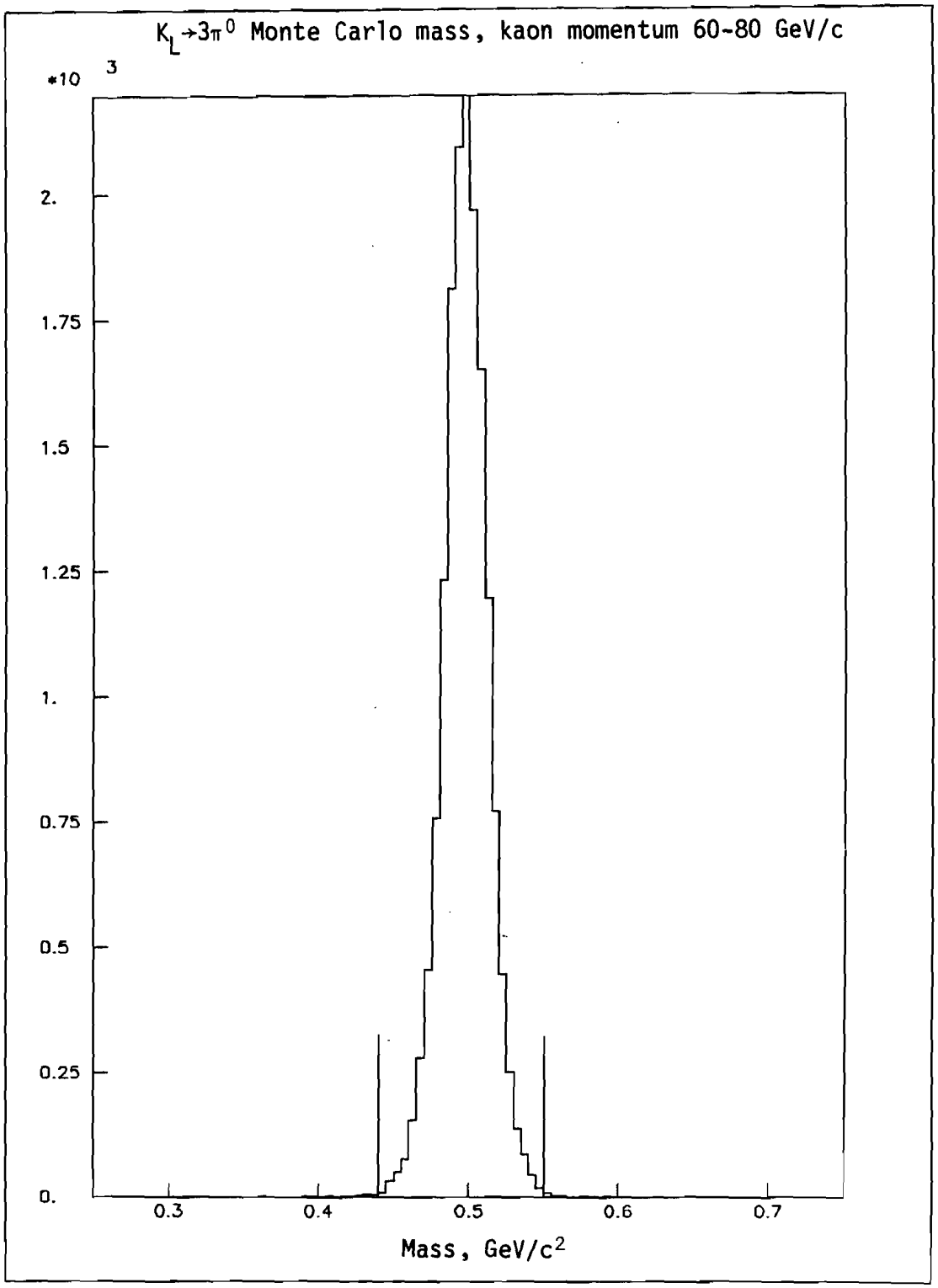
$K_L \to 3\pi^0$ Monte Carlo mass, kaon momentum 60-80 GeV/c
*10 3
2.
1.75
1.5
1.25
1.
0.75
0.5
0.25
0.
0.3
0.4
0.5
0.6
0.7
Mass, GeV/c^2

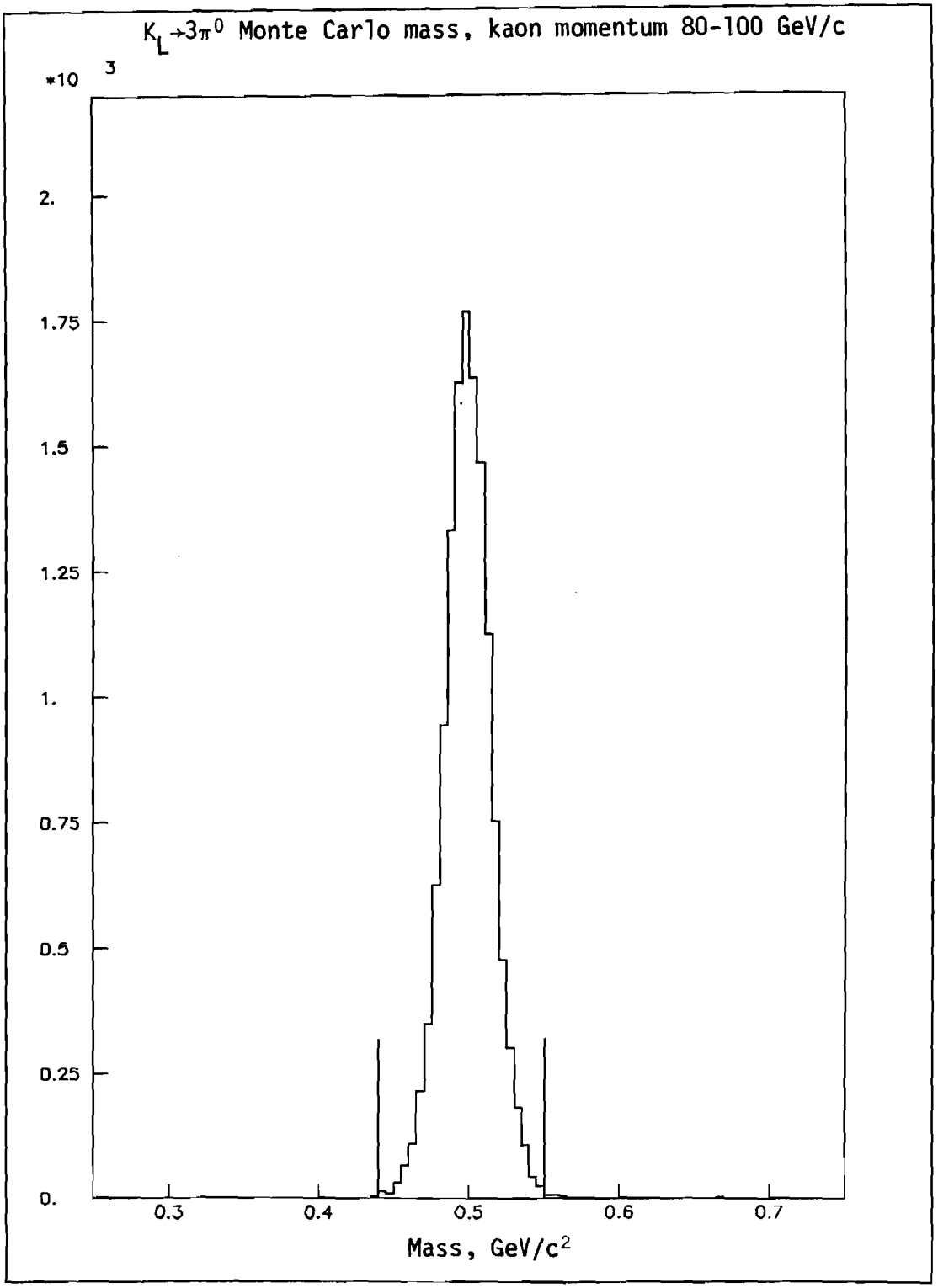
$K_L \to 3\pi^0$ Monte Carlo mass, kaon momentum 80-100 GeV/c
*10 3
2.
1.75
1.5
1.25
1.
0.75
0.5
0.25
0.
0.3
0.4
0.5
0.6
0.7
Mass, GeV/c^2

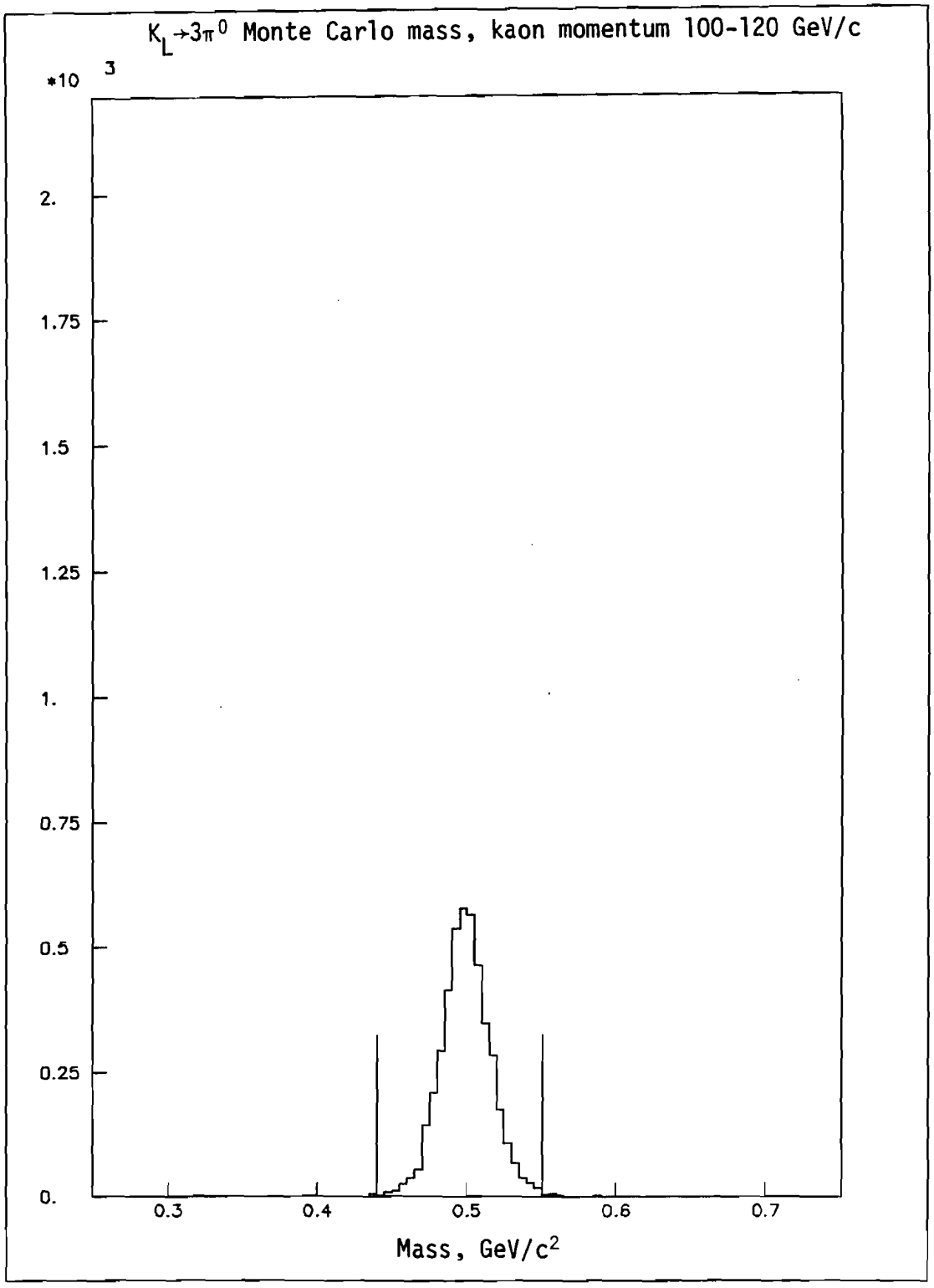
$K_L \to 3\pi^0$ Monte Carlo mass, kaon momentum 100-120 GeV/c
*10 3
2.
1.75
1.5
1.25
1.
0.75
0.5
0.25
0.
0.3
0.4
0.5
0.6
0.7
Mass, GeV/c^2

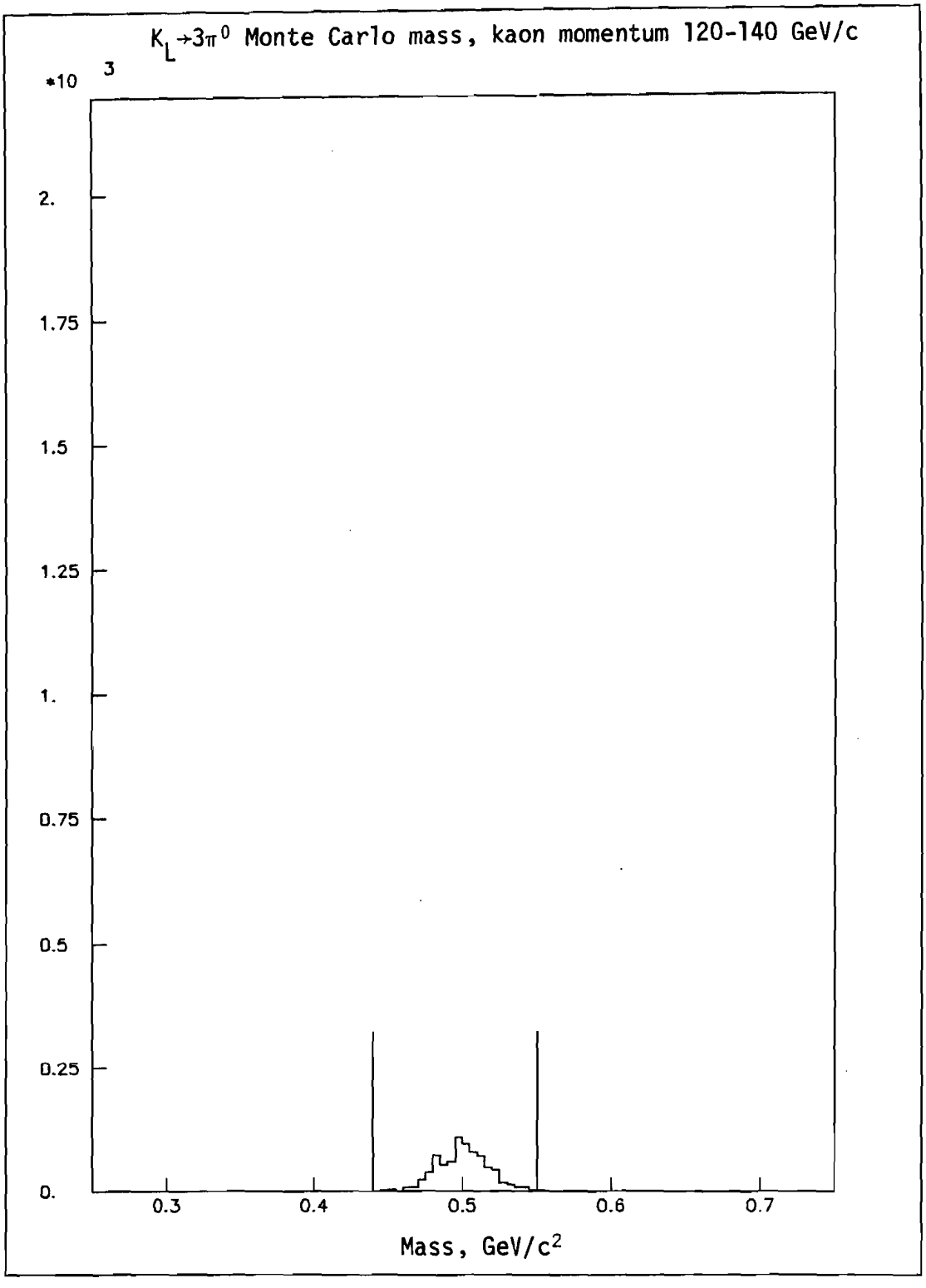
$K_L \to 3\pi^0$ Monte Carlo mass, kaon momentum 120-140 GeV/c
*10 3
2.
1.75
1.5
1.25
1.
0.75
0.5
0.25
0.
0.3
0.4
0.5
0.6
0.7
Mass, GeV/c^2

Appendix-Continued

Object	Radiation Length	Distance from target meters
Magnet Anti (MA)	---	470.09
Helium bag between chamber B and chamber C	0.0013 $\pm 1.9 \times 10^{-5}$	471.32
Analyzing magnet	---	471.32
Air bag between helium bag and chamber C	0.00079 $\pm 3.9 \times 10^{-5}$	472.5
Beam pipe support wires (averaged over plane)	0.00101 $\pm 5 \times 10^{-5}$	472.5
Drift Chamber C	0.00448 $\pm 2.2 \times 10^{-4}$	473.118
Helium bag between chamber C and chamber D	0.00162 $\pm 4 \times 10^{-5}$	475.62
Beam pipe support wires (averaged over plane)	0.000738 $\pm 3.7 \times 10^{-5}$	479.8
Drift Chamber D	0.00492 $\pm 2.5 \times 10^{-4}$	478.105
Air bag between chamber D and G-hodoscope	0.0031 $\pm 1.5 \times 10^{-4}$	478.49
Beam pipe support wires (averaged over plane)	0.00101 $\pm 5 \times 10^{-5}$	478.49
Collar Anti (CA)	---	478.49
G-hodoscope and wrapping	0.009 $\pm 9 \times 10^{-4}$	479.21
Lead glass	---	480.274
Back Anti (BA)	---	513.38
Total Radiation Length	0.21051 $\pm$ 0.00133	

APPENDIX

TABLE OF RADIATION LENGTHS AND POSITIONS OF MATERIAL IN THE BEAM AND SPECTROMETER

Object	Radiation Length	Distance from Target meters
Pinching Anti	---	399.566
Aluminum vacuum window upstream of regenerator	$0.0023011 \pm 1.2 \times 10^{-5}$	401.429
Air from aluminum window to Regenerator Anti (RA)	$0.01540 \pm 7.7 \times 10^{-4}$	404.187
RA scintillator and wrapping	$0.00606 \pm 1.2 \times 10^{-4}$	406.114
Air from RA to vacuum window at start of decay volume	$0.00046 \pm 2.3 \times 10^{-5}$	406.184
Aluminum vacuum window at start of decay volume	$0.0023011 \pm 1.2 \times 10^{-5}$	406.254
Sailcloth window downstream of decay volume	$0.002535 \pm 1.5 \times 10^{-5}$	4.9.44
Air surrounding conversion hodoscope	$0.004273 \pm 2.1 \times 10^{-4}$	420.091
Black polyethylene upstream of hodoscope	$0.000466 \pm 2.3 \times 10^{-6}$	420.0
Aluminized mylar wrapping of A counter	$0.000266 \pm 8 \times 10^{-6}$	420.090
A counter	$0.00695 \pm 6.9 \times 10^{-5}$	420.091
Thin lead converter	$0.09845 \pm 1 \times 10^{-4}$	420.095
Mylar straps holding lead sheet	$0.0001089 \pm 6 \times 10^{-6}$	420.095
V-bank of hodoscope counters	$0.00353 \pm 7.1 \times 10^{-5}$	420.098
H-bank of hodoscope counters	$0.00689 \pm 6.9 \times 10^{-5}$	420.101

taken simultaneously. The normalization to a different particle's decay entailed three systematic errors estimated by the authors at 10% each. Their result was

$$\frac{K_{L\to\gamma\gamma}}{K_L\to all} = (5.0 \pm 1.0) \times 10^{-4}.$$

Enstrom et al. (1971)[11] found 23 $K_L\to\gamma\gamma$ events. The positions and directions of the gamma rays were measured in a converter-spark chamber system. The energy of the gamma rays was not measured, and hence the mass could not be calculated. The kaon energy was measured using time of flight, so $K_L\to\gamma\gamma$ events were selected using collinearity of the gamma rays in a kaon frame. A small observed background was subtracted. All that is said about the $K_L\to 3\pi^\circ$ events used as normalization is the number found. Their result was

$$\frac{K_{L\to\gamma\gamma}}{K_L\to all} = (4.5 \pm 1.0) \times 10^{-4}.$$

Banner et al. (1972)[12] found 4000 $K_L\to\gamma\gamma$ events. The vector momentum of one converted photon was measured, and the position of the other photon was measured. A decay vertex was found by projecting the converted photon back to its intersection with their thin ribbon beam. Events were selected on the basis of collinearity of the gamma rays in

last measurement of the $K_L \to \gamma\gamma$ branching ratio, the accepted value of the CP violation parameter $|\eta_{+-}|^2$ has changed by more than four (old) standard deviations.

While no serious errors may be apparent from the published reports of previous measurements, it is appropriate to point out some of their potential weaknesses.

Arnold et al. (1968)[7] found 16 $K_L \to \gamma\gamma$ decays in a heavy liquid bubble chamber at CERN. Their mass resolution appears to be $\sim$200 MeV/c^2 full width at half maximum, deduced from one of their figures. They normalize their events to the $K_L \to 3\pi^\circ$ decays, for which no mass plot or other evidence of their resolution or background rejection is given. Their result was

$$\frac{K_{L\to\gamma\gamma}}{K_{L\to 3\pi^\circ}} = (2.5 \pm 0.7) \times 10^{-3}.$$

Banner et al. (1969)[8] found 115 $K_L \to \gamma\gamma$ decays at the Princeton-Pennsylvania Accelerator. The vector momentum of one converted gamma ray was measured, and the direction of the other gamma rays in a decay was measured roughly in a spark chamber-converter. The invariant mass of the $K_L \to \gamma\gamma$ events could not be calculated, and they were selected on the basis of collinearity of the two gamma rays and on the energy of the well-measured gamma in the center of mass frame. The main difficulty in this experiment was the extremely low energy of the gamma rays in $K_L \to 3\pi^\circ$ decays,

Figure 71. Plot showing previous published measurements of the branching ratio

$$\frac{K_L \to \gamma\gamma}{K_L \to \text{all}}$$

together with three recent theoretical predictions of this branching ratio, and our new result with statistical and systematic errors added in quadrature.

Figure 70. Plot showing previous published measurements of the ratio

$$\frac{K_L \to \gamma\gamma}{K_L \to 3\pi^0}$$

together with our new result for this quantity, with statistical and systematic errors added in quadrature.

$K_S \to \pi^+\pi^-$ branching ratios to determine the CP violating parameter $|\eta_{00}|^2/|\eta_{+-}|^2$.

$$\frac{|\eta_{00}|^2}{|\eta_{+-}|^2} = \frac{\text{branching ratio } K_L \to 2\pi^\circ}{\text{branching ratio } K_S \to 2\pi^\circ} \times \frac{\text{branching ratio } K_S \to \pi^+\pi^-}{\text{branching ratio } K_L \to \pi^+\pi^-}$$

Using world average values:

$$\text{branching ratio } K_L \to \pi^+\pi^- = (2.03 \pm 0.05) \times 10^{-3}$$

$$\text{branching ratio } K_S \to \pi^0\pi^0 = 0.3139 \pm 0.0024$$

$$\text{branching ratio } K_S \to \pi^+\pi^- = 0.6861 \pm 0.0024$$

and our value,

$$\text{branching ratio } K_L \to \pi^0\pi^0 = (0.974 \pm 0.050) \times 10^{-3}$$

we obtain

$$\frac{|\eta_{00}|^2}{|\eta_{+-}|^2} = 1.049 \pm 0.061.$$

This value is in excellent agreement with the accurate number obtained completely independently from E617 data.[14] The preliminary result from that experiment has about half the error given above, and is greater than unity by just over half a standard deviation.

Such agreement constrains any errors in the measured $K_L \to \gamma\gamma$ branching ratio due to the Monte Carlo or to the normalization method to be within the quoted errors of the measurement.

Figure 69. Plot showing our measurement of the ratio

$$\frac{K_L \to 2\pi^0}{K_L \to 3\pi^0}$$

in four bins of kaon momentum. The fifth point is our ratio for all the data combined, and the sixth point is the current world average.[6] Errors on the first four points are purely statistical, while our combined point shows statistical and systematic errors added in quadrature.

TABLE 2

K_L TO TWO PI ZERO EVENTS,
NORMALIZATION AND ACCEPTANCE

	KAON MOMENTUM, GeV/c			
	50-70	70-90	90-110	110-140
OBSERVED $K_L \to 2\pi^0$ EVENTS	784±28	1183±34	817±29	383±20
TOTAL ACCEPTANCE $K_L \to 2\pi^0$	$(1.454\pm0.009)\times10^{-3}$	$(3.703\pm0.019)\times10^{-3}$	$(3.980\pm0.026)\times10^{-3}$	$(2.54\pm0.025)\times10^{-3}$
OBSERVED $K_L \to 3\pi^0$ EVENTS	16842±130	33533±183	16967±130	4546±67
TOTAL ACCEPTANCE $K_L \to 3\pi^0$	$(1.457\pm0.017)\times10^{-4}$	$(4.57\pm0.04)\times10^{-4}$	$(3.96\pm0.05)\times10^{-4}$	$(1.35\pm0.03)\times10^{-4}$
$\frac{\text{RATE } K_L \to 2\pi^0}{\text{RATE } K_L \to 3\pi^0}$	$(4.66\pm0.18)\times10^{-3}$	$(4.35\pm0.13)\times10^{-3}$	$(4.79\pm0.19)\times10^{-3}$	$(4.48\pm0.27)\times10^{-3}$

for $K_L \to \gamma\gamma$ events. The ratio of these two probabilities, which is sensitive to the total of radiation lengths, is given by

$$3(1 - {}^{7}/_{9}(UP + CN + DN))^4.$$

Inserting the values UP $\sim$ 0.05, CN $\sim$ 0.1, DN $\sim$ 0.05, one obtains a ratio of probabilities of 1.525. If all the radiation lengths are increased by 2%, one obtains a ratio of 1.503, which is 1.4% smaller.

This uncertainty of 1.4%, corresponding to a 2% error in the measurement of the radiation lengths, is being quoted as the systematic error, to take into account unknown errors in the table of radiation lengths per area density. We therefore obtain

$$\frac{\text{Rate } K_L \to \gamma\gamma}{\text{Rate } K_L \to 3\pi^\circ} = (2.836 \pm 0.042 \pm 0.040) \times 10^{-3}$$

a much more accurate result than the current world average[6] for this quantity, which is

$$(2.24 \pm 0.22) \times 10^{-3}.$$

To obtain the branching ratio of $K_L \to \gamma\gamma$, we multiply by the data book[6] value of the branching ratio of $K_L \to 3\pi^\circ$ which is 0.215 $\pm$0.01. The 4.7% error in this quantity adds a systematic error external to the current experiment. Thus,

Figure 68. Plot showing our measurement of the ratio

$$\frac{K_L \to \gamma\gamma}{K_L \to 3\pi^0}$$

in four bins of kaon momentum. The fifth point is our determination of the ratio for all four bins of momentum combined. The errors shown are statistical.

TABLE 1

K_L TO GAMMA GAMMA EVENTS,
NORMALIZATION AND ACCEPTANCE

	KAON MOMENTUM, GeV/c			
	60-80	80-100	100-120	120-140
OBSERVED $K_L \to \gamma\gamma$ EVENTS	3945±75	3052±69	1483±51	512±34
TOTAL ACCEPTANCE $K_L \to \gamma\gamma$	$(1.481\pm0.006)\times10^{-2}$	$(1.890\pm0.009)\times10^{-2}$	$(1.541\pm0.010)\times10^{-2}$	$(8.91\pm0.11)\times10^{-3}$
OBSERVED $K_L \to 3\pi^0$ EVENTS	38300±198	33858±184	11103±105	2055±45
TOTAL ACCEPTANCE $K_L \to 3\pi^0$	$(4.065\pm0.032)\times10^{-4}$	$(5.889\pm0.051)\times10^{-4}$	$(3.39\pm0.05)\times10^{-4}$	$(1.02\pm0.04)\times10^{-4}$
$\frac{\text{RATE } K_L \to \gamma\gamma}{\text{RATE } K_L \to 3\pi^0}$	$(2.827\pm0.061)\times10^{-3}$	$(2.809\pm0.071)\times10^{-3}$	$(2.938\pm0.115)\times10^{-3}$	$(2.85\pm2.23)\times10^{-3}$

Figure 67. Histogram similar to Figure 64, except that the kaon momentum is between 120 and 140 GeV/c.

Figure 66. Histogram similar to Figure 64, except that the kaon momentum is between 100 and 120 GeV/c.

Figure 65. Histogram similar to Figure 64, except that the kaon momentum is between 80 and 100 GeV/c.

Figure 64. Histogram showing the distribution of the reconstructed mass for $K_L \to \gamma\gamma$ Monte Carlo for which the kaon momentum is between 60 and 80 GeV/c. The limits of the accepted mass range are shown as vertical spikes. Events in this plot passed all cuts as used in the final analysis except this one.

vertex and the lead glass. (See Figures 22 and 23.) In both $K_L \to 3\pi^\circ$ and $K_L \to \gamma\gamma$ modes, the mass plot for the lowest kaon momentum shows a low mass tail, which is presumably due to the effect of poorly calibrated blocks on the outside of the lead glass array. The major source of error in the vertex reconstruction was multiple scattering of the electron pair in the thin lead sheet.

As can be seen from Figures 52 through 55, virtually no background existed between the mass cuts at 440 MeV/c^2 and 550 MeV/c^2 (shown on the plots), and none was subtracted. All events between these mass limits were counted as $K_L \to 3\pi^\circ$ signal. The $3\pi^\circ$ Monte Carlo data were analyzed identically, and are shown in Figures 56 through 59.

Mass plots for $K_L \to \gamma\gamma$ are shown in Figures 60 through 63. The mass resolution in this mode is also about 15 MeV/c^2, also primarily due to the vertex resolution, essentially independent of the lead glass energy resolution. A background of 10-20% existed between the mass limits of 440-550 MeV/c^2. This background shape was well simulated by events which passed all cuts except that the distance of closest approach was between 3 and 10 cm. The background was normalized between 250-440 MeV/c^2 and 550-750 MeV/c^2. This background is shown superimposed on the mass

Figure 63. Histogram similar to Figure 60, except that the kaon momentum is between 120 and 140 GeV/c under the assumption that the event is a $K_L \to \gamma\gamma$ decay.

Figure 62. Histogram similar to Figure 60, except that the kaon momentum is between 100 and 120 GeV/c under the assumption that the event is a $K_L \to \gamma\gamma$ decay.

Figure 61. Histogram similar to Figure 60, except that the kaon momentum is between 80 and 100 GeV/c under the assumption that the event is a $K_L \to \gamma\gamma$ decay.